Heat Transfer Enhancement in Phase Change Materials (PCMs) by Metal Foams and Cascaded Thermal Energy Storage

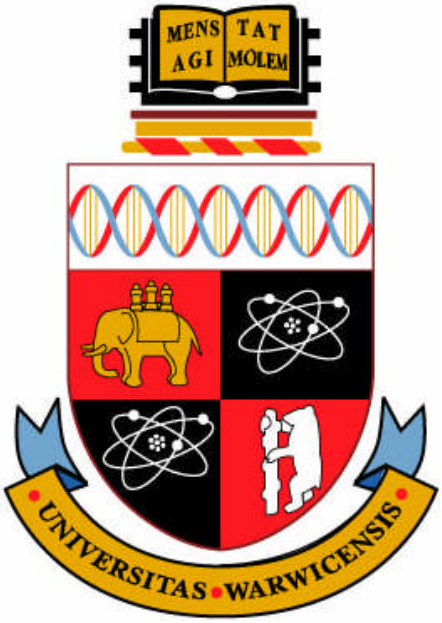

Yuan Tian

Department of Engineering

University of Warwick

Thesis submitted

in partial fulfillment of the requirements for the degree of

Doctor of Philosophy

(November 2012)

Table of Contents

List of Figures

List of Tables

Acknowledgements

Thanks firstly go to my supervisors Prof. Alexei Lapkin and Dr. Changying Zhao. They have provided so much valuable advice in improving the quality of this research, pointing me to the right direction during the whole course of this Ph.D. Changying introduced me into this very interesting research field of metal foams, from which my research skills got significantly developed. Alexei has offered a big help during the preparation of this Thesis. Every comment from him has subsequently improved the quality. I would also like to thank Prof. Robert Critoph and Dr. Zachaire Tamainot-Telto for their important contribution in monitoring the quality of this research during the last three years.

I cannot be more grateful to Prof. Keith Godfrey for his great help in improving my academic writing, which had proved to be extremely important later when I wanted to publish my research results in prestigious journals. If it were not his valuable and professional advice, I would not have been able to publish 14 academic papers during the course of my Ph.D.

Without financial support, this study could not have been finished. I would like to thank the Engineering and Physical Sciences Research Council (EPSRC), the Engineering Department (University of Warwick), the Henry-Lester Trust (UK) and the Great Britain–China Educational Trust (UK) for their generous sponsorship. In addition, the great support that I received from my family is also acknowledged.

Parts of this Thesis have been presented on several international conferences. Acknowledgement goes to EPSRC for their generous sponsorship and also to Dean Boni, Deborah Savage and Sarah Pain for their help in sorting out the flights.

Last but certainly not least, my special thanks go to Roland, Sian, Menai, Pam, Roger, Paul and Graham, for being such good friends and making my spare time so colourful. To Ms. Dan Zhou, my biggest thanks for all your support and love through the ups and downs.

Author Declaration

I hereby declare that this submission is my own work and that, to the best of my knowledge, it contains no material previously published or written by another person nor material which has been accepted for the award of a degree or diploma of the University or any other Institute of Higher Education, except where due acknowledgment has been made in the text.

Signed and dated by the author of this Thesis:
Mr. Yuan Tian
30th November 2012

Supervisors Declaration

This is to certify that the Thesis entitled "Heat Transfer Enhancement in Phase Change Materials (PCMs) by Metal Foams and Cascaded Thermal Energy Storage" submitted by Mr. Yuan Tian to the University of Warwick towards partial fulfillment of the requirements for the award of the degree of *Doctor of Philosophy* in Mechanical Engineering is a bona fide record of the work carried out by him under our supervision and guidance.

Thesis supervisors:
Prof. Alexei Lapkin and Dr. Changying Zhao
30th November 2012

Inclusion of Published Work Arising from the Thesis

- **Peer-reviewed journal papers**

[1] **Tian, Y.**, Zhao, C.Y., 2011a. A numerical investigation of heat transfer in phase change materials (PCMs) embedded in porous metals. *Energy* **36**, 5539–5546.

[2] **Tian, Y.**, Zhao, C.Y., 2011b. Natural convection investigations in porous phase change materials. *Nanosci. Nanotech. Lett.* **3**(6), 769–772.

[3] **Tian, Y.**, Zhao, C.Y., 2012a. A review of solar collectors and thermal energy storage in solar thermal applications. *Appl. Energ.* (In Press: Corrected Proof). doi:10.1016/j.apenergy.2012.11.051.

[4] **Tian, Y.**, Zhao, C.Y., 2012b. A thermal and exergetic analysis of Metal Foam-enhanced Cascaded thermal Energy storage (MF-CTES). *Int. J. Heat Mass Tran.* (In Press: Corrected Proof). doi:10.1016/j.ijheatmasstransfer.2012.11.034.

[5] Zhao, C.Y., Lu, W., **Tian, Y.**, 2010. Heat transfer enhancement for thermal energy storage using metal foams embedded within phase change materials (PCMs). *Sol. Energy* **84**, 1402–1412.

[6] Zhou, D., Zhao, C.Y., **Tian, Y.**, 2012. Review on thermal energy storage with phase change materials (PCMs) in building applications. *Appl. Energ.* **92**, 593–605.

- **Refereed conference papers**

[7] **Tian, Y.**, Zhao, C.Y., 2009a. Heat transfer analysis for Phase Change Materials (PCMs). *11th International Conference on Energy Storage (Effstock 2009)*, Stockholm, Sweden.

[8] **Tian, Y.**, Zhao, C.Y., 2009b. Numerical investigations of heat transfer in phase change materials using non-equilibrium model. *11th UK National Heat Transfer Conference – UKHTC-11*, Queen Mary College, University of London, UK.

[9] **Tian, Y**., Zhao, C.Y., 2010. Thermal analysis in phase change materials (PCMs) embedded with metal foams. In: *Proceedings of 14th International Heat Transfer Conference (ASME Conference) – IHTC-14,* Washington D.C., USA, Volume **7**, 425–434.

[10] **Tian, Y.**, Zhao, C.Y., Lapkin A., 2012. Exergy optimisation for cascaded thermal storage. In: *Proceedings of the 12th International Conference on Energy Storage (Innostock 2012)*. University of Lleida, Lleida, Spain.

- **Book chapter**

[11] **Tian, Y.**, 2012. Phase change convective heat transfer in high porosity cellular metal foams. In Book: *Focus on Porous Media Research*. Nova Science Publishers Inc., New York (ISBN: 978-1-62618-668-2).

Breakdown:

Parts of [3] and [6] arise from Chapter 2 of this Thesis;

[7], [8] and parts of [5] arise from Chapter 3 of this Thesis;

[1], [2] and [9] arise from Chapter 4 of this Thesis;

[10] arises from Chapter 5 of this Thesis;

[4] arises from Chapter 6 of this Thesis;

[11] arises from parts of Chapters 3, 4, 5 and 6 of this Thesis.

Other Publications

The author also has the following publications produced during the course of this Ph.D., but these publications did not arise from the current Thesis:

[12] Du, Y.P., Zhao, C.Y., **Tian, Y.**, Qu, Z.G., 2012. Analytical considerations of flow boiling heat transfer in metal-foam filled tubes. *Heat Mass Transfer* **48**(1), 165–173.

[13] Han, X.X., **Tian, Y.**, Zhao, C.Y., 2012. A phase field model for heat transfer in a metal foam-embedded Latent Thermal Energy Storage (LTES) system. In: *Proceedings of 8th International Symposium on Heat Transfer – ISHT-8*, Tsinghua University, Beijing, China.

[14] Han, X.X., **Tian, Y.**, Zhao C.Y., 2013. An effectiveness study of enhanced heat transfer in Phase Change Materials (PCMs). *Int. J. Heat Mass Tran.* **60**, 459–468. doi:10.1016/j.ijheatmasstransfer.2013.01.013.

Flow boiling heat transfer in metal foams was investigated in [12], and Phase Field Model for solving phase change phenomena was developed in [13] and [14]. They are not included in this Thesis because of their low relevance.

Abstract

Low heat transfer performance has been the main problem restricting the use of Phase Change Materials (PCMs) in situations requiring rapid energy release or storage. Three innovative solutions are studied in this Thesis to improve heat transfer in PCMs. These include combining PCMs with metal foams, Cascaded Thermal Energy Storage (CTES) and Metal Foam-enhanced Cascaded Thermal Energy Storage (MF-CTES). Heat conduction is investigated in Chapter 3, in which it was found that metal foams can improve heat conduction of PCMs by 5–20 times. Natural convection is investigated in Chapter 4, in which metal foams were found to suppress natural convection due to their large flow resistances. Nevertheless, metal foams can still achieve a higher overall heat transfer rate (3–10 times) than PCMs without metal foams. CTES is examined in Chapter 5, with results showing that CTES has a higher heat transfer rate (30%) and a higher exergy transfer rate (22%) than Single-stage Thermal Energy Storage (STES). MF-CTES is proposed in Chapter 6; this is, to the best knowledge of the author, the first time that it has been investigated. MF-CTES was found to further improve the heat and exergy transfer of CTES by 2–7 times, meanwhile reducing melting time by 67%–87%.

Nomenclature

a_{sf}	=	specific surface area	m^{-1}
A	=	area	m^2
Bi	=	Biot number	(dimensionless)
c_p	=	specific heat capacity at constant pressure	kJ/(kg ^oC)
$c_{p.HTF}$	=	specific heat capacity of Heat Transfer Fluid (HTF)	kJ/(kg ^oC)
$c_{p.MF}$	=	specific heat capacity of metal foam	kJ/(kg ^oC)
$c_{p.PCM}$	=	specific heat capacity of Phase Change Material (PCM)	kJ/(kg ^oC)
C_f	=	inertia coefficient of fluid flow in metal foams	(dimensionless)
d	=	characteristic length	m
d_f	=	equivalent diameter of metal fibres	m
d_p	=	equivalent pore diameter	m
dA	=	differential heat transfer area	m^2
dq	=	differential heat	W
dV	=	differential volume	m^3
e	=	length ratio of cubic juncture node to ligament	(dimensionless)
g	=	gravity constant (non-variable)	m/s^2
h	=	the distance step	m
h_{ex}	=	effective exergy transfer rate	W/m^2
h_{exch}	=	heat exchange rate between HFT and PCM	W/m^2
h_{HTF}	=	effective heat transfer coefficient of HTF	W/m^2
h_{sf}	=	interstitial heat transfer coefficient	$W/(m^2 K)$
$h_{1, 2, 3}$	=	heat transfer coefficients (in Chapters 3 and 4)	$W/(m^2 K)$
$h_{1, 2}$	=	system dimensions in *y*-axis (in Chapters 5 and 6)	m
H_L	=	latent heat	kJ/kg
H_{PCM}	=	PCM enthalpy function	kJ/kg

i, j	=	index numbers of the nodes in the computational domain	(dimensionless)
k	=	thermal conductivity	W/(m K)
k_f	=	thermal conductivity of the fluid saturated in the metal foam	W/(m K)
k_s	=	thermal conductivity of the metal used to make the metal foam	W/(m K)
$\bar{k}_{MF}$	=	effective thermal conductivity of the metal foam when PCM is taken off	W/(m K)
$\bar{k}_{PCM}$	=	effective thermal conductivity of the porous PCM when metal foam is taken off	W/(m K)
$\bar{k}_{PCM-MF}$	=	effective thermal conductivity of the PCM-embedded metal foam	W/(m K)
K	=	permeability	m^2
$L_{1, 2, 3}$	=	system dimension in x-axis	m
m	=	mass	kg
m, n	=	node numbers (in Chapter 3)	(dimensionless)
Nu	=	Nusselt number	(dimensionless)
p	=	pressure	Pa
Pr	=	Prandtl number	(dimensionless)
q	=	heat transfer rate	W/m^2
q_w	=	heat flux	W/m^2
r	=	mesh ratio	(dimensionless)
r_p	=	effective pore radius	m
$R_{A, B, C, D}$	=	thermal resistance	$(m^2 K)/W$
Re	=	Reynolds number	(dimensionless)
R_g	=	ideal gas constant	kJ/(kg K)
s	=	specific entropy	kJ/kg

S	=	position function for the melting front	m
t	=	time	s
T	=	temperature	^{o}C
T_a	=	ambient temperature (non-variable)	^{o}C
T_m	=	melting temperature	^{o}C
T_w	=	wall temperature	^{o}C
T_{HTF}	=	temperature function of HTF	^{o}C
T_{MF}	=	temperature function of metal foam	^{o}C
T_{PCM}	=	temperature function of PCM	^{o}C
$T_{0.HTF}$	=	HTF inlet temperature (non-variable)	^{o}C
u	=	the component of flow velocities in x-direction	m/s
U	=	equivalent thermal conductivity of the PCM-embedded metal foam samples	W/(m K)
v	=	the component of flow velocities in y-direction	m/s
V	=	volume	m^3
$\mathbf{V}$	=	velocity vector	m/s
x	=	the horizontal coordinate in the x-axis	m
X	=	specific anergy	kJ/kg
y	=	the vertical coordinate in the y-axis	m

Greek symbols

α	=	thermal diffusivity	m^2/s
β	=	linear thermal expansion coefficient	K^{-1}
ΔT	=	temperature difference	^{o}C
ε	=	porosity	(percentage)
η_{ex}	=	exergy efficiency	(percentage)

λ	=	ratio of ligament radius to ligament length	(dimensionless)
λ_{HTF}	=	thermal conductivity of HTF	W/(m K)
μ_f	=	dynamic viscosity	Pa·s
π	=	circumference ratio	(dimensionless)
ρ	=	density	kg/m^3
τ	=	time step	s
υ	=	kinetic viscosity	m^2/s

Subscripts

e	=	effective value
ex	=	exergy
exch	=	heat exchange
f	=	fluid; HTF; fibre (in metal foam)
p	=	pore
s	=	metal
sf	=	inter-phase value (between PCM and metal foam)
HTF	=	heat transfer fluid
L	=	latent heat
MF	=	metal foam
PCM	=	Phase Change Materials
PCM-MF	=	PCM and metal foam
ref	=	reference value
w	=	wall
0	=	initial or ambient
1, 2	=	initial, final state of a thermal system (Chapters 5 and 6)
a	=	ambient

∞	=	ambience

Superscripts

$\dot{}$	=	mass rate
$\bar{}$	=	mean value of a variable

Mathematical operators

∇	=	Laplace operator
$\bullet$	=	dot product of two vectors
$\langle\ \rangle$	=	volume-averaged value
$\lvert\ \rvert$	=	the absolute value of a variable
$\lVert\ \rVert$	=	the norm of a vector

Abbreviations

AC	=	Alternating Current
CENG	=	Compressed Expanded Natural Graphite
CTES	=	Cascaded Thermal Energy Storage
DC	=	Direct Current
EG	=	Expanded Graphite
ES	=	Energy Storage
EES	=	Electric Energy Storage
ε–NTU	=	Effectiveness–Number of Transfer Units
FDM	=	Finite Difference Method

FVM	=	Finite Volume Method
HES	=	Hydraulic Energy Storage
HTF	=	Heat Transfer Fluid
MF	=	Metal Foam
MF-CTES	=	Metal Foam-enhanced Cascaded Thermal Energy Storage
PCM	=	Phase Change Materials
PLS	=	Power Law Scheme
RAM	=	Random Access Memory
REV	=	Representative Elementary Volume
SIMPLE	=	Semi-Implicit Method for Pressure Linked Equations
SIMPLER	=	Semi-Implicit Method for Pressure Linked Equations Revised
STES	=	Single-stage Thermal Energy Storage
TES	=	Thermal Energy Storage

Chapter 1. Introduction

1.1. Energy Storage (ES)

Efficient utilisation of solar energy is increasingly being considered as a promising solution to anthropogenic climate change, and as a means of achieving the state of sustainable development for human society. Solar energy is a form of intermittent energy, which highly depends on the weather, location and time. This has therefore made Energy Storage (ES) an essential technology in almost all solar, and other renewable technologies applications. In solar applications, ES plays two roles: firstly to ensure an unceasing energy supply at times of low solar radiation; secondly to act as an efficient energy buffer in the process of electric peak shaving. The three main options for the efficient storage of solar energy are Electric Energy Storage (EES), Hydraulic Energy Storage (HES) and Thermal Energy Storage (TES).

1.1.1. Electric Energy Storage (EES)

In EES, energy is usually stored in large-capacity batteries or superconducting materials. Dincer and Rosen (2010) reviewed various types of batteries for EES, but concluded that despite battery technologies having been greatly developed since the late 19th century, present-day batteries are still not suitable for large-scale energy applications because of their weight, cost, and short life cycles. Current batteries are struggling to reach a life cycle of 1,000 times, but a life cycle of 10,000 times is usually needed for EES applications to achieve a reasonably low long-term cost and excellent reversibility.

Electric energy can also be efficiently stored in a magnetic field induced by superconductors, with corresponding research under development as noted in Dincer and Rosen (2010). The working principle is that superconductors completely lose their electric resistance when temperature drops down to a critical value and thus large electric

currents can circulate in them without any losses. The critical temperature is around 0 K (–273 ºC) for most materials, with the highest one discovered being 55 K (–218 ºC) for specially designed iron-based superconducting materials (Paglione and Greene, 2010). To ensure a suitable working temperature for superconductors, a large amount of electricity is needed for the cryogenic machines. In addition, superconductors store direct current (DC) instead of alternating current (AC), so energy losses also occur in the conversion processes between DC and AC. To date, technologies for suitable batteries and superconductors in EES are very limited, and the relevant research is still in its early stage.

1.1.2. Hydraulic Energy Storage (HES)

In Hydraulic Energy Storage (HES) water is pumped up to a certain height and the stored potential energy can be later converted into kinetic energy when flowing through a hydraulic turbine. HES has the following advantages: simple equipment required, long operation period (more than 20 years) and quick response when the energy is needed. However, drawbacks such as low energy efficiency and low energy storage density still exist. 30% of the energy is lost when water is pumped uphill and 20% of the energy is lost when water flows down (Dincer and Rosen, 2010). The energy stored when 1 kg water is lifted up to a height of 4,285.7 meters is equal to the energy stored in the same amount of water when heated up by 10 ºC, suggesting that HES really has a very low energy storage density.

1.1.3. Thermal Energy Storage (TES)

In Thermal Energy Storage (TES), energy is stored by heating/cooling, or melting/solidifying, or gasifying/liquefying special materials, or through thermo-chemical processes. TES is a very promising option for solar applications, due to its low cost and high storage capacity. Heat storage capacity of TES is generally 10^3 times higher than

that of HES and 1–2 times higher than that of EES (Dincer and Rosen, 2010; Tian and Zhao, 2012a). In addition, TES technologies are much more developed than EES technologies. All these have made TES attractive in energy storage applications. TES will be the research topic of this Thesis.

Playing a pivotal role in balancing energy demand and energy supply, TES relies on high-quality Phase Change Materials (PCMs): high heat storage capacity and high heat transfer performance. Most PCMs can store or release a large amount of heat during phase change, providing a very high heat storage capacity (90 kJ/kg to 330 kJ/kg) (Zalba et al., 2003; Sharma et al., 2009). However, the inherent low thermal conductivities of PCMs usually result in poor heat transfer, restricting their application in situations which require rapid energy release and storage. Thus, heat transfer enhancement is essential for TES (Tian, 2012).

1.2. Objectives

As discussed in Section 1.1.3, poor heat transfer is a key problem when applying PCMs to a TES system. The research objective of this Thesis is to enhance heat transfer for PCMs by means of Metal Foams (MF) and Cascaded Thermal Energy Storage (CTES).

1.2.1. Metal foams

Low thermal conductivity is the main reason accounting for poor heat transfer in PCMs. It can be solved by incorporating high-thermal conductivity enhancers. Open-cell metal foams have high thermal conductivities and continuous inter-connected structures, which are very useful in achieving a more uniform temperature distribution and higher heat transfer performance inside PCMs. In this Thesis, the effects of metal foams on PCMs will be investigated both theoretically and experimentally.

1.2.2. Cascaded Thermal Energy Storage (CTES)

A decrease in the driving force (temperature difference) is the second reason accounting for heat transfer deterioration. For a single-stage PCM storage system, temperature of the heat transfer fluid falls rapidly when transferring heat to the PCM; as a result, the temperature difference between them is reduced, leading to poor heat transfer at the end of the storage. Such problems can be solved by employing Cascaded Thermal Energy Storage (CTES). A typical CTES system consists of multiple PCMs (with cascaded melting temperatures) arranged along the flow direction, which can help to keep a relatively constant temperature difference. How and by how much CTES improves the thermal performance of a TES system will be investigated in this Thesis.

In addition, a combination of metal foams and CTES, which is Metal Foam-enhanced Cascaded Thermal Energy Storage (MF-CTES), will also be investigated.

1.3. Thesis outline and methodology

The current technologies of heat transfer enhancement in PCMs are reviewed in Chapter 2. These include using high-thermal conductivity metal enhancers, carbon materials, metal foams, and CTES technology. As for enhancer materials, the review has found that metal foams have a high potential to achieve better heat transfer than metal fins and carbon materials. Therefore metal foams are investigated in Chapter 3 and Chapter 4.

Heat conduction of PCM-embedded metal foams is addressed in Chapter 3. The enthalpy method is employed to consider phase change, with the movement of the melting front tracked by numerical simulations. The effects of metal foam porosity and pore size are also examined. Two models are proposed, and both of them have achieved good agreement with experimental data.

Natural convection of PCM-embedded metal foams is addressed in Chapter 4. A two-equation non-thermal equilibrium model is employed to distinguish the temperature difference between metal foam and PCM. The flow and temperature profiles during phase change are obtained by numerical simulations, which are validated by experimental data. The dual effects of metal foams on PCMs are also examined.

CTES is a newly proposed technology. Most currently available publications have focused on energy analysis, with only a few addressing exergy analysis. Therefore Chapter 5 consists of an overall exergy and energy analysis of CTES, in which a three-stage PCM CTES system is examined. Heat transfer rate, exergy efficiency and effective exergy transfer rate are obtained from numerical simulations. Comparison is made between CTES and the traditional Single-stage Thermal Energy Storage (STES).

The idea of combined metal foam and CTES is investigated Chapter 6: Metal Foam-enhanced Cascaded Thermal Energy Storage (MF-CTES). To the best knowledge of the author, this is the first time that MF-CTES has been investigated. In Chapter 6, a three-stage PCM MF-CTES system is examined. Heat transfer rate, exergy efficiency and effective exergy transfer rate are obtained. Comparison is also made between MF-CTES, CTES and STES.

The conclusions drawn from Chapters 3, 4, 5 and 6 are summarised in Chapter 7. Suggestions for possible further work are also proposed.

Chapter 2. Literature Review

2.1. Thermal Energy Storage (TES)

Carbon dioxide-induced global warming and depletion of fossil fuels are the two most pressing issues in the energy research field. Efficient utilisation of renewable energy sources, especially solar energy, is increasingly being considered as a promising solution to them and a means of achieving a sustainable development for human beings.

Solar energy has low-density and is intermittent. Therefore Thermal Energy Storage (TES) plays a pivotal role in balancing energy demand and energy supply. TES can be classified into three main categories according to different storage mechanisms: sensible heat storage, latent heat storage and chemical heat storage.

2.1.1. Sensible heat storage

In sensible heat storage, thermal energy is stored by the storage media when their temperatures are rising. The specific heat capacity for most sensible heat storage media ranges from 0.5 kJ/kg to 4.2 kJ/kg (Sharma et al., 2009; Tian and Zhao, 2012a). The common advantage of sensible heat storage is its low cost and simple operating conditions (Pilkington Solar International GmbH, 2000). However, the disadvantage is its large temperature variance after heat is stored/released, which has highly restricted its application to most situations requiring strict working temperatures.

2.1.2. Latent heat storage

In latent heat storage, Phase Change Materials (PCMs) are used. PCMs can store/release large amounts of heat during melting/solidification or gasification/liquefaction processes. The phase-transition enthalpy of most PCMs ranges from 90 kJ/kg to 330 kJ/kg (Zalba et al., 2003; Sharma et al., 2009), thus latent heat storage has much higher storage capacity

than sensible heat storage. Unlike sensible heat storage in which materials have a large temperature rise/drop during working, latent heat storage can work in a nearly isothermal way due to the phase change mechanism of PCMs. This makes latent heat storage favourable for those applications which require strict working temperatures. Despite all these advantages of latent heat storage, the drawback still exists: most PCMs have rather low thermal conductivities, yet to be significantly improved by heat transfer enhancement technologies (Velraj et al., 1999; Jegadheeswaran and Pohekar, 2009; Fan and Khodadadi, 2011). More details are given in Section 2.3.

2.1.3. Chemical heat storage

Chemical heat storage was proposed to store solar energy, because certain chemicals can absorb/release large amounts of thermal energy when they break/form chemical bonds during endothermic/exothermic reactions (Wentworth and Chen, 1976; Prengle and Sun, 1976). Suitable materials for chemical heat storage can be organic or inorganic, as long as their reversible chemical reactions involve absorbing/releasing large amounts of heat. Chemical heat storage usually has an enthalpy change in the order of MJ/kg, much higher than that of latent heat storage (in the order of kJ/kg), reviewed by Tian and Zhao (2012a). However, the research of chemical heat storage is still in its very early stage, and its application is limited due to the following problems: complicated reactor design needed for specific chemical reactions (Zondag et al., 2008; Turton et al., 2008; Couper et al., 2010), corrosion and toxicity (Ervin, 1977), wide working temperature ranges (Kato et al., 2001 and 2009), strict requirements of pressure vessels (Lovegrove et al., 2004), weak long-term durability (reversibility) (Hauer, 2007), and weak chemical stability (Foster, 2002; Gil et al., 2010).

2.1.4. Summary

Sensible heat storage has the lowest heat storage capacity, but at a very low cost; latent heat storage has a much higher heat storage capacity, still at a reasonable cost; chemical heat storage, despite having the highest storage capacity, is at its very early research stage, with many problems restricting its application: complicated reactor design (followed by high cost) and weak reversibility and stability. All studies in this Thesis focus on latent heat storage.

2.2. Phase Change Materials (PCMs)

Thermal Energy Storage (TES) technologies rely on high-quality Phase Change Materials (PCMs), which should have high heat storage capacity and excellent heat transfer performance. PCMs include the solid-solid type (low phase change enthalpy) in which the phase transition occurs within the solid state, the solid-liquid type (high phase change enthalpy) in which the phase changes from solid to liquid, and the liquid-gas type (very high phase change enthalpy) in which the phase changes from liquid to gas. The large volume change in the liquid-gas PCMs restricts their application in TES. The relatively low phase change enthalpy of the solid-solid PCMs also restricts their application in TES. Relatively high phase change enthalpy and small volume change make the solid-liquid PCMs the ideal option for TES. Figure 2.1 includes a broad range of known solid-liquid PCMs, giving their melting temperature (ºC) and enthalpy (kJ/L) ranges.

PCMs can be made of organics (paraffins and fatty acids), inorganic minerals (salts, salt hydrates/hydroxides) or eutectics. Different types of PCMs are listed in Table 2.1. Organic PCMs have the advantages of good chemical compatibility and no super-cooling, whilst the disadvantages are their low thermal conductivities (mostly 0.2 W/(m K)), flammability and non-constant phase change temperatures. Inorganic PCMs have slightly higher thermal conductivities (mostly 0.5 W/(m K)), but they have very severe super-

cooling problems, resulting in reduction of storage capacity and unstable working temperatures (Shukla et al., 2008; Kuznik et al., 2011). Storage capacity reduces significantly when the PCM temperature falls just below the melting point, because latent heat cannot be released due to the delayed solidification by super-cooling. Eutectic PCMs have sharp phase change temperatures, but they have the problem of large volume changes (Zhou et al., 2012).

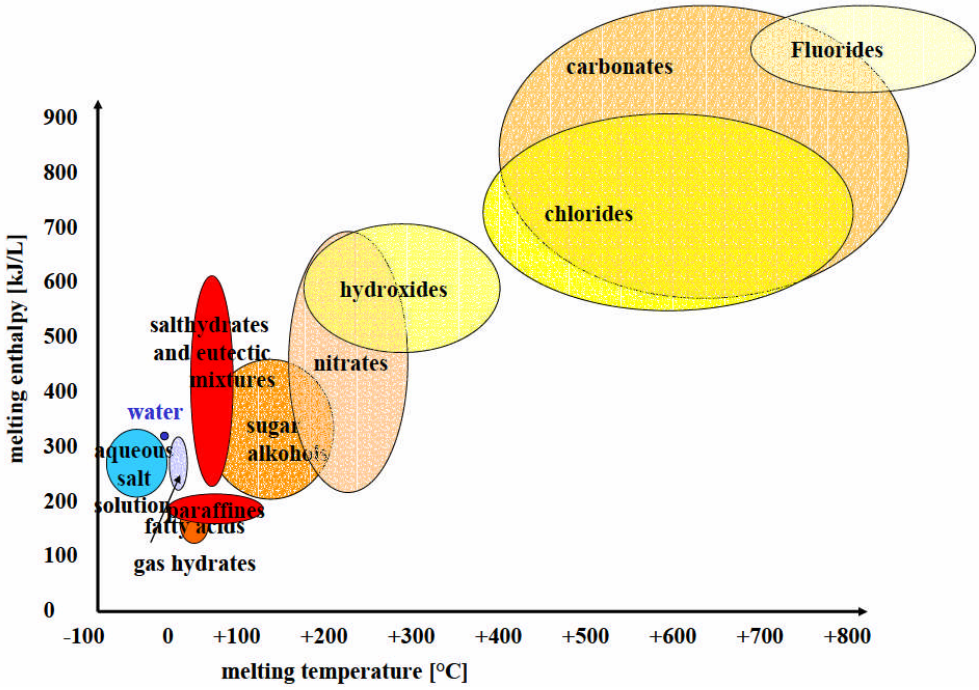

Figure 2.1. Different types of Phase Change Materials (PCMs) (Mehling and Hiebler, 2004).

Table 2.1. Organic, inorganic and eutectic PCMs.

PCMs	Type	Melting Temperature (^{o}C)	Heat of fusion (kJ/kg)	Specific Heat (kJ/(kg K))	Thermal Conductivity (W/(m K))
Polyglycol E600	organic	22	127.2	n.a.	0.190
Paraffin C16–C18	organic	20-22	152	n.a.	n.a.
Paraffin C13–C24	organic	22-24	189	2.1	0.210
RT27	organic	26–28	179	1.8–2.4	0.200
Paraffin C18	organic	28	244	2.16	0.150
1-Tetradecanol	organic	38	205	1.8–2.4	0.358
RT50	organic	50	168	2.1	0.200
Paraffin wax	organic	64	174–266	2.1	0.167–0.346
Paraffin C21–C50	organic	66–68	189	2.1	0.210
Naphthalene	organic	80	147.7	1.7	0.132–0.341
RT100	organic	100	n.a.	n.a.	0.200
$CaCl_2 \cdot 6H_2O$	inorganic	29	190.8	n.a.	0.540 –0.561
$Na_2SO_4 \cdot 10H_2O$	inorganic	32.4	254	n.a.	0.544
$Zn(NO_3)_2 \cdot 6H_2O$	inorganic	36	146.9	n.a.	0.464–0.469
$Mg(NO_3)_2 \cdot 6H_2O$	inorganic	89	162.8	n.a.	0.490–0.669
KNO_3	inorganic	333	266	n.a.	0.500
66.6%$CaCl_2 \cdot 6H_2O$ +33.3% $MgCl_2 \cdot 6H_2O$	eutectic	25	127	n.a.	n.a.
61.5%$Mg(NO_3)_2 \cdot 6H_2O$ +38.5% NH_4NO_3	eutectic	52	125.5	n.a.	0.494–0.552
66.6% urea +33.4% NH_4Br	eutectic	76	161.0	n.a.	0.324–0.682

PCMs have received extensive research interest during the last decade, and they were investigated in a variety of applications: energy saving buildings (Neeper, 2000; Pasupathy et al., 2008), solar collectors (Mettawee and Assassa, 2006), solar still (El-Sebaii et al., 2009), solar cooker (Domanski et al., 1995; Sharma et al., 2005), high-efficient compact heat sinks (Nayak et al., 2006; Shatikian et al., 2008), industrial waste heat recovery (Buddhi, 1997) and solar power plants (Michels and Pitz-Paal, 2007). Thermal stability investigations of PCMs were also conducted through implementing repeated thermal cycle tests (Tyagi and Buddhi, 2008; El-Sebaii et al., 2011).

2.3. Heat transfer enhancement of PCMs

Most PCMs have large heat storage capacity, ranging from 90 kJ/kg to 330 kJ/kg (Zalba et al., 2003), but they suffer from the common problem of low thermal conductivities, being around 0.2 W/(m K) for most paraffin waxes and 0.5 W/(m K) for most inorganic salts (Zalba et al., 2003). Low heat transfer performance has been the main factor restricting the application of PCMs in situations requiring rapid energy release/storage (Mills et al., 2006; Zhao et al., 2010). Researchers have proposed various methods enhancing heat transfer in PCMs, and these include: incorporating high thermal conductivity enhancers into PCMs (Stritih, 2004; Mettawee and Assassa, 2007); adopting porous heat transfer media (Py et al., 2001; Sari and Karaipekli, 2007; Lafdi et al., 2008; Nakaso et al., 2008; Zhou and Zhao, 2011); Cascaded Thermal Energy Storage (CTES) (Watanabe and Kanzawa, 1995; Tian et al., 2012).

2.3.1 High-thermal conductivity metal enhancers

Most metal materials have high thermal conductivities, ranging from 40 W/(m K) to 400 W/(m K) (Holman, 1997). Therefore, metal pieces, fins, powders and beads can be used as high thermal conductivity enhancers to improve heat transfer in PCMs. Mazman et al. (2008) tested copper pieces as additives into PCMs, and found that heat transfer was

increased by up to 70%. Zhang and Faghri (1996a and 1996b) numerically investigated the heat transfer enhancement in PCMs by using finned tubes. They found that the enhancement was below 30%, whether using internally or externally finned tubes. Stritih (2004) added 32 metal fins into PCM to enhance heat transfer, and found the heat transfer was increased by 67% with melting time reduced by 40%. However, Stritih (2004) concluded that the addition of metal fins did not have the desired effects on heat transfer enhancement, with the reason being that natural convection was completely suppressed by the metal fins (large flow resistance).

Mettawee and Assassa (2007) placed aluminium powders in the PCM for a compact PCM solar collector and tested its performance during the processes of charging and discharging. They found a notable reduction of melting time (60%), meaning the heat transfer was increased by 150%.

Moreover, not all researchers have achieved good heat transfer enhancement by using high-thermal conductivity metal enhancers. Ellinger and Beckermann (1991) experimentally investigated the heat transfer enhancement in a rectangular domain partially occupied by a porous layer of aluminum beads. They found that the introduction of a porous layer caused the solid/liquid interface to move faster initially during the conduction-dominated regime. But in the later convection-dominated regime, the overall melting and heat transfer rates were found to be lower with the presence of porous layer due to the low porosity and permeability. They concluded that the porous layer severely constrained the convective heat transfer.

In summary, the enhancement effects by using these metal enhancers (metal pieces, fins, powders and beads) look to be limited to between 67% and 150%, which is not high enough to meet most application requirements.

2.3.2. Porous materials

Porous media with high thermal conductivities can also be used to enhance heat transfer for PCMs. These include carbon materials and metal foams.

2.3.2.1. Carbon materials

Carbon materials usually have high thermal conductivities. For example, synthetic graphite has a thermal conductivity from 25 W/(m K) to 470 W/(m K) depending on the manufacturing process; laboratory-made carbon nanotubes were even reported to have a surprisingly high value of 6,600 W/(m K) (Berber et al., 2000). Having such high thermal conductivities, carbon materials have been examined for heat transfer enhancement in PCMs.

Nakaso et al. (2008) tested the use of carbon fibres to enhance heat transfer in thermal storage tanks, reporting a twofold rise in effective thermal conductivities. Their carbon cloths and carbon brushes (both made of high-thermal conductivity carbon fibres) are shown in Figure 2.2. They also found that the carbon cloths had better thermal performance than carbon brushes because the cloth structure was more continuous than the brush structure.

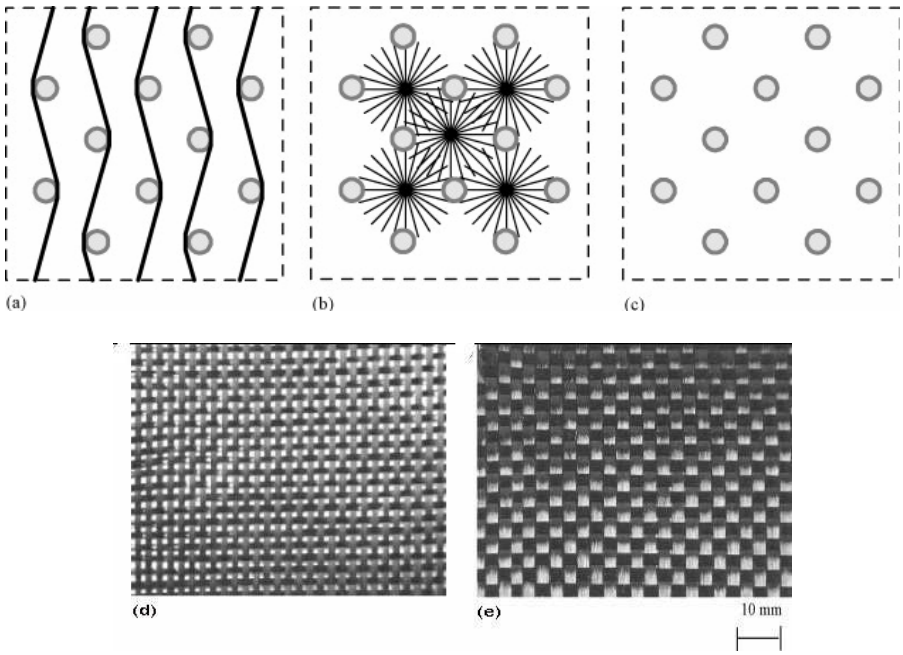

Figure 2.2. Use of carbon fibres to enhance heat transfer (Nakaso et al., 2008).
(a) Fibre cloth; (b) Fibre brush; (c) No carbon fibre;
(d) Fibre cloth of 142g/m^2; (e) Fibre cloth of 304g/m^2.

The thermal conductivity of the carbon-PCM systems can usually be increased by raising the volume percentage of carbon materials used. However, the volume percentage of the carbon fibres in Nakaso et al. (2008) could only reach around 1% due to the low packing density. A higher percentage can be achieved by compressing carbon materials. Paraffin/CENG composites can have a carbon percentage as high as 5% (CENG means compressed expanded natural graphite), and are usually made by impregnating paraffin (with the aid of capillary forces) into a porous graphite matrix to form a stable composite material. Such composites were elaborated and characterised by Py et al. (2001); they have good thermal conductivities, but present a strong anisotropy in the axial and radial directions due to mechanical compression, which makes the heat transfer performance vary in different directions.

To avoid anisotropy, Paraffin/EG (Expanded Graphite) composites were introduced, and they can be made to incorporate even more carbon. Sari and Karaipekli (2007) fabricated a series of the Paraffin/EG composites, shown in Figure 2.3. They found that the effective thermal conductivity was increased by between 81.2% and 272.7% depending on the mass fraction of EG added. However, the main disadvantage of EG is its structural discontinuity, resulting in large thermal contact resistance and inefficient heat transfer.

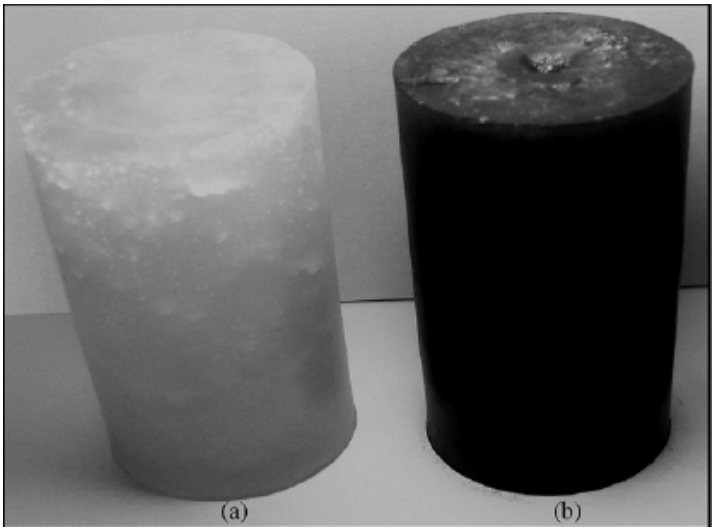

Figure 2.3. Photograph of (a) pure paraffin as PCM; (b) paraffin/EG (10% mass) composite as form-stable PCM (Sari and Karaipekli, 2007).

2.3.2.2. Metal foams

To overcome the structural discontinuity of the Paraffin/EG composites, metal foams (shown in Figure 2.4) have been investigated, because they have continuous inter-connected structures with porosity ranging from 85% to 97%, as well as high thermal conductivities. Extensive investigations have been carried out for heat transfer in metal foams. However, most of them worked on the non-phase change heat transfer. These include single-phase heat conduction (Calmidi and Mahajan, 1999; Boomsma and Poulikakos, 2001; Zhao et al., 2004b), single-phase forced convection (Lee et al., 1993;

Calmidi and Mahajan, 2000; Kim et al., 2000; Kim et al., 2001; Hwang et al., 2002; Bhattacharya et al., 2002; Zhao et al., 2004a; Zhao et al., 2006; Lu et al., 2006), single-phase natural convection (Phanikumar and Mahajan, 2002; Zhao et al., 2005), and single-phase thermal radiation (Zhao et al., 2004c).

Phase change heat transfer in metal foams has been reported in a few literatures. Tian and Zhao (2009a and 2011a) conducted an experiment in which metal foams were embedded to PCMs, and their results showed a considerable increase of heat transfer rate (overall, 3–10 times). Dukhan (2010) made an experiment tesing the effect of metal foams on energy storage/release duration, and he found significant reduction of energy charging/discharging time (up to 42.4%) due to high thermal conductivity of metal foams.

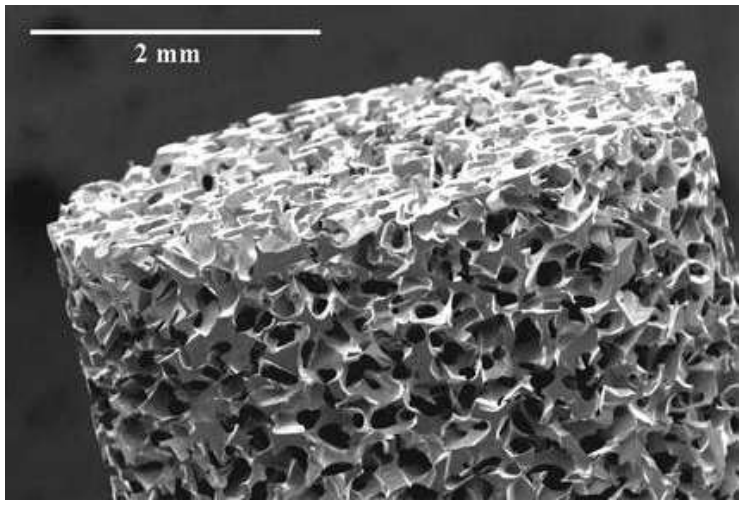

(a) A piece of metal foam
(http://www.acceleratingfuture.com/michael/blog/category/images/page/4/);

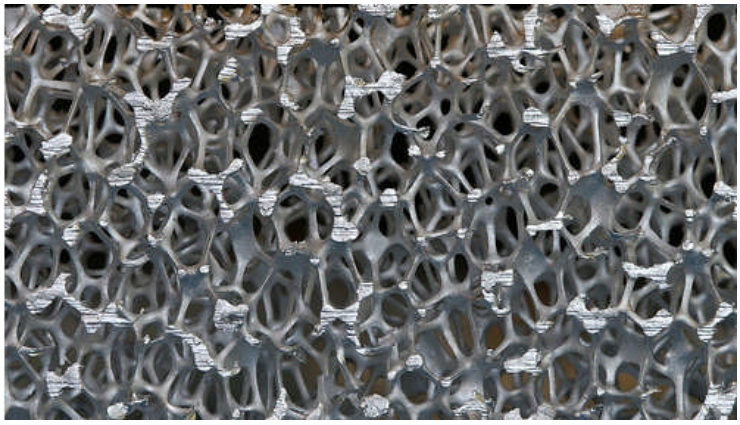

(b) Close-up
(Tian and Zhao, 2011).

Figure 2.4. Metal foam.

Zhou and Zhao (2011) experimentally investigated the Paraffin/EG and Paraffin/Metal Foam composites. They found that both Paraffin/EG and Paraffin/Metal Foam increased heat transfer rate significantly, but Paraffin/Metal Foam showed better performance than

Paraffin/EG, shown in Figure 2.5. It should be noted that in their study, heat flux was fixed, thus smaller temperature differences represented better heat transfer.

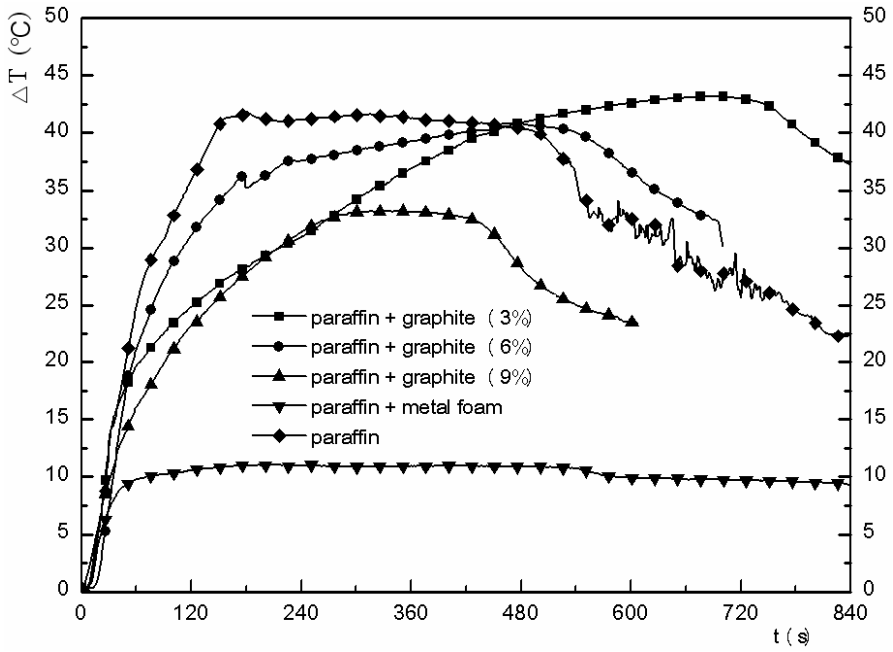

Figure 2.5. Temperature differences (ΔT) between Paraffin/EG and Paraffin/Metal Foam (Zhou and Zhao, 2011).

The reason why metal foams performed better than EG was later numerically investigated by Tian and Zhao (2011a): the structures inside EG are rather sparse (discontinuous), whilst metal foams have much more continuous inter-connected structures, which means heat can be efficiently transferred to the PCM. They also investigated the effects of metal foam parameters (porosity and pore density) on heat transfer, and found that better heat transfer was achieved by metal foams with low porosity and high pore density. The effects of the PCM viscosity and thermal expansion coefficient were also examined, with

results showing that low viscosity and high thermal expansion coefficient delivered better heat transfer.

2.4. Numerical investigations of heat transfer in metal foams

2.4.1. Heat conduction

Due to the geometric complexity of metal foam microstructures, almost all previous researchers have used regular polygons or polyhedrons to approximate the real metal foam structures. These include hexagons used by Calmidi and Mahajan (2000), cubes used by Dul'nev (1965), dodecahedrons used by Ozmat et al. (2004), and tetrakaidecahedrons used by Boomsma and Poulikakos (2001). The models based on hexagons, cubes, dodecahedrons and tetrakaidecahedron are shown in Figure 2.6(a), 2.6(b), 2.6(c) and 2.6(d), respectively, with Figure 2.6(e) showing the real metal foam structures. In their models, metal foam was assumed to have periodical structures with each cell approximated by the aforementioned polygons or polyhedrons.

Effective thermal conductivity is an important parameter to model heat conduction in porous media, different mathematical formulae of which have been derived by researchers depending on the geometry used. The hexagon model by Calmidi and Mahajan (2000) was under two-dimensional approximation, therefore lacking of high accuracy. The cube model by Dul'nev (1965) was three-dimensional and easy to use, but the simple geometry lacked resemblance to the real metal foam structures. The dodecahedron structures proposed by Ozmat et al. (2004) beared better resemblance to the real metal foam structures, but they reported a low model accuracy for high thermal conductivity ratios (between the saturation material and the metal). The tetrakaidecahedron model proposed by Boomsma and Poulikakos (2001) does not appear to suffer such problems, and therefore is still the most commonly used model to obtain the effective thermal conductivity of metal foams.

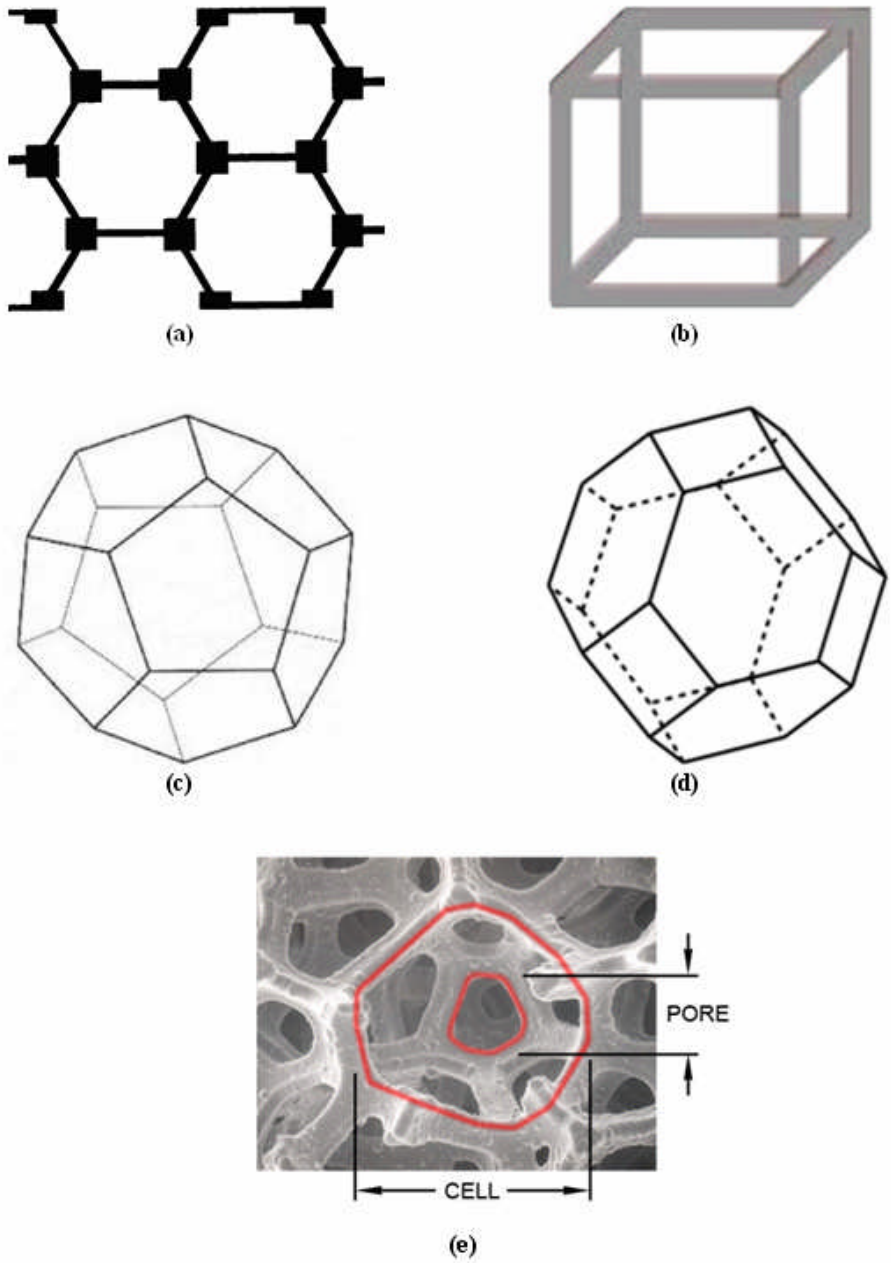

Figure 2.6. Geometry approximation of metal foam.

(a) Hexagon; (b) Cube;

(c) Dodecahedron; (d) Tetrakaidehedron;

(e) Real metal foam structure.

2.4.2. Forced and natural convection

Darcy Law (Darcy, 1856) has been widely used to model fluid flow in porous media, which states that the volume-averaged flow velocity through porous media is proportional to the pressure gradient and the permeability of the porous media whilst inversely proportional to the dynamic viscosity of the fluid. Darcy Law is valid for seepage flow in which both porosity and flow velocity are low; however, Darcy Law no longer holds true for flow in metal foams because flow velocity in metal foams is usually high due to high porosity. In addition, Darcy Law neglects inertial forces and fails to satisfy the non-slip boundary condition which holds true for almost all viscous fluids. Brinkman (1947) and Forchheimer (1901) modified Darcy Law by adding two correction terms to account for inertial and viscous effects. Based on Brinkman-extended Darcy Law, Lu et al. (2006) presented an analytical solution to flow in metal foams, but inertial forces were neglected in their study. Tian et al. (2008) numerically investigated both viscous and inertial effects in metal foam-filled pipes, and found that inertial effects (Forchheimer, 1901) were dominant over viscous effects (Brinkman, 1947) especially under high flow velocity. Their research extended the famous SIMPLE algorithm (Semi-Implicit Method for Pressure Linked Equations) (Patankar, 1980) for forced flow in metal foams, making a numerical simulation possible. However, their work did not consider natural convection, nor phase change heat transfer. Despite that natural convection was numerically simulated in air-filled metal foam by Zhao et al. (2005), there is still a pressing need to investigate the coupled conduction/convection phase change heat transfer in high-porosity metal foams.

2.4.3. Phase change heat transfer

Traditional heat transfer models in porous media have been based on the thermal equilibrium condition, which assumes a sufficient heat communication between porous media and saturation material so that only one heat transfer equation is needed to consider two components. This holds true for most porous media such as packed beds and granular materials which have low porosity (volume percentage of each component does not vary much) and low thermal conductivity ratio. For metal foams, their high porosity means thermal equilibrium is difficult to achieve; metal materials usually have a thermal conductivity 10^3 times higher than saturation materials such as air and water. All these have made the traditional one-equation thermal equilibrium model unsuitable for metal foams.

Krishnan et al. (2005) numerically investigated the solid/liquid phase change phenomena in metal foams by using a two-temperature numerical model. However, their numerical results were not validated by a phase change experiment in real metal foams, due to the lack of experimental data at that time. Zhao and Tian (2010) carried out an experiment on heat transfer in PCM-embedded metal foams, a two-dimensional heat conduction model was also presented, which agreed well with experimental data. This study did not consider the effect of natural convection, and was later improved by Tian and Zhao (2011a), in which the effects of metal foam inner structures on heat transfer were analysed. Their investigation was based on the two-equation non-equilibrium heat transfer model, and the coupled problem of heat conduction and natural convection was solved for phase change heat transfer in metal foams. Their results showed that heat can be quickly transferred to the whole domain of PCMs with the help of the metal foam frame. However, at the two-phase zone and liquid zone, metal foams were found to have large flow resistance, thus suppressing the natural convection in PCMs. Nonetheless, the

PCM–metal foam samples still achieved higher overall heat transfer performance than the PCM sample, which implies that the enhancement of heat conduction offsets or exceeds the natural convection loss.

Phase change heat transfer in PCM-embedded metal foams was also numerically investigated in other methods such as Phase Field Model (PFM) and Lattice Boltzmann Method (LBM). According to Han et al. (2013), PFM that uses a set of phase field parameters to distinguish melting zone from the solid/liquid zone has advantages in tracking moving boundaries which would otherwise have to be tackled by the enthalpy method. Their study did not consider fluid flow, which is important to convective heat transfer. Zhao et al. (2010) numerically investigated convective heat transfer by using LBM, in which the complicated thermal transport in metal foams was modelled by choosing appropriate spatio-temporal distribution functions. However, the geometric structures assumed in their simulations were discontinuous squares, which beared no resemblance to real metal foam structures (coutinuous).

2.5. Cascaded Thermal Energy Storage (CTES)

2.5.1. Motivation

The main advantage of latent heat storage over sensible heat storage is the high storage capacity within a small temperature band. Figure 2.7(a) (Mehling and Cabeza, 2008) gives a comparison between a sensible heat storage system and a latent heat storage system made of a single PCM. For the small temperature difference covering the phase change zone, there is a factor of 3 between the heat stored in the latent heat storage system and the sensible heat storage system. For a larger temperature difference, the advantage of the latent heat storage shrinks to 6:4 = 1.5, so that there is no reason to prefer a latent heat storage system to a sensible heat storage system.

Mehling and Cabeza (2008) suggested that the use of a cascaded arrangement of multiple PCMs with different melting temperatures should solve the above problem. Figure 2.7(b) (Mehling and Cabeza, 2008) shows a typical three-stage Cascaded Thermal Energy Storage (CTES) system: the PCM I with the lowest melting temperature is heated from T_1 to T_2, the PCM II with the medium melting temperature is heated from T_2 to T_3, and the PCM III with the highest melting temperature is heated from T_3 to the maximum temperature. Using such a cascaded storage system, the difference of the stored energy between cascaded latent heat storage and single sensible heat storage is 10:4 = 2.5.

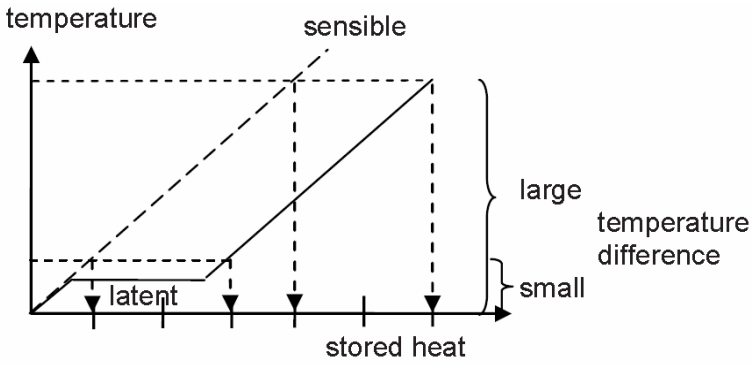

(a) With a single PCM

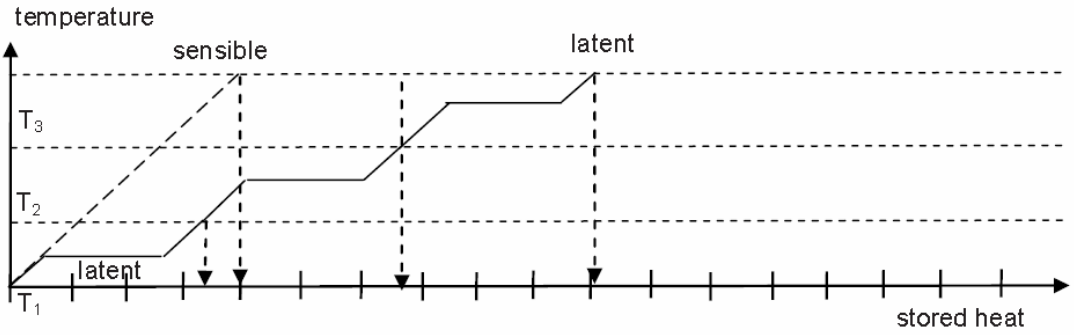

(b) With cascaded latent heat storage

Figure 2.7. Comparison of stored heat between sensible heat storage and latent heat storage (Mehling and Cabeza, 2008).

Another reason for using CTES is illustrated as follows. A very common practical situation is that the charging and discharging time is usually limited and the heat needs to be stored or released quickly. When charging a storage system with only a single-stage PCM, the heat transfer fluid rapidly transfers heat to the PCM. The temperature of the heat transfer fluid therefore reduces, which in turn reduces the temperature difference between the PCM and heat transfer fluid and leads to poor heat transfer at the end of the

storage. As a result, the PCM is melted rapidly at the entrance part where the Heat Transfer Fluid (HTF) enters the storage, but the PCM is melted more slowly at the end of the storage where HTF exits the storage. For the discharging process, the problem still exists: the PCM at the end of the storage might not be used for latent heat storage as the HTF temperature rises. By using CTES, such problems can be solved. Figure 2.8 gives a comparison between a single-stage PCM system and a five-stage CTES PCM system (Medrano et al., 2010; Pilkington Solar International GmbH, 2000). For charging process, a PCM with a lower melting temperature can be placed at the end of the heat exchanger, so that the temperature difference can be large enough to ensure all PCMs to be melted. CTES also works efficiently for discharging process.

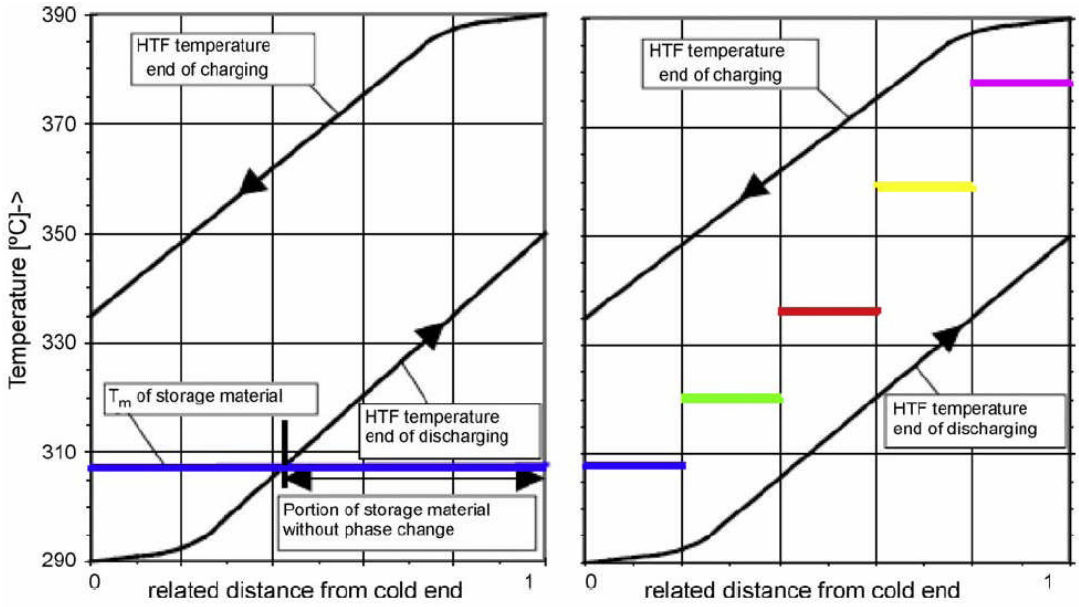

Figure 2.8. Comparison between a single-stage storage system and a five-stage cascaded storage system (Medrano et al., 2010; Pilkington Solar International GmbH, 2000).

2.5.2. Applications

Cascaded Thermal Energy Storage (CTES), consisting of multiple PCMs with cascaded melting temperatures, has recently been proposed as a solution to heat transfer deterioration, which often arises when charging/discharging a single-stage PCM storage system. The reasons were given in Section 2.3.2.1.

Gong and Mujumdar (1997) investigated a five-stage PCM system, and found a significantly improved heat transfer (34.7%) compared to the single PCM system. Michels and Pitz-Paal (2007) investigated a three-stage PCM system, and found that a higher proportion of melted PCM and a more uniform heat transfer fluid outlet temperature than in the traditional single-stage storage.

The study by Michels and Pitz-Paal (2007) was based on energy efficiency, not having considered exergy efficiency that represents the utilisable part of energy. Exergy analyses for multiple PCM systems were conducted by Watanabe and Kanzawa (1995), and Shabgard et al. (2012). Watanabe and Kanzawa (1995) found an increased exergy efficiency by using multiple PCMs, whilst Shabgard et al. (2012) found that the multiple PCMs recovered a larger amount of exergy despite having lower exergy efficiency at times. Tian et al. (2012) conducted an overall thermal analysis of a three-stage CTES system, and found that CTES achieved a higher heat transfer rate than the Single-stage Thermal Energy Storage (STES), but CTES did not always achieve higher exergy efficiency than STES.

2.5.3. Metal Foam-enhanced Cascaded Thermal Energy Storage (MF-CTES)

An overall thermal analysis taking exergy into account considers not only the quantity of the energy, but also the quality of the energy, and therefore is very important. However, there are only a few publications addressing exergy issues for CTES. Moreover, none of

these existing studies has combined CTES with other heat transfer enhancement techniques, especially the use of metal foams. Chapter 6 of this Thesis aims to investigate, for the first time, the idea of the metal foam-enhanced CTES system, examining its technical feasibility and evaluating its energy and exergy performance.

Chapter 3. Heat Conduction

To investigate the thermal transport phenomena in PCM-embedded metal foams, two main heat transfer modes need to be considered: heat conduction and natural convection. Heat conduction is addressed in Chapter 3, whilst natural convection is addressed in Chapter 4. This Chapter starts with a basic one-dimensional heat conduction problem, then progresses to the real two-dimensional heat conduction problem.

3.1. One-dimensional heat conduction

3.1.1. Problem description

Figure 3.1(a) illustrates the one-dimensional heat conduction for the PCM-embedded metal foam. The PCM, after being heated into liquid, flows and fills the entire pore space inside the metal foam, and thus a PCM-embedded metal foam system is formed. The system is heated by a constant heat flux q_w on the bottom boundary, and is thermally insulated on the top boundary. The melting front denotes the border line dividing the liquid and the solid zone, and it moves upwards as time increases. Figure 3.1(b) shows a differentiation control volume inside the PCM-embedded metal foam system. For the control volume considered (the grey in Figure 3.1(b)), the net heat flux is equal to the heat flux coming from the top control volume (q^+) minus the heat flux going to the bottom control volume (q^-). Discussion on the governing equations in Section 3.1.2 will be based on Figure 3.1(b).

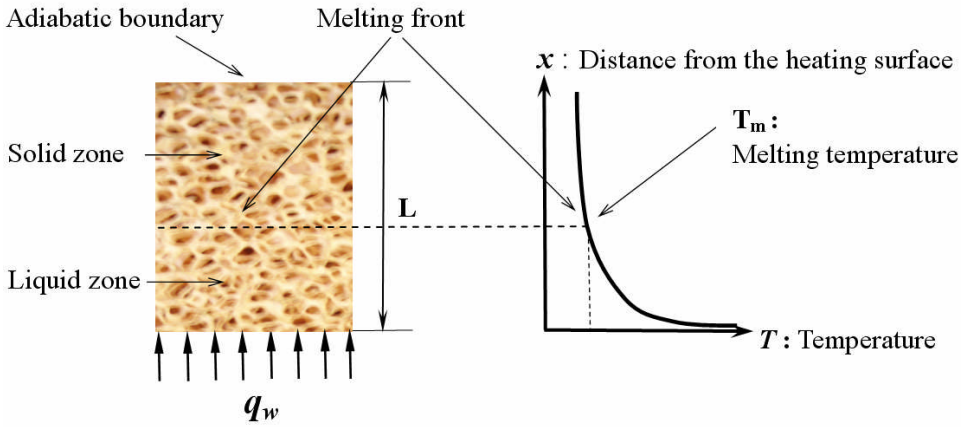

(a)

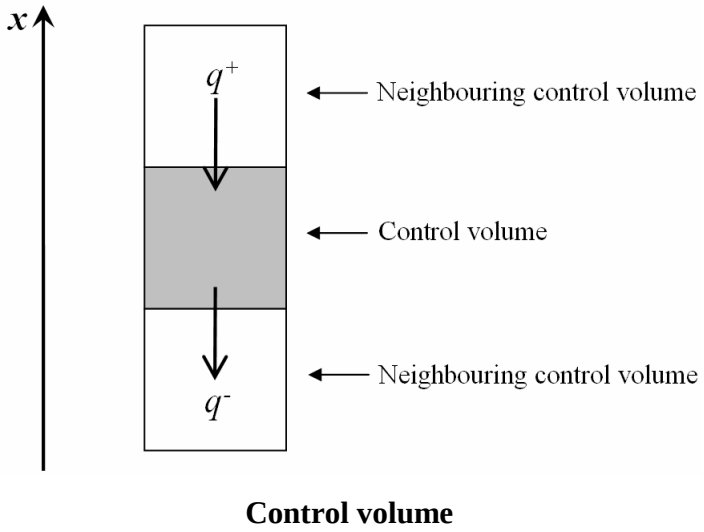

(b)

Figure 3.1. One-dimensional heat conduction for the PCM-embedded metal foam.

3.1.2. Governing equation

Within Cartesian coordinate system, the governing equation for one-dimensional heat conduction takes on the following form:

$$\frac{\partial T(x,t)}{\partial t} = \alpha \frac{\partial^2 T(x,t)}{\partial x^2} \tag{3.1}$$

where $T(x,t)$ is the PCM temperature, t is time, x is the horizontal coordinate, α is the PCM thermal diffusivity and is given by:

$$\alpha = \frac{\bar{k}_{PCM-MF}}{\rho c_p} \tag{3.2}$$

where ρ and c_p denote the PCM density and specific heat capacity respectively; $\bar{k}_{PCM-MF}$ is the effective thermal conductivity of the PCM-embedded metal foam.

When calculating $\bar{k}_{PCM-MF}$, the following factors need to be considered: porosity, pore size, pore shape, and the thermal conductivities of both the metal material and the PCM. Details of the derivation of $\bar{k}_{PCM-MF}$ are given later in Section 3.1.3.

The boundary conditions of Eq. (3.1) are given by:

$$-\bar{k}_{PCM-MF} \frac{\partial T(0,t)}{\partial x} = q_w \tag{3.3a}$$

$$\frac{\partial T(L,t)}{\partial x} = 0 \tag{3.3b}$$

$$T(S(t),t) = T_m \tag{3.3c}$$

$S(t)$ is the position function of the melting front. It varies with time t, having a value from 0 to L. The correlation between $S(t)$ and $T(x,t)$ can be obtained by the energy conservation law, shown below:

$$\rho H_L \frac{d(S(t))}{dt} = \bar{k}_{PCM-MF} \frac{\partial T(S(t)^+, t)}{\partial x} - \bar{k}_{PCM-MF} \frac{\partial T(S(t)^-, t)}{\partial x} \tag{3.4}$$

where H_L (kJ/kg) is the latent heat of the PCM, *T(x, t)* is a piecewise function that has different definitions in the solid and the liquid phases. The superscript "+" denotes the solid phase, whilst the superscript "–" denotes the liquid phase. The term on the left hand side of Eq. (3.4) represents the net amount of heat that a control volume at the melting front absorbs. As shown in Figure 3.1(b), the net heat equals q^+ minus q^-. In fact, the first term on the right hand side of Eq. (3.4) is q^+, and the second term on the right hand side of Eq. (3.4) is q^-.

The initial condition of Eq. (3.1) is given by:

$$T(x,0) = T_0 \tag{3.5}$$

3.1.3. Determination of the effective thermal conductivity ($\bar{k}_{PCM-MF}$)

Determination of the effective thermal conductivity $\bar{k}_{PCM-MF}$ is complicated, because it depends on porosity, pore size, pore shape, and thermal conductivities of both the metal material and the PCM. $\bar{k}_{PCM-MF}$ is usually modelled by researching geometrically similar structures.

Calmidi and Mahajan (2000) presented a two-dimensional simplified model of the effective thermal conductivity for metal foams, which gave good agreement with test data. However the real microstructures in metal foams are three-dimensional, and therefore a three-dimensional model is preferred in order to improve model accuracy. In this Chapter, a three-dimensional structured model presented by Boomsma and Poulikakos (2001) has been used to deal with the effective thermal conductivity of metal foams. A tetrakaidecahedron (Thomson, 1887) was used in their model to approximate metal foam

cells, because it is the polyhedron with the minimal surface energy. The reason for using the principle of minimal surface energy is that metal foam cells tend to shrink to the minimal surface when being manufactured by foaming processes. Figure 3.2 shows the structure of a tetrakaidecahedron, which is a fourteen-face polyhedron comprising six squares and eight hexagons. By using such a polyhedron approximation, Boomsma and Poulikakos (2001) obtained a good agreement between model predictions and experimental data on metal foams with porosities from 88% to 98%. Their model is shown in Eq. (3.6):

$$\bar{k}_{PCM-MF} = \frac{\sqrt{2}}{2\left(R_A + R_B + R_C + R_D\right)} \tag{3.6a}$$

$$R_A = \frac{4\lambda}{\left(2e^2 + \pi\lambda(1-e)\right)k_s + \left(4 - 2e^2 - \pi\lambda(1-e)\right)k_f} \tag{3.6b}$$

$$R_B = \frac{\left(e-2\lambda\right)^2}{\left(e-2\lambda\right)e^2 k_s + \left(2e - 4\lambda - (e-2\lambda)e^2\right)k_f} \tag{3.6c}$$

$$R_C = \frac{\left(\sqrt{2}-2e\right)^2}{2\pi\lambda^2\left(1-2e\sqrt{2}\right)k_s + 2\left(\sqrt{2}-2e-\pi\lambda^2\left(1-2e\sqrt{2}\right)\right)k_f} \tag{3.6d}$$

$$R_D = \frac{2e}{e^2 k_s + \left(4-e^2\right)k_f} \tag{3.6e}$$

$$\lambda = \sqrt{\frac{\sqrt{2}\left(2-(5/8)e^3\sqrt{2}-2\varepsilon\right)}{\pi\left(3-4e\sqrt{2}-e\right)}} \tag{3.6f}$$

$$e = 0.339 \tag{3.6g}$$

In Eqs. (3.6a) to (3.6g), e is a length ratio defined by Boomsma and Poulikakos (2001) to account for the effect of the juncture nodes where metal fibres joint, ε is the metal foam porosity, k_s is the thermal conductivity of the metal material used to manufacture the

metal foam, k_f is the thermal conductivity of the material saturated in the metal foam, and R_A, R_B, R_C and R_D are the calculated thermal resistance of four different layers inside a tetrakaidecahedron cell. The effective thermal conductivity $\bar{k}_{PCM-MF}$ is a result of these four layers thermally placed in parallel (Boomsma and Poulikakos, 2001).

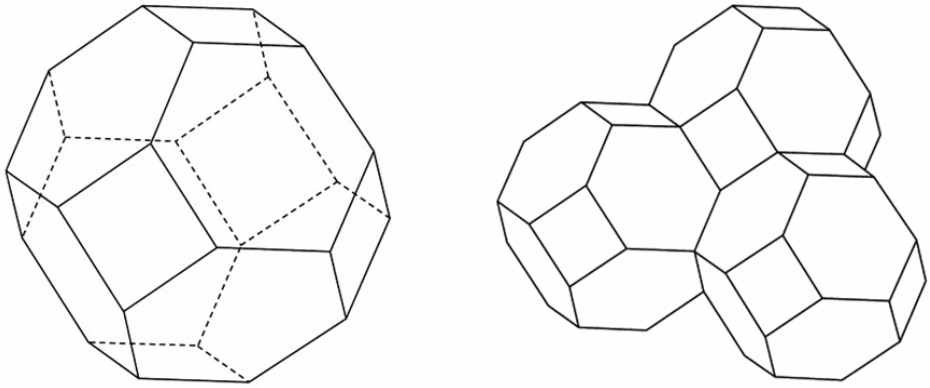

(a) A single tetrakaidecahedron; (b) Three tetrakaidecahedrons lapped together

Figure 3.2. Tetrakaidecahedron (Fourie and Du Plessis, 2002).

3.1.4. Discretisation schemes

- **Explicit scheme**

The governing equation is a parabolic-type partial differential equation, as shown in Eq. (3.1). It can be discretised into the following forms:

$$T_{i,j+1} = rT_{i-1,j} + (1-2r)T_{i,j} + rT_{i+1,j} \tag{3.7a}$$

$$r = \frac{\alpha\tau}{h^2} \quad (i = 2,3,\cdots,\mathrm{m}-1;\ j = 1,2,\cdots,\mathrm{n}-1) \tag{3.7b}$$

where $T_{i,j}$ denotes the temperature at the *i*-th node at the *j*-th time step, τ and h are the time step and the distance step respectively. The discretised nodes are shown in Figure 3.3.

By using the explicit scheme, the temperature at a certain time step can be obtained from the calculated temperature at the previous time step. Thus, with Eq. (3.5) giving the initial temperature in the whole computational domain, the temperature at any node and any time step can be calculated. The drawback of the explicit scheme is its divergence when time step is larger than a critical value (mesh ratio r is greater than 0.5), the mathematical proof of which is given by Morton and Mayers (2005). To ensure numerical convergence, a small time step is usually used in the explicit scheme, which significantly increases the computing time.

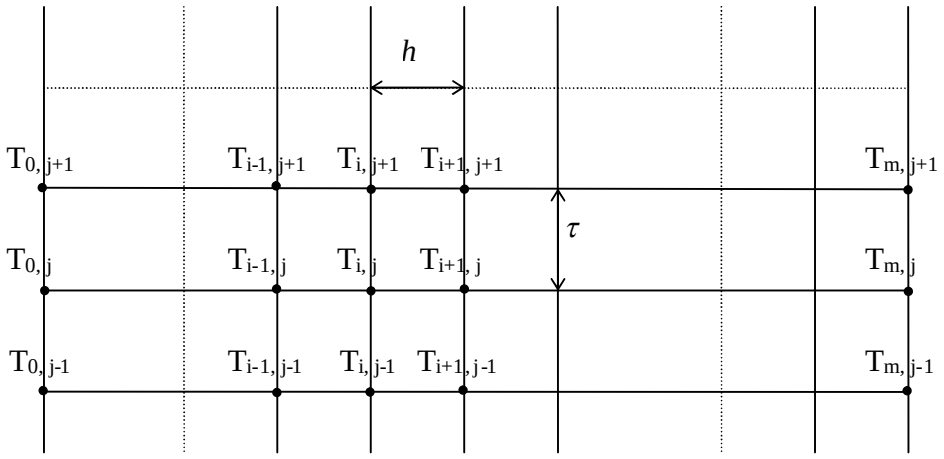

Figure 3.3. Discretised nodes.

- **Implicit scheme**

The implicit scheme is given by:

$$-rT_{i-1,\,j+1} + (1+2r)T_{i,\,j+1} - rT_{i+1,\,j+1} = T_{i,\,j} \tag{3.8}$$

The temperature at a certain time step cannot be directly obtained from the calculated values at the previous time step. Instead, a series of algebraic equations have to be solved.

According to the study conducted by Tian and Zhao (2009a), the implicit and the explicit scheme produced the same calculation results, and the difference is that the former showed much better numerical convergence in large time steps than the latter.

3.1.5. Numerical procedure and validation

To get better numerical convergence and reduce computing time, the implicit scheme was adopted in the simulation, which was executed under the workspace of Matlab®. The discretised equation – Eq. (3.8) was solved in a 112×6000 mesh, including 112 nodes in the *x*-axis and 6000 nodes in the time axis. Numerical simulations were set to stop when the difference between two consecutive iterations was less than 10^{-6} (0.0001%).

Mesh independence was also conducted by examining a finer mesh. The number of the nodes in the *x*-axis was doubled to 224, thus the number of the nodes in the time axis should be quadrupled to ensure a constant mesh ratio *r*, shown in Eq. (3.7b). Numerical simulations indicated that a 224×24000 mesh could only improve the accuracy by 0.03% compared to the 112×6000 mesh, meaning a finer mesh is not needed. The numerical accuracy was determined by comparing the two mesh systems. 0.03% represents the relative temperature difference (temperatures measured in ºC) between the two mesh systems averaged on each calculation grid.

To validate the simulations, the program was used to solve the one-dimensional transient heat conduction problem (no phase change) under two different boundary conditions: constant heat flux and constant temperature. The maximum discrepancy between the simulation results and the corresponding analytical solutions was found to be less than 0.15%.

3.1.6. Results and discussion

- **Comparison with experimental data**

The simulation results were compared to the experimental data by Tian and Zhao (2009a). RT58 (manufacturer: Rubitherm® Technologies GmbH, Germany) was used as the PCM, and a piece of copper foam of 95% porosity and 10 ppi was used to enhance heat conduction. Here 95% porosity means the pore volume percentage is 95%; 10 ppi means the pore density is 10 pores per inch (1 inch = 0.0254 m). Pore density represents the pore size in metal foams, with higher pore density meaning smaller pore size. The PCM RT58 has a latent heat of 181 kJ/kg and a specific heat of 2.1 kJ/kg. More thermal properties of RT58 are given in Section 4.4.1. Figure 3.4 shows the comparison of PCM temperatures between the simulation and the experiment. Good agreement between the two is achieved in the early heating stage and the late phase change stage. However, large discrepancies exist in the early phase change stage, because the RT58, which should have a nominal melting temperature of 58 ºC, actually melts in a large temperature range (48 ºC – 62 ºC) according to Rubitherm®. Thus, the numerical results in Figure 3.4 indicate that the melting starts only when the temperature rises up to 58 ºC, whilst the experimental data indicate that the melting actually starts earlier. Large discrepancies also exist in the post-melting stage (natural convection-dominated area), because natural convection was not considered in the present model. Two other reasons accounting for such large discrepancies are: low accuracy of the model (only one-dimensional) and inability to consider the temperature difference between the PCM and the metal foam. Low accuracy of the present model will be improved by a two-dimensional analysis in Section 3.2, which will employ a two-temperature model to consider the temperature difference between the PCM and the metal foam.

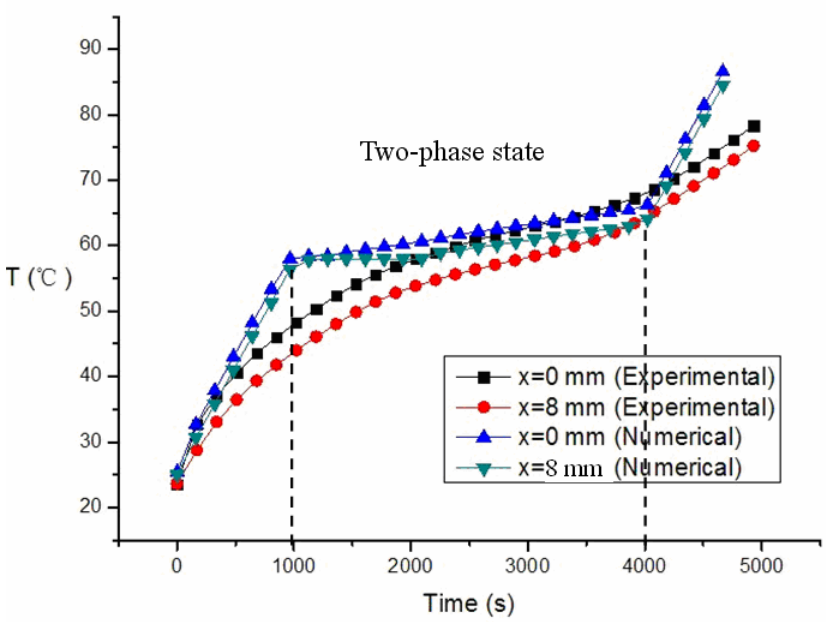

Figure 3.4. Comparison between numerical results and experimental data (one-dimensional heat conduction).

- **Melting front**

Figure 3.5 shows the model-predicted PCM temperature variance as a function of time. When t = 805 s, melting has not started (below melting point: 58 ºC). When t = 1529 s and 2616 s, melting has started, with the melting front moving gradually from the heat surface inwards. As time increases, the PCM has finished melting and fully become liquid state when t = 4225 s.

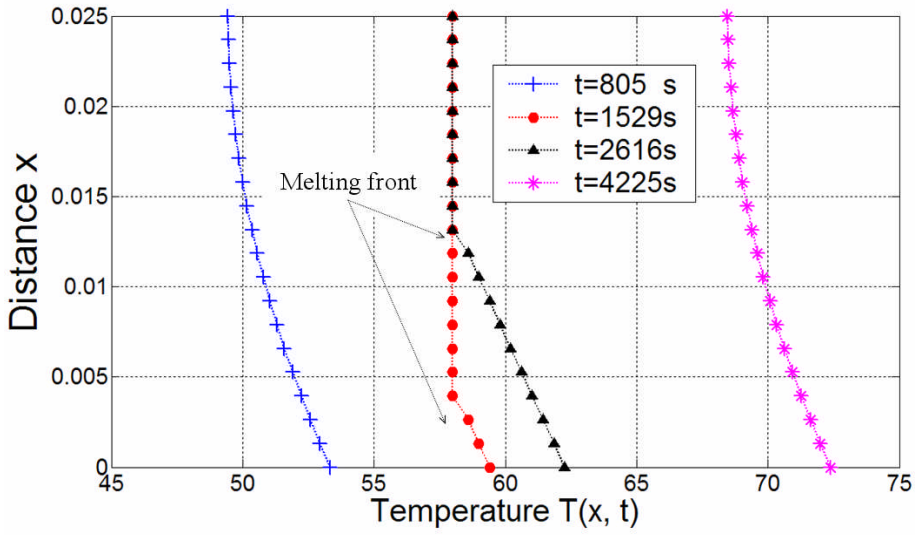

Figure 3.5. Melting front.

- **Effect of different metal foam samples**

Figure 3.6 gives the model-predicted temperature difference between the heating surface and x = 8 mm, for two metal foam samples (95% and 85% porosity respectively), in which temperature difference is measured in ºC and time is measured in s. When heat flux is fixed, smaller temperature difference means higher heat transfer rate. Since the metal foam of 85% porosity has smaller temperature difference than the one of 95% porosity, it also has better heat transfer performance. This is reasonable, because a lower porosity means a higher percentage of the high-thermal conductivity metal material, which is helpful to transfer heat rapidly from the heating surface to the PCM.

In Figure 3.6, the temperature difference for both samples is 0 ºC at the start since the initial temperature distribution is uniform. When the heat flux q_w is applied, the temperature difference increases rapidly and then stays constant for a while until melting starts (t = 1000±150 s). Once melting starts, the temperature difference undergoes a steep

decrease, because the PCM around the heating wall is absorbing a large amount of heat to overcome latent heat, which has significantly delayed the temperature rise near the wall. When t = 1200±50 s, the PCM close to the wall has finished melting, leading to the rapid rise of the wall temperature. As time increases, more PCM is being melted. When t = 2000±50 s, all the PCM at $x \leq 8$ mm has finished melting, and the heat flux is mainly used to heat the PCM at $x > 8$ mm for phase change, which causes the temperature difference to keep relatively steady afterwards.

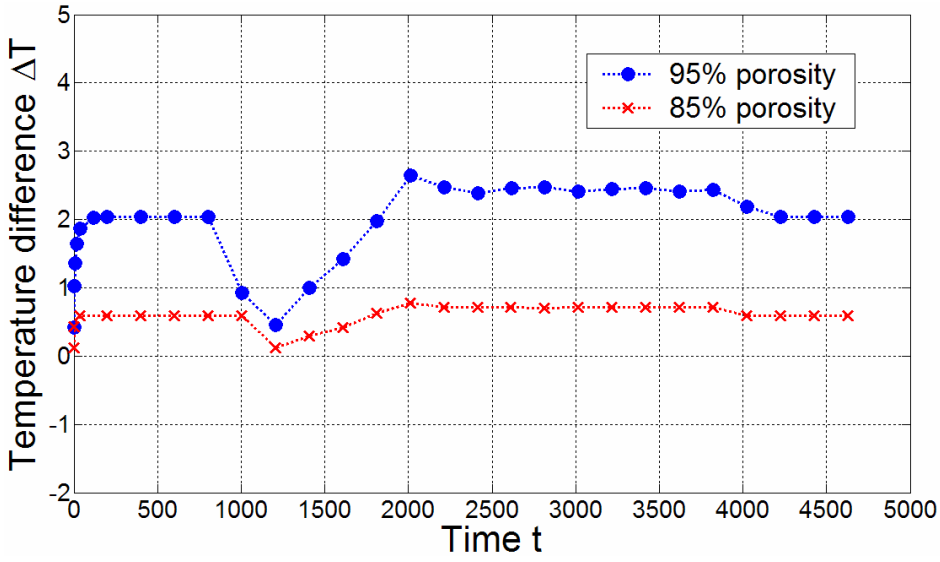

Figure 3.6. Comparison between two different metal foam samples.

- **Heat transfer enhancement by using metal foams**

Numerical simulation also obtained the temperature difference ΔT (ºC) in two metal-foam samples, shown in Figure 3.7. Smaller ΔT means higher heat transfer performance, because when heat flux is fixed heat transfer rate is proportional to $1/\Delta T$. Figure 3.7 shows that the ΔT in two metal-foam samples is much smaller than that in the pure PCM sample, with the former being only 5% to 20% of the latter. Thus, the heat conduction rate in metal-foam samples is 5–20 times higher than in the pure PCM sample. The conclusion can therefore be drawn that heat conduction of PCMs can be significantly enhanced by metal foams.

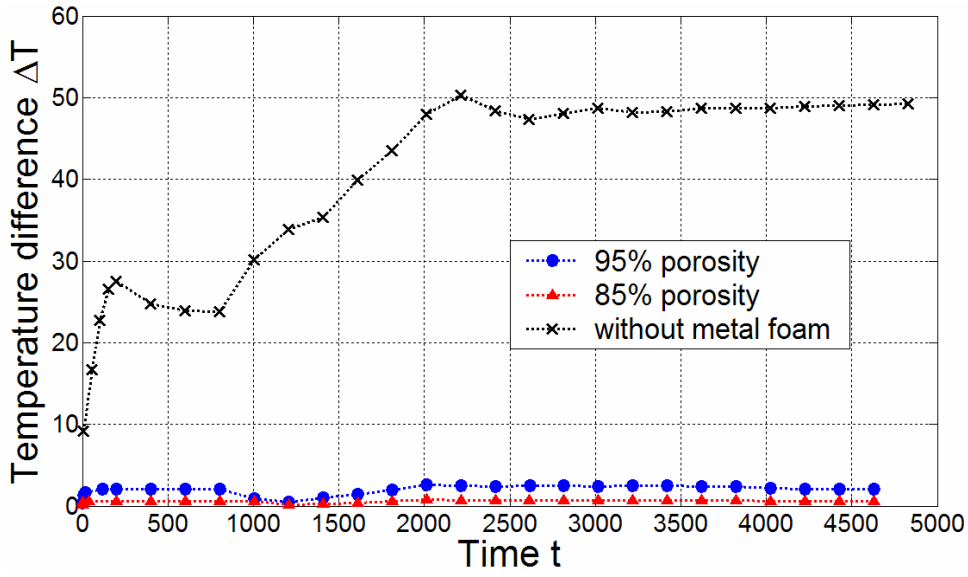

Figure 3.7. Heat transfer enhancement by metal foams.

3.1.7. Limitations

The above one-dimensional model is subject to a rather low accuracy. It cannot reflect the temperature difference between the PCM and the metal foam, nor the natural convection. The one-dimensional model only considers the effect of metal foam porosity (%), whilst

it neglects the effect of metal foam pore density (ppi). Therefore an investigation involving one more dimension becomes necessary. In Section 3.2, a two-dimensional heat conduction analysis will be presented, which employs a two-temperature model to consider the temperature difference between the PCM and the metal foam. To further reduce the model error, a two-dimensional natural convection study will be presented in Chapter 4.

3.2. Two-dimensional heat conduction

3.2.1. Problem description

As shown in Figure 3.8(a), the PCM-embedded metal foam is heated from the bottom boundary by a constant heat flux q_w, and loses heat to the ambiance through its left, right and top boundary, with the heat loss coefficients being h_1, h_2 and h_3, respectively. The sample dimensions are L_1 in the x-direction and L_2 in the y-direction. Different from the one-dimenionsal heat conduction discussed in Section 3.1, a control volume unit in the two-dimensional heat conduction has four neighbouring control volume units affecting its thermal state, thus making the process of equations solvation more time-consuming.

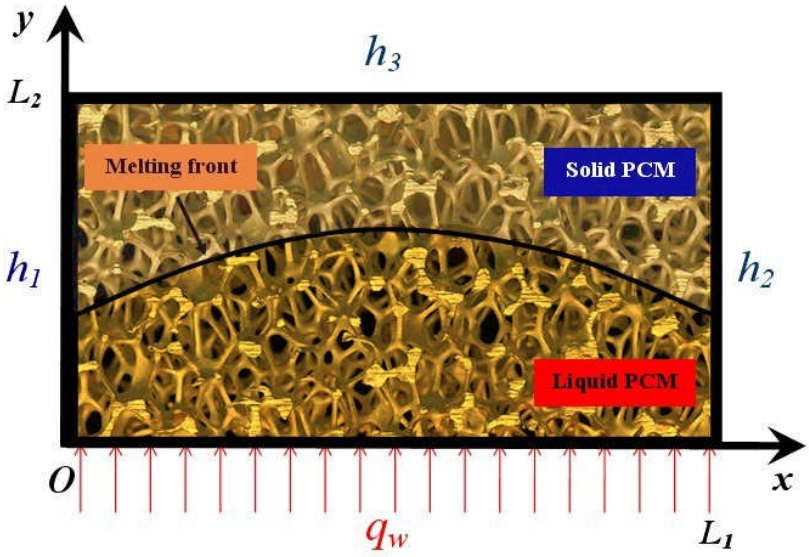

(a) Physical problem;

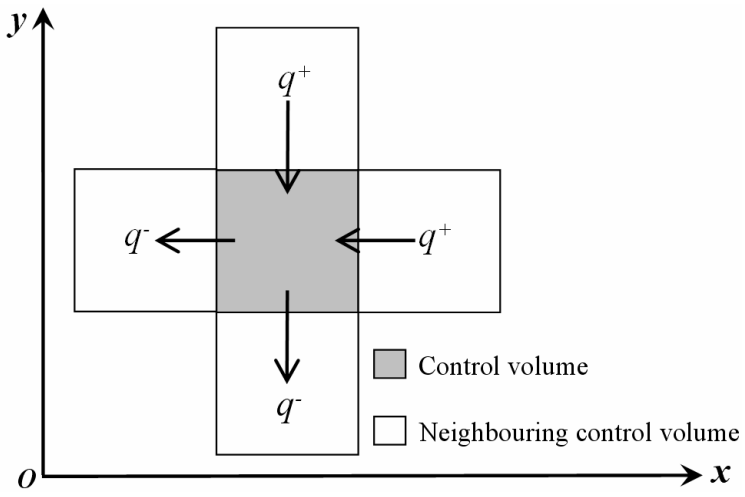

(b) Control volume

Figure 3.8. Two-dimensional heat conduction for the PCM-embedded metal foam.

3.2.2. Governing equations

A two-dimensional heat transfer analysis has been conducted for the PCM-embedded metal foam, without natural convection being considered. Eq. (3.9a) and Eq. (3.9b) are the governing equations for the metal foam and the PCM respectively (Tian and Zhao, 2009b).

$$(1-\varepsilon)\frac{\partial T_{MF}(x,y,t)}{\partial t}=\alpha_{MF}\left[\frac{\partial^2 T_{MF}(x,y,t)}{\partial x^2}+\frac{\partial^2 T_{MF}(x,y,t)}{\partial y^2}\right] -\frac{k_{int}}{\rho_{MF}C_{p.MF}}a_{sf}\frac{\left[T_{MF}(x,y,t)-T_{PCM}(x,y,t)\right]}{r_p} \tag{3.9a}$$

$$\varepsilon\frac{\partial T_{PCM}(x,y,t)}{\partial t}=\alpha_{PCM}\left[\frac{\partial^2 T_{PCM}(x,y,t)}{\partial x^2}+\frac{\partial^2 T_{PCM}(x,y,t)}{\partial y^2}\right] +\frac{k_{int}}{\rho_{PCM}C_{p.PCM}}a_{sf}\frac{\left[T_{MF}(x,y,t)-T_{PCM}(x,y,t)\right]}{r_p} \tag{3.9b}$$

where k_{int} is the interfacial heat transfer coefficient between the metal foam and the PCM, which is chosen as the thermal conductivity of the PCM because the main thermal resistance is on the PCM side; r_p is the effective pore radius, equal to half of the effective pore diameter d_p, which from Section 4.2.2 equals 0.0254 m/pore density; a_{sf} is the specific surface area of the metal foam, given by Eq. (4.15); α_{MF} is the thermal diffusivity of the metal foam, and α_{PCM} is the thermal diffusivity of the porous PCM. The calculating formulae of α_{MF} and α_{PCM} are given by:

$$\alpha_{MF}=\frac{\bar{k}_{MF}}{\rho_{MF}c_{p.MF}} \tag{3.10a}$$

$$\alpha_{PCM}=\frac{\bar{k}_{PCM}}{\rho_{PCM}c_{p.PCM}} \tag{3.10b}$$

where $\bar{k}_{MF}$ is the effective thermal conductivity of the metal foam when PCM is not saturated), $\bar{k}_{PCM}$ is the effective thermal conductivity of the porous PCM when not considering metal foam. They can be calculated by assigning $k_f = 0$ and $k_s = 0$ in Eq. (3.6), respectively (Tian and Zhao, 2009b; Tian and Zhao, 2011a).

In Eq. (3.9), the terms on the left hand side stand for the changing rates of the temperature (*T*) along with time *t*. They are caused by thermal diffusion (the first terms on the right hand side) and interstitial heat transfer (the second terms on the right hand side). The initial temperature of the system is T_0, shown in Eq. (3.11):

$$T_{MF}(x, y, 0) = T_{PCM}(x, y, 0) = T_0 \tag{3.11}$$

The PCM and metal foam are receiving a total amount of heat flux q_w at their common bottom boundary. However, the percentages of q_w need to be carefully decided for the PCM and metal foam. Calmidi and Mahajan (2000) employed an explicit presumption to decide the percentages: with PCM being $\bar{k}_{PCM} / (\bar{k}_{MF} + \bar{k}_{PCM}) \times 100\%$ and metal foam being $\bar{k}_{MF} / (\bar{k}_{MF} + \bar{k}_{PCM}) \times 100\%$. Such a presumption can make numerical simulations simpler and quicker, but meanwhile results in inaccuracy. To avoid such inaccuracy, exact percentages between the PCM and metal foam should be decided by an implicit relationship, which was proposed by Zhao et al. (2005) and further developed by Tian and Zhao (2011a), shown in Eq. (3.12):

$$\bar{k}_{MF} \frac{\partial T_{MF}(x, 0, t)}{\partial y} + \bar{k}_{PCM} \frac{\partial T_{PCM}(x, 0, t)}{\partial y} = -q_w \tag{3.12a}$$

$$T_{PCM}(x, 0, t) = T_{MF}(x, 0, t) \tag{3.12b}$$

Eq. (3.12b) shows the condition that the PCM and metal foam have the identical temperature at their common boundary.

The PCM temperature at the melting front is T_m:

$$T_{PCM}\left[S_x(y,t), S_y(x,t), t\right] = T_m \tag{3.13}$$

Eqs. (3.14a) and (3.14b) show the energy balance on the left boundary:

$$\bar{k}_{MF}\frac{\partial T_{MF}(0,y,t)}{\partial x} + h_1(1-\varepsilon)\left[T_\infty - T_{MF}(0,y,t)\right] = 0 \tag{3.14a}$$

$$\bar{k}_{PCM}\frac{\partial T_{PCM}(0,y,t)}{\partial x} + h_1\varepsilon\left[T_\infty - T_{PCM}(0,y,t)\right] = 0 \tag{3.14b}$$

Eqs. (3.15a) and (3.15b) show the energy balance on the right boundary:

$$-\bar{k}_{MF}\frac{\partial T_{MF}(L_1,y,t)}{\partial x} + h_2(1-\varepsilon)\left[T_\infty - T_{MF}(L_1,y,t)\right] = 0 \tag{3.15a}$$

$$-\bar{k}_{PCM}\frac{\partial T_{PCM}(L_1,y,t)}{\partial x} + h_2\varepsilon\left[T_\infty - T_{PCM}(L_1,y,t)\right] = 0 \tag{3.15b}$$

Eqs. (3.16a) and (3.16b) show the energy balance on the top boundary:

$$-\bar{k}_{MF}\frac{\partial T_{MF}(x,L_2,t)}{\partial y} + h_3(1-\varepsilon)\left[T_\infty - T_{MF}(x,L_2,t)\right] = 0 \tag{3.16a}$$

$$-\bar{k}_{PCM}\frac{\partial T_{PCM}(x,L_2,t)}{\partial y} + h_3\varepsilon\left[T_\infty - T_{PCM}(x,L_2,t)\right] = 0 \tag{3.16b}$$

The position function of the melting front *S(x, y, t)* has the following correlation with the temperature function $T_{PCM}(x, y, t)$:

$$\begin{aligned}\rho_{PCM}H_L\varepsilon\frac{d\left(S_x(y,t)\right)}{dt} &= \bar{k}_{PCM}\frac{\partial T_{PCM}(S_x(y,t)^+,y,t)}{\partial x} - \bar{k}_{PCM}\frac{\partial T_{PCM}(S_x(y,t)^-,y,t)}{\partial x} \\ &+ k_{int}a_{sf}\frac{d\left(S_x(y,t)\right)}{dt}\frac{\left[T_{MF}\left[S_x(y,t),y,t\right] - T_{PCM}\left[S_x(y,t),y,t\right]\right]}{r_p}\end{aligned} \tag{3.17a}$$

$$\rho_{PCM} H_L \varepsilon \frac{d\left(S_y(x,t)\right)}{dt} = \bar{k}_{PCM} \frac{\partial T_{PCM}(x, S_y(x,t)^+, t)}{\partial y} - \bar{k}_{PCM} \frac{\partial T_{PCM}(x, S_y(x,t)^-, t)}{\partial y} \quad (3.17b)$$
$$+ k_{int} a_{sf} \frac{d\left(S_y(x,t)\right)}{dt} \frac{\left[T_{MF}\left[x, S_y(x,t), t\right] - T_{PCM}\left[x, S_y(x,t), t\right]\right]}{r_p}$$

The position function *S(x, y, t)* has two components in the *x*-direction and the *y*-direction, which are shown in Eqs. (3.17a) and (3.17b), respectively. In these two equations, the term on the left hand side represents the marching speed of the melting front. The first two terms on the right hand side represent the net heat given by the neighbouring PCM. The third term on the right hand side represents the heat from the metal foam.

3.2.3. Numerical procedure

A Finite Difference Method (FDM)-based program was developed to deal with the phase change heat transfer problem in the PCM-embedded metal foam. The program was compiled and executed in Matlab®. Uniform mesh grids were employed: 14×112, i.e. 14 nodes in the *y*-direction (0.025 m) and 112 nodes in the *x*-direction (0.2 m). Iterations were automatically aborted when the maximum difference between two successive iterations is smaller than 10^{-6} (0.0001%). Mesh independence was also ensured, as the result shows that a finer mesh of 28×224 could only improve the numerical accuracy by 0.07%.

3.2.4. Numerical results and discussion

The numerical results are compared with the corresponding experimental data from Tian and Zhao (2009b), shown in Figure 3.9. The symbol "*y*" denotes the vertical coordinate of the computational domain, representing the distance of local positions from the heating wall. The PCM begins to melt at t = 1100±100 s and finishes phase change at t = 4500±100 s. Compared to the one-dimensional model shown in Figure 3.4, the two-dimensional model has achieved a better agreement with the corresponding

experimental data. Especially when melting finishes, the results from the two-dimensional model are much closer to the experimental data than the results from the one-dimensional model. Despite a better accuracy, small discrepancies still exist. The probable reason is that natural convection was neglected. More importantly, the PCM used in the experiment was RT58, which melts between 48 ºC and 62 ºC according to the PCM provider Rubitherm®. However, the PCM was assumed to have a constant melting point (58 ºC) in the numerical model, leading to a rather flat melting line in the numerical results. Experimental data indicates that the PCM starts melting at 48 ºC, the place where the numerical results deviate from experimental data, because latent heat starts taking effect and delays the temperature rise whilst in the numerical model the PCM temperature is still rising (sensible heat taking effect since below 58 ºC).

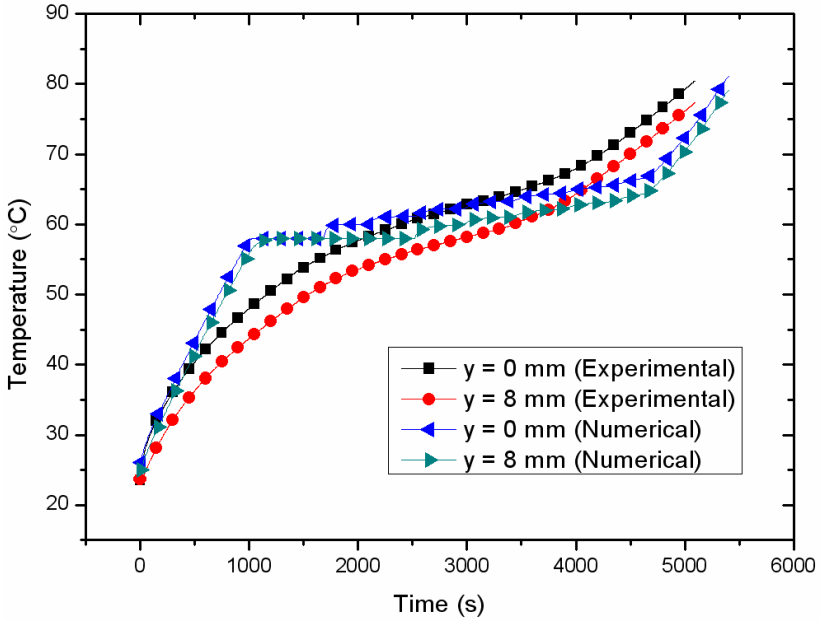

Figure 3.9. Comparison between numerical results and experimental data (two-dimensional heat conduction).

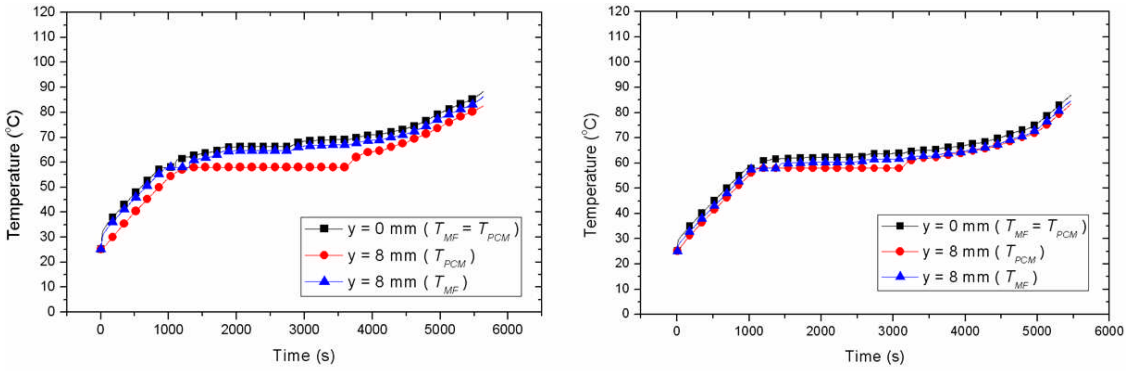

Figure 3.10. Comparison between two metal foam samples with different pore density: (a) 10 ppi; (b) 30 ppi.

Figure 3.10 shows a comparison between two metal foam samples with the same porosity (95%) but different pore density: 10 ppi and 30 ppi. In Figure 3.10, T_{MF} denotes the metal foam temperature and T_{PCM} denotes the PCM temperature. PCM has the same temperature as metal foam at the bottom boundary (heating wall) as assumed in Eq. (3.12b). The temperature difference between PCM and metal foam is smaller in the 30 ppi sample than in the 10 ppi sample, meaning that the thermal communication in the 30 ppi sample is better than that in the 10 ppi sample. The metal foam sample of 30 ppi has finer pores and larger specific surface area than the one of 10 ppi, resulting in the former having better heat transfer than the latter.

Figures 3.11(a)–(d) show the evolution of the two-dimensional temperature profiles during melting process for the metal foam of 95% porosity and 10 ppi. As seen in Figure 3.11, the sample is 0.2 m in the *x*-direction and 0.025 m in the *y*-direction. Temperatures

are represented by different colours. The numbers on the isotherms denote the local temperature (in ºC).

Figure 3.11(a) shows the temperature profiles at t = 966 s. At this time, the maximum temperature of the PCM in the whole region is 57.5 ºC which is still below the melting point (58 ºC). As time increases, PCM begins to melt from the bottom boundary where the heat flux is exerted. When t = 2146 s, nearly 40% of the whole PCM has finished melting, illustrated by the area below the 58 ºC isotherm line shown in Figure 3.11(b). As time increases further, the melting front gradually moves upwards, meaning more PCM is being melted, shown in Figure 3.11(c). The PCM temperature profiles when t = 4888 s are shown in Figure 3.11(d). At this time, all the PCM has been fully heated into liquid state, with the minimum and maximum temperature being 60 ºC and 71 ºC respectively.

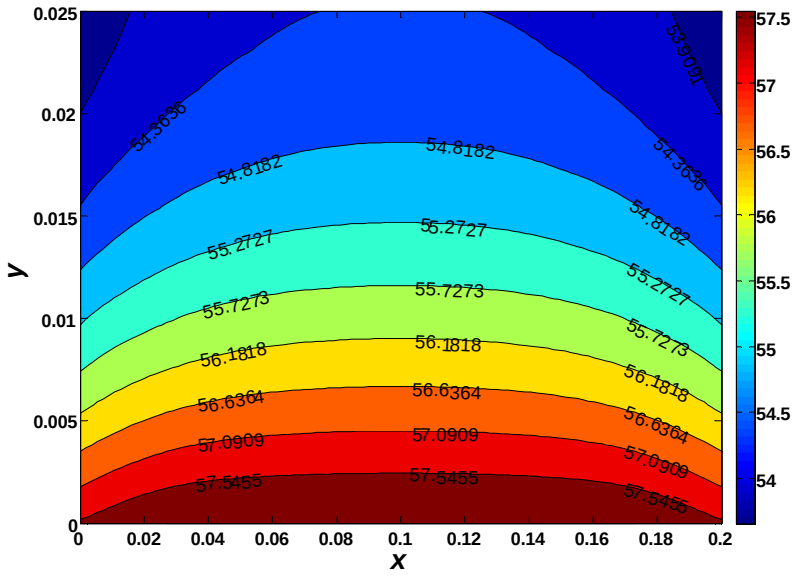

(a) t = 966 s

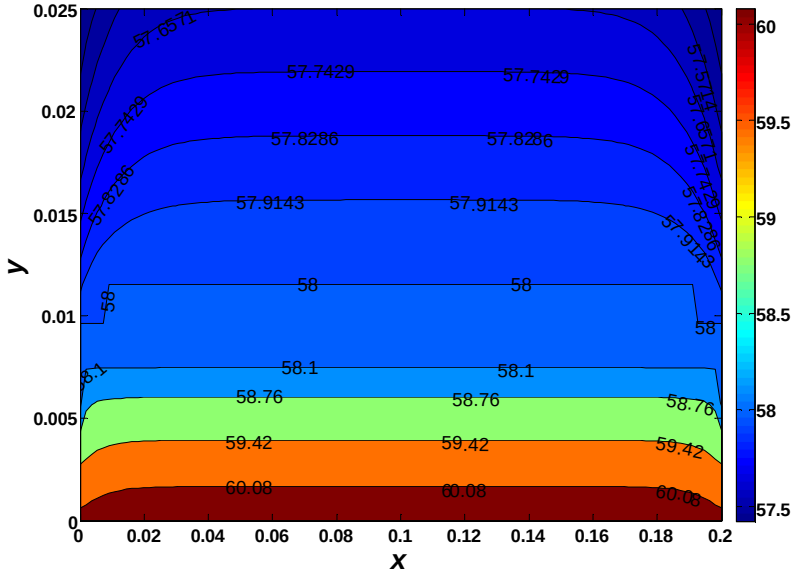

(b) t = 2146 s

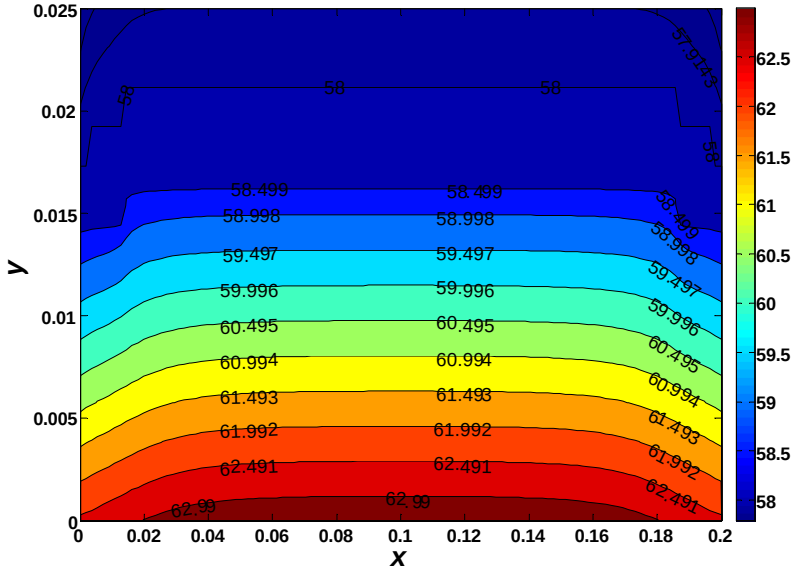

(c) t = 3219 s

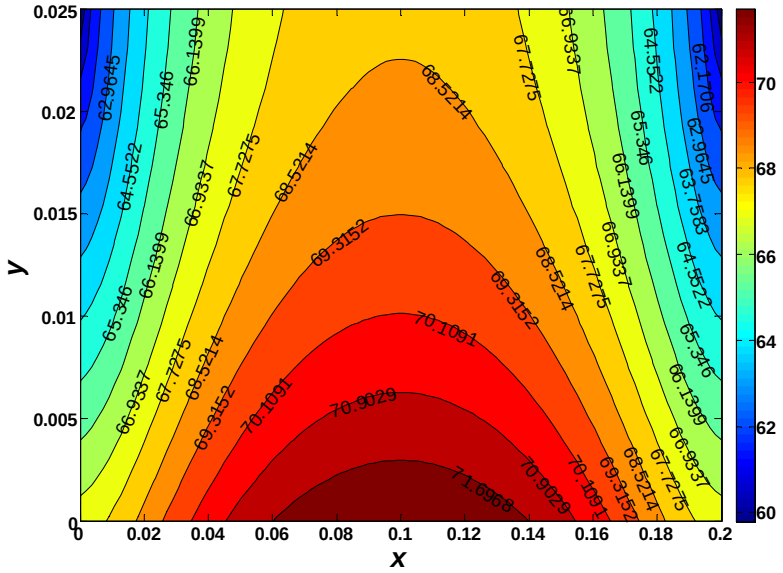

(d) t = 4888 s

Figure 3.11. Temperature profiles (two-dimensional heat conduction).

3.3. Conclusion

In this Chapter, heat conduction was examined for PCM-embedded metal foams. The one-dimensional and the two-dimensional model both achieved a fairly good agreement with the corresponding experimental data. The one-dimensional investigation treated the PCM and metal foam with the same temperature. This does not conform to the real case, and was improved by the two-dimensional investigation, which employs the two-equation non-thermal equilibrium model to consider the temperature difference between the PCM and the metal skeleton.

It was found that the addition of metal foams can significantly reduce the temperature difference in PCMs and therefore enhance the heat conduction rate by 5–20 times compared to the case without metal foams. Numerical results also showed that the metal foams of smaller porosity and larger pore density can achieve even better heat transfer performance than those of larger pore size and porosity.

Chapter 4. Natural Convection

Apart from heat conduction, natural convection is the other important heat transfer mode in PCM-embedded metal foams. In this Chapter, a two-dimensional thermal study of coupled heat conduction and natural convection is presented for PCM-embedded metal foams, and the effects of metal foams on heat transfer enhancement are investigated theoretically and experimentally. The numerical investigation is based on the high-accuracy two-equation non-equilibrium heat transfer model, with numerical results being validated by experimental data.

4.1. Problem description

The physical problem to be tackled is illustrated in Figure 4.1. The PCM, after being heated to liquid, is embedded into a piece of rectangular copper foam. The PCM and the foam are heated from the bottom side through a constant heat flux q_w provided by an electric heater. Because perfect insulation is hard to achieve in real applications, they lose heat to the atmosphere through the left, right and top boundaries, with heat loss coefficients h_1, h_2 and h_3 respectively. The curve in Figure 4.1 represents the melting front of the PCM during phase change. Within the area below this curve, the PCM has been fully melted into the liquid state (natural convection occurs, illustrated by the red dashed circles), whilst within the area above this curve the PCM is still in the solid state (natural convection does not occur).

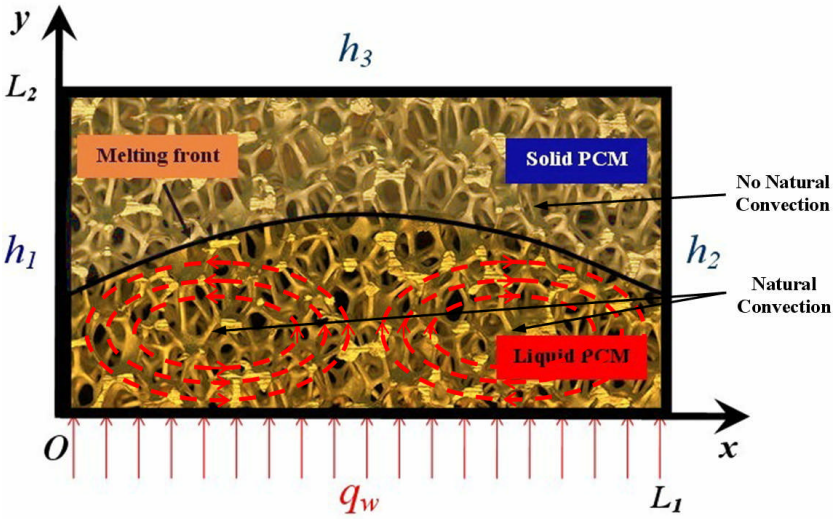

Figure 4.1. Natural convection for the PCM-embedded metal foam.

4.2. Mathematical model

Transport phenomena, such as fluid flow and heat transfer, are rather difficult to be quantified in porous media because of their complicated porous structures. The volume-averaging method is usually employed by researchers when modelling transport phenomena in porous media. Volume-averaging method treats porous media as a continuous structure comprising many Representative Elementary Volumes (REVs) (Tian, 2012). Most porous media have at least two components (solid frame saturated by air/water or other materials). Porous media have irregular structures inside and therefore are heterogeneous, but they can be homogeneous if looked macroscopically. REV is the differentiation volume unit in porous media beyond which the physical properties of the porous media become homogeneous. Introduction of REV allows researchers to extend the models used in continuum theory to porous media. The size of an REV should be much larger than the characteristic pore size, so that a function f can have a reliable average value over a whole REV (Whitaker, 1969): the volume-averaged value fluctuates

when the selected REV is not large enough. The size of an REV should also be much smaller than the porous media macroscopic size, so that the differential equations that are used to describe transport phenomena in porous media can be applied to an REV (Whitaker, 1969). The volume-averaged value $<f>_{REV}$ of any function f over an REV is given by:

$$\langle f \rangle_{REV} = \frac{1}{V_{REV}} \int_{REV} f dV \tag{4.1}$$

where $\langle\ \rangle$ denotes the volume-averaged value of a certain function over an REV.

4.2.1 Equations of fluid dynamics

Based on such a volume-averaging technique, the classical continuity equation can be written as:

$$\nabla \bullet \langle \mathbf{V} \rangle = \mathbf{0} \tag{4.2}$$

$\langle\ \rangle$ denotes the volume-averaged value of the velocity function over a metal foam REV (Representative Elementary Volume inside metal foams) (Calmidi, 1998; Tian and Zhao, 2011a). The continuity equation takes on different forms under different coordinate systems, and its form under the Cartesian coordinate system can be written by:

$$\frac{\partial u}{\partial x} + \frac{\partial v}{\partial y} = 0 \tag{4.3}$$

where u and v denote the components of the velocity $\mathbf{V}$ in the x-direction and in the y-direction respectively.

Darcy's Law has been used to describe fluid flow in porous media for over a hundred years; however, its application has been restricted to seepage flow where the flow velocity is rather low. Fluid flow in metal foams is usually at a much higher flow rate due to high porosities (85% and higher), resulting in the non-Darcy effects of viscous flow

resistance and inertia flow resistance (Tian, 2012). To consider these non-Darcy effects, correction terms have been introduced, and these include Brinkman correction for viscous effects (Brinkman, 1947) and Forchheimer correction for inertia effects (Forchheimer, 1901). Brinkman-Forchheimer extended Darcy equations for metal foams take on the following form:

$$\begin{aligned} &\frac{1}{\varepsilon}\langle\rho_{PCM}\rangle\frac{\partial\mathbf{V}}{\partial t}+\frac{\langle\rho_{PCM}\rangle}{\varepsilon^2}\langle(\mathbf{V}\bullet\nabla)\mathbf{V}\rangle= \\ &-\nabla\langle p\rangle+\frac{\mu_{PCM}}{\varepsilon}\nabla^2\langle\mathbf{V}\rangle-\frac{\mu_{PCM}}{K}\langle\mathbf{V}\rangle-\frac{\rho_{PCM}C_f}{\sqrt{K}}\|\langle\mathbf{V}\rangle\|\langle\mathbf{V}\rangle+\langle\rho_{PCM}\rangle\mathbf{g} \end{aligned} \tag{4.4}$$

where $\|\ \|$ denotes the norm of a vector, $\mathbf{g}$ denotes the gravity vector, ε denotes the porosity of the metal foam, μ_{PCM} denotes the dynamic viscosity of the PCM, ρ_{PCM} denotes the density of the PCM, K is the permeability coefficient for homogeneous metal foams, which can be a vector/tensor for anisotropic materials, and C_f denotes the inertial factor for fluid flow in metal foams.

Eq. (4.4) takes on the following forms under the Cartesian coordinate system:

$$\begin{aligned} &\rho_{PCM}\frac{\partial u}{\partial t}+\frac{\rho_{PCM}}{\varepsilon}\left(u\frac{\partial u}{\partial x}+v\frac{\partial u}{\partial y}\right)= \\ &-\frac{\partial p}{\partial x}+\frac{\mu_{PCM}}{\varepsilon}\left(\frac{\partial^2 u}{\partial x^2}+\frac{\partial^2 u}{\partial y^2}\right)-\frac{\mu_{PCM}}{K}u-\frac{\rho_{PCM}C_f}{\sqrt{K}}|u|u \end{aligned} \tag{4.5}$$

$$\begin{aligned} &\rho_{PCM}\frac{\partial v}{\partial t}+\frac{\rho_{PCM}}{\varepsilon}\left(u\frac{\partial v}{\partial x}+v\frac{\partial v}{\partial y}\right)= \\ &-\frac{\partial p}{\partial y}+\frac{\mu_{PCM}}{\varepsilon}\left(\frac{\partial^2 v}{\partial x^2}+\frac{\partial^2 v}{\partial y^2}\right)-\frac{\mu_{PCM}}{K}v-\frac{\rho_{PCM}C_f}{\sqrt{K}}|v|v+\rho_{PCM}g\varepsilon\beta(T_{PCM}-T_{ref}) \end{aligned} \tag{4.6}$$

Eqs. (4.5) and (4.6) give the momentum equations of the velocity $\mathbf{V}$ in the x-direction and the y-direction respectively. Here, $|\ |$ denotes the modulus of a variable, β denotes the

thermal expansion coefficient of the PCM and T_{PCM} denotes the temperature of the PCM. The last term on the right hand side of Eq. (4.6) represents the buoyancy force caused by temperature differences of the PCM, and it is the driving force of the natural convection. The intensity of the natural convection in the PCM mainly depends on its driving force and its resisting force. The driving force increases with increasing temperature differences, whilst the resisting force can be reduced by decreasing the viscosity μ_{PCM} of the PCM. With fixed temperature differences, the latter results in natural convection weakening when the viscosity of the PCM is increased. When the PCM is still in solid state, its viscosity is infinite, so that natural convection does not take place, but as the PCM becomes liquid after melting finishes, the viscosity falls rapidly, so that natural convection can take place.

4.2.2 Determination of permeability and inertia factor

By employing data fitting technology, Calmidi and Mahajan (2000) obtained empirical formulae for permeability and inertial factor of metal foams. Since their results showed good agreement with test data, this Chapter has employed their formulae, with Eq. (4.7) showing permeability and Eq. (4.8) showing inertial factor respectively:

$$\frac{K}{d_p^{\,2}} = 0.00073\left(1-\varepsilon\right)^{-0.224}\left(\frac{d_f}{d_p}\right)^{-1.11} \tag{4.7}$$

$$C_f = 0.00212\left(1-\varepsilon\right)^{-0.132}\left(\frac{d_f}{d_p}\right)^{-1.63} \tag{4.8}$$

where d_p denotes the equivalent diameter of metal foam cells, which can be calculated if knowing the pore density: d_p = 0.0254 m/pore density. Pore density reflects the pore size of metal foam cells and is measured in ppi (pores per inch: 1 inch = 2.54 cm); d_f denotes the equivalent diameter of metal foam fibres, calculated from Calmidi (1998):

$$\frac{d_f}{d_p} = 1.18\sqrt{\frac{1-\varepsilon}{3\pi}}\left(\frac{1}{1-e^{-(1-\varepsilon)/0.04}}\right) \tag{4.9}$$

To give more accurate results, Eq. (4.9) has taken into account the non-circular shape of metal fibres by introducing a shape factor, which is shown within the brackets in Eq. (4.9). When calculating the metal fibre diameters, errors caused by the non-circular effect can be as large as 40.2% for the metal foam with 95% porosity, but only 8.9% for 90% porosity and 2.4% for 85% porosity (Tian 2012).

4.2.3 Equations of phase change heat transfer

In order to cope with the phase change heat transfer problem, the Enthalpy Method has been employed in this study (Tian and Zhao 2011a). The relationship between PCM enthalpy function $H_{PCM}(x, y, t)$ and temperature $T_f(x, y, t)$ is given by:

$$T_{PCM} = \begin{cases} \dfrac{H_{PCM}}{c_{p.PCM}}, & H_{PCM} \in (-\infty, c_{p.PCM} T_m) \\ T_m, & H_{PCM} \in [c_{p.PCM} T_m, c_{pf} T_m + H_L] \\ \dfrac{H_{PCM} - H_L}{c_{p.PCM}}, & H_{PCM} \in (c_{p.PCM} T_m + H_L, +\infty) \end{cases} \tag{4.10}$$

The energy equation for the metal foam (Tian and Zhao, 2011a) is given by:

$$\begin{aligned} \langle \rho_{MF} \rangle c_{p.MF} \frac{\partial \langle T_{MF}(x,y,t) \rangle}{\partial t} &= \left\langle \nabla \bullet \left[\bar{\bar{k}}_{MF} \nabla \langle T_{MF}(x,y,t) \rangle \right] \right\rangle \\ &- h_{sf} a_{sf} \left[\langle T_{MF}(x,y,t) \rangle - \langle T_{PCM}(x,y,t) \rangle \right] \end{aligned} \tag{4.11}$$

With the enthalpy method being used in this Chapter, the energy equation for the PCM is given by:

$$\frac{\partial \langle H_{PCM}(x,y,t)\rangle}{\partial t} + \langle \rho_{PCM} \rangle c_{p.PCM} \mathbf{V} \bullet \nabla \langle T_{PCM}(x,y,t)\rangle = \left\langle \nabla \bullet \left[\bar{k}_{PCM} \nabla \langle T_{PCM}(x,y,t)\rangle \right] \right\rangle + h_{sf} a_{sf} \left[\langle T_{MF}(x,y,t)\rangle - \langle T_{PCM}(x,y,t)\rangle \right] \tag{4.12}$$

In Eqs. (4.11) and (4.12), $\bar{k}_{MF}$ is the effective thermal conductivity of the metal foam when PCM is not saturated, and $\bar{k}_{PCM}$ is the effective thermal conductivity of the porous PCM when metal foam is removed. Details of their calculation are given in Section 3.2.2 of Chapter 3. h_{sf} is the inter-phase heat transfer coefficient between metal ligaments and PCM, a_{sf} is specific surface area of the metal foam, and their calculation formulae are given in Section 4.2.4.

Within Cartesian coordinate system, the above energy equations for the metal foam and the PCM are given by Eq. (4.13) and Eq. (4.14) respectively:

$$\rho_{MF} c_{p.MF} (1-\varepsilon) \frac{\partial T_{MF}}{\partial t} = \bar{k}_{MF} \left(\frac{\partial^2 T_{MF}}{\partial x^2} + \frac{\partial^2 T_{MF}}{\partial y^2} \right) - h_{sf} a_{sf} \left[T_{MF} - T_{PCM} \right] \tag{4.13}$$

$$\varepsilon \frac{\partial H_{PCM}}{\partial t} + \rho_{PCM} c_{p.PCM} \varepsilon \left(u \frac{\partial T_{PCM}}{\partial x} + v \frac{\partial T_{PCM}}{\partial y} \right) = \bar{k}_{PCM} \left(\frac{\partial^2 T_{PCM}}{\partial x^2} + \frac{\partial^2 T_{PCM}}{\partial y^2} \right) + h_{sf} a_{sf} \left[T_{MF} - T_{PCM} \right] \tag{4.14}$$

4.2.4. Determination of specific surface area and inter-phase heat transfer coefficient

The surface area density of metal foams a_{sf} is defined as the total surface area (m^2) of metal fibres within unit volume of metal foam matrix (m^3), and it can be obtained by assuming that all metal fibres have an ideal cylindrical shape (a shape factor was also introduced by Calmidi and Mahajan (2000) to consider the non-circularity):

$$a_{sf} = \frac{3\pi d_f \left(1 - e^{-\left((1-\varepsilon)/0.04\right)} \right)}{\left(0.59 d_p \right)^2} \tag{4.15}$$

where h_{sf} represents the inter-phase heat transfer coefficient between the metal foam struts and PCM. Because the metal foam struts were assumed to have the shape of cylinders, its value can be approximately (uncertainty ±15%) calculated by the empirical formulae for the flow across a bank of cylinders (Zukauskas, 1987):

$$Nu_{sf} = \frac{h_{sf} d}{k_f} = 0.76 \mathrm{Re}_d^{0.4} \mathrm{Pr}^{0.37}, \left(1 \le \mathrm{Re}_d \le 40\right) \tag{4.16a}$$

$$Nu_{sf} = \frac{h_{sf} d}{k_f} = 0.52 \mathrm{Re}_d^{0.5} \mathrm{Pr}^{0.37}, \left(40 \le \mathrm{Re}_d \le 1000\right) \tag{4.16b}$$

$$Nu_{sf} = \frac{h_{sf} d}{k_f} = 0.26 \mathrm{Re}_d^{0.6} \mathrm{Pr}^{0.37}, \left(1000 \le \mathrm{Re}_d \le 2 \times 10^5\right) \tag{4.16c}$$

In Eqs. (4.16a) – (4.16c), Re_d is the Reynolds number, in which the characteristic diameter d is chosen as the effective diameter of the metal fibres d_f (Lu et al., 2007; Tian, 2012). The calculating formula for d_f was given in Eq. (4.9).

4.2.5. Initial and boundary conditions

The initial and boundary conditions for u, v, T_{MF}, T_{PCM} are shown in the following equations. Eq. (4.17) gives the velocity boundary conditions, which can be obtained from the non-slip law for viscous fluids. Eq. (4.18) gives the initial conditions of the thermal system.

The boundary conditions (for temperature) are given by Eqs. (4.19) and (4.20) (the lower boundary, which is the heating surface), Eqs. (4.21) and (4.22) (the left boundary), Eqs. (4.23) and (4.24) (the right boundary) and Eqs (4.25) and (4.26) (the upper boundary).

$$u, v\big|_{x=0, L_1} = 0, \; u, v\big|_{y=0, L_2} = 0 \tag{4.17}$$

$$u, v\big|_{t=0} = 0,\ T_{MF}\big|_{t=0} = T_{PCM}\big|_{t=0} = T_0 \tag{4.18}$$

$$\bar{k}_{MF}\left.\frac{\partial T_{MF}}{\partial y}\right|_{y=0} + \bar{k}_{PCM}\left.\frac{\partial T_{PCM}}{\partial y}\right|_{y=0} = -q_w \tag{4.19}$$

$$T_{PCM}\big|_{y=0} = T_{MF}\big|_{y=0} \tag{4.20}$$

$$\bar{k}_{MF}\left.\frac{\partial T_{MF}}{\partial x}\right|_{x=0} + h_1(1-\varepsilon)\left[T_\infty - T_{MF}\big|_{x=0}\right] = 0 \tag{4.21}$$

$$\bar{k}_{PCM}\left.\frac{\partial T_{PCM}}{\partial x}\right|_{x=0} + h_1\varepsilon\left[T_\infty - T_{PCM}\big|_{x=0}\right] = 0 \tag{4.22}$$

$$-\bar{k}_{MF}\left.\frac{\partial T_{MF}}{\partial x}\right|_{x=L_1} + h_2(1-\varepsilon)\left[T_\infty - T_{MF}\big|_{x=L_1}\right] = 0 \tag{4.23}$$

$$-\bar{k}_{PCM}\left.\frac{\partial T_{PCM}}{\partial x}\right|_{x=L_1} + h_2\varepsilon\left[T_\infty - T_{PCM}\big|_{x=L_1}\right] = 0 \tag{4.24}$$

$$-\bar{k}_{MF}\left.\frac{\partial T_{MF}}{\partial y}\right|_{y=L_2} + h_3(1-\varepsilon)\left[T_\infty - T_{MF}\big|_{y=L_2}\right] = 0 \tag{4.25}$$

$$-\bar{k}_{PCM}\left.\frac{\partial T_{PCM}}{\partial y}\right|_{y=L_2} + h_3\varepsilon\left[T_\infty - T_{PCM}\big|_{y=L_2}\right] = 0 \tag{4.26}$$

4.3. Numerical procedure

A Finite Volume Method (FVM)-based program was developed to solve the governing equations in Section 4.2. The program was compiled and executed in Visual Fortran®. The SIMPLER algorithm (Semi-Implicit Method for Pressure Linked Equations Revised) was employed because it was found to have much higher convergence rate (Tian and Zhao, 2011a) than the SIMPLE algorithm (Semi-Implicit Method for Pressure Linked Equations). Both the SIMPLER and the SIMPLE algorithms were proposed by Patankar (1980) to solve the flow problems for incompressible fluids. All numerical simulations

were conducted in a uniform mesh of 50×200. There were 50 computational nodes in the *y*-direction (0.025 m in total, 0.0005 m for each node), and 200 computational nodes in the *x*-direction (0.2 m in total, 0.001 m for each node). The independence of the accuracy of the numerical solution on the mesh size was also examined, and it was found that the 50×200 mesh can ensure that the numerical solution is mesh-independent, meaning the calculation accuracy cannot be further improved by using a finer mesh grid.

The numerical programming needs to ensure that natural convection only takes place at the grids where the PCM is in its liquid state and does not take place at the grids where the PCM is still in its solid state. This is realised by only assigning the real viscosity value to the grids where the PCM is liquid whilst assigning a viscosity with the value of 10^{10} to the grids where the PCM is still solid.

4.4. Results and discussion

4.4.1. Experimental test rig and results

The experiment setup is illustrated in Figure 4.2. The test section comprises a piece of rectangular metal foam (copper foam with the dimension of 200×120×25 mm) with paraffin wax RT58 embedded in it. According to the PCM provider Rubitherm®, the thermo-physical properties of RT58 are melting temperature: 48 ºC to 62 ºC, latent heat of fusion: 181 kJ/kg, specific heat: 2.1 kJ/kg, dynamic viscosity: 0.0269 Pa·s, thermal conductivity: 0.2 W/(m K), thermal expansion coefficient: 1.1×10^{-4} K^{-1}. The metal foam was sintered onto a thin copper plate from the bottom side for better thermal contact. Attached to the copper plate was an electrical heater which is made of flexible silicon with adjustable heat flux, providing continuous and uniform heat flux for the PCM and metal foam. The heater input power can be precisely controlled and measured by a Variac and an electrical power meter (Hameg HM8115-2, accuracy ±0.5%). This allows the heat flux used in the test to be calculated through dividing the input power by the surface area

of the copper plate.

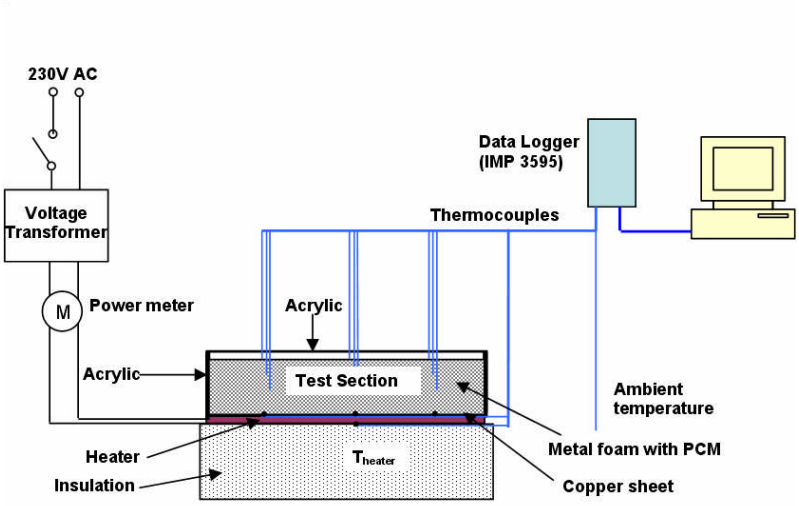

Figure 4.2. Test rig.

In the test, nine thermocouples (accuracy ±0.1 ºC) were placed at different locations (y = 8 mm, 16 mm and 24 mm respectively, three thermocouples (at x = 50 mm, 100 mm and 150 mm respectively) were used for each place to get more reliable readings) inside the PCM to monitor the transient temperature variation. Here, y denotes the distance between different locations and the heating plate. Another three thermocouples were placed on the copper plate to record the plate temperatures (y = 0 mm). Although perfect insulation cannot be guaranteed in the test, the underneath of the heating surface was insulated with Armflex insulation material and other surfaces were insulated by acrylic sheets, which were transparent for observation during the tests. The temperatures and the input power were automatically recorded by a data acquisition system. The uncertainty of the test was also examined by using Eq. (4.27). The total uncertainty can be attributed to inaccuracies of measurement for input heat flux and temperature, as well as heat loss. With δT_{TC} being ±0.1ºC (±0.43%) for thermocouples, δT_{IMP} being ±0.3ºC (±1.30%) for the temperature measurement tolerance of IMP3595, the uncertainty of power meter being

±0.5%, q_{LOSS} being estimated at 2.5 W according to a heat loss coefficient of 3 W/m K for natural convection of air, and q_T being 38.4 W (1.6 KW/m^2), the overall uncertainty of the test was estimated at 6.67% by using Eq. (4.27).

$$U_T = \sqrt{\left(\frac{\delta T_{TC}}{T_{TC}}\right)^2 + \left(\frac{\delta T_{IMP}}{T_{IMP}}\right)^2 + \left(\frac{\delta q_{PM}}{q_{PM}}\right)^2 + \left(\frac{q_{LOSS}}{q_T}\right)^2} \times 100\% \qquad (4.27)$$

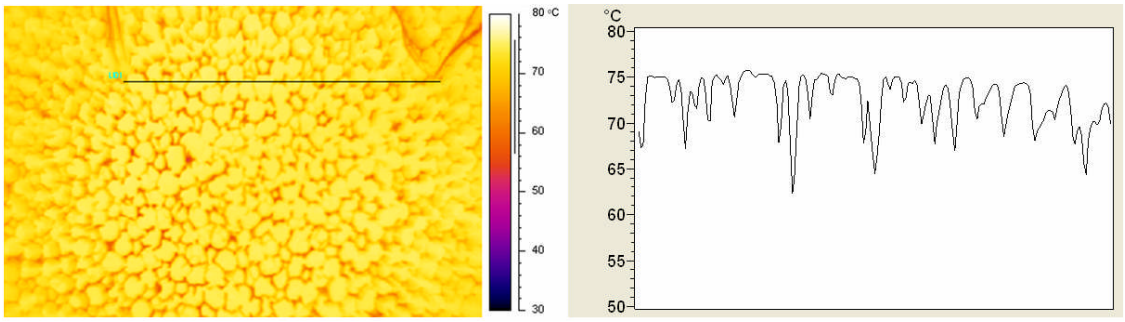

(a) (b)

Figure 4.3. Infrared camera image.

Prior to the more accurate temperature measurements using thermocouples, a thermal picture is taken by using an infrared camera (Therma CAM^{TM}, FLIR A40), shown in Figure 4.3. The picture shows the full liquid state of paraffin, as the temperature is above the melting temperature. The metal foam open cells can be seen in Figure 4.3(a). Figure 4.3(b) shows the temperature variation along the line drawn in Figure 4.3(a). Due to the non-negligible difference between the paraffin and metal foam solid structures, the temperature exhibits periodic variation. In the experiment, the tiny thermocouple probes were placed inside the metal foam pores (to measure PCM temperature) instead of contacting the metal frame. Although this was difficult to achieve, the high porosity of metal foams made it much easier because 95% porosity would mean that the chance of a thermocouple probe contacting the metal frame is only 5%. In addition, the temperature

reading gets unreasonably high if the probe accidentally contacts the metal frame, in which case the data acquisition system can be programmed to eliminate wrong data and warn the experimenter of a bad thermocouple contact.

The comparison between the pure RT58 sample and two metal-foam samples during melting process (charging) is shown in Figure 4.4 ($\Delta T = T_{y=0\,mm} - T_{y=8\,mm}$), from which it can be seen that the heat transfer enhancement of metal foam on solid/liquid phase change heat transfer in PCM is very significant compared to the results of the pure PCM sample, especially at the solid zone. The heat transfer rate can be enhanced by 5–20 times. In the pure PCM sample, when the PCM starts melting natural convection takes place thereby reducing the temperature difference between the heating wall and the PCM, which improves the heat transfer performance. The large flow resistance caused by metal foam suppresses natural convection in two metal-foam samples. Even so, the addition of the metal foam can still increase the overall heat transfer rate by 3–10 times (depending on the metal foam structures) during the melting process (two-phase zone) and the liquid zone. It can also be concluded from Figure 4.4 that the metal foam sample with smaller porosity has better heat transfer performance than the one with larger porosity. This is reasonable because smaller porosity means a larger percentage of metal skeletons, which is helpful for transferring heat to the PCM more rapidly.

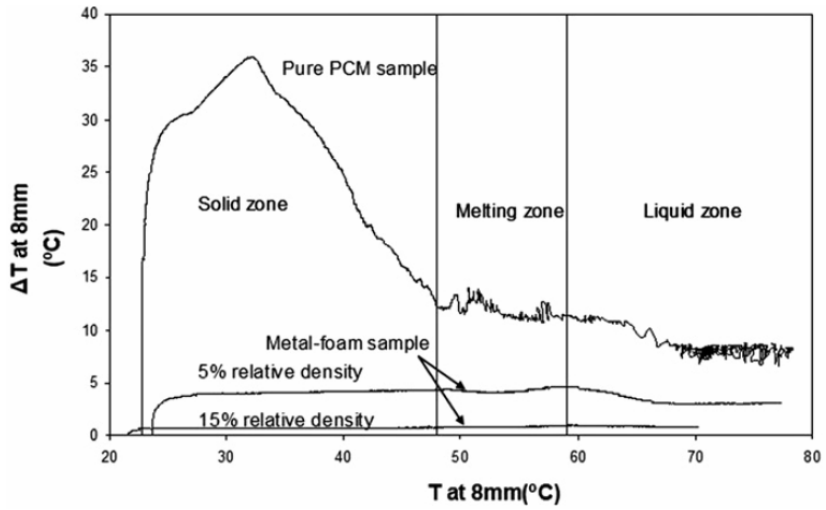

Figure 4.4. Comparison between the pure PCM sample and two metal-foam samples.

4.4.2 Comparison between experimental data and numerical results

The numerical results and the corresponding experimental data are compared in Figure 4.5, which shows the temperatures at y = 0 mm and 8 mm. y is the vertical coordinate in the computational domain shown in Figure 4.1, namely the distance between different locations and the heating plate. Both numerical results and experimental data show that the PCM begins to melt around t = 1100 s and finishes phase change around t = 4000 s. Compared to the results shown in Figure 3.9 where natural convection has been neglected, the numerical results shown in Figure 4.5 have achieved a better agreement with experimental data, because natural convection has been included in the current model. Although a better agreement is achieved, there are still small discrepancies between numerical results and experimental data at t = 1100±500 s. Such discrepancies cannot be eliminated because in the mathematical model it has been assumed that the PCM has a fixed melting point of 58 ºC, similarly to crystal materials. In practice, it is important to note that the PCM used in the experiment was RT58 and it melts in a temperature range of 48 ºC to 62 ºC according to Rubitherm®. Some crystal salt hydrates, like $MnCl_2 \cdot 4H_2O$

and $MgCl_2 \cdot 4H_2O$ (Sharma et al., 2009), have a fixed melting point of 58 ºC. However, the reason why they were not used in the experiment was that they have very severe problems such as phase separation and super-cooling.

As shown in Figure 4.5, the PCM temperatures increase more slowly after melting begins, because the heat provided is mainly used for phase change rather than increasing sensible heat. After the PCM has become fully liquid (when temperatures are higher than 62 ºC), its temperature begins to increase rapidly again, because the heat provided is now all used for increasing sensible heat of the PCM.

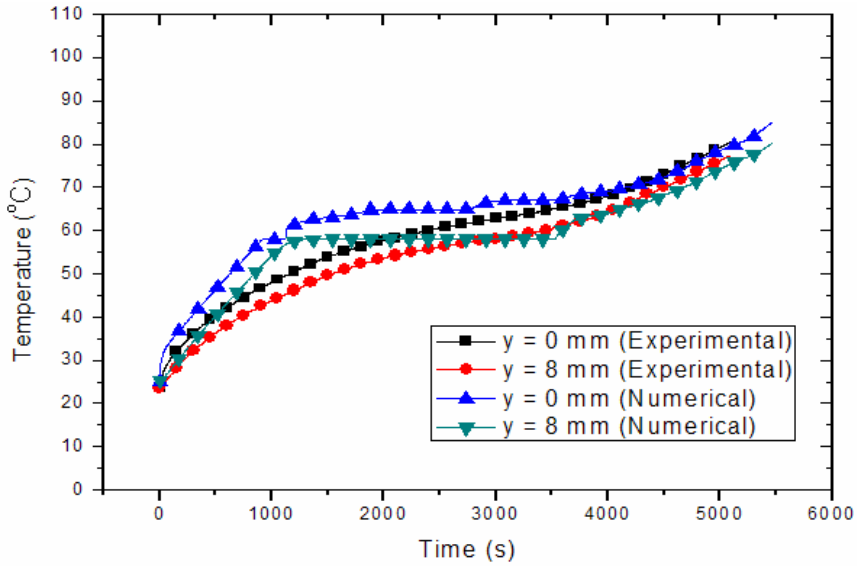

Figure 4.5. Comparison between numerical results and experimental data (two-dimensional coupled heat conduction and natural convection).

4.4.3 Flow field in natural convection

Figure 4.6 and Figure 4.7 present the velocity profiles at two different times (t = 1108 s and 5859 s, respectively), from which it can be clearly seen that two symmetrical eddies are formed when natural convection takes place. Both figures indicate that the PCM near the symmetrical plane (x = 0.1 m) tends to move upward, whilst the PCM on both the left and right sides has downward velocities. This is because the PCM can be regarded as being insulated on the symmetrical plane (at x = 0.1 m), but that it is losing heat to atmosphere on both sides. In Figure 4.6, only a small part of PCM has been melted and starts natural convection. As time goes on, more percentage of PCM is being melted. Figure 4.7 shows the velocity profile when the PCM is fully melted.

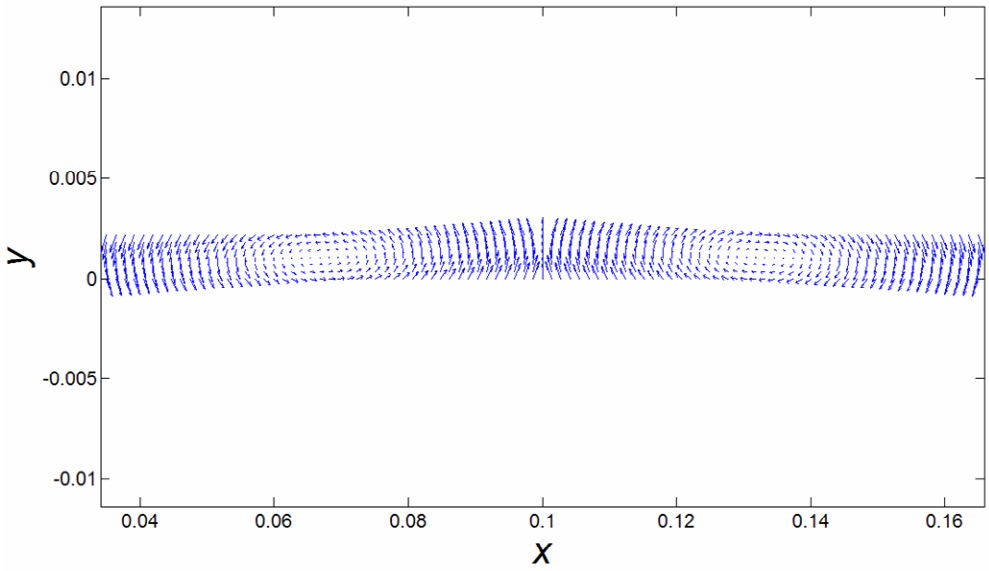

Figure 4.6. Velocity profile of natural convection (t = 1108 s).

From the numerical investigations, the velocities caused by buoyancy force are quite low, with an order of magnitude of 10^{-5} m/s. At first sight, this may seem rather surprising, but it is still believed to be reasonable, for the following reason. The buoyancy force term

$\rho_{PCM} g\beta\Delta T$, which drives natural convection, has an order of magnitude of 10^1, but in the main drag force term $-\mu_{PCM} u/K$ (i.e. Darcy term), μ_{PCM}/K has an order of magnitude of 10^6. According to the equilibrium of forces, drag force should have a similar order of magnitude to buoyancy force, and therefore u should have an order of magnitude of 10^{-5}. The paraffin wax RT58 used in this study has high dynamic viscosity of 0.0269 Pa·s (1000 times higher than air) and low thermal expansion coefficient of 1.1×10^{-4} K^{-1} (30 times lower than air), so these special physical characteristics result in the velocity driven by buoyancy force being so small in this case. Thus, the natural convection fails to produce dominant influence on heat transfer. It should be noted that despite the buoyancy-driven convection is not strong enough to have dominant influence, the weak natural convection over a long period of time can make a difference (slight heat transfer enhancement reflected by reduced melting time). The similar suppression of natural convection was also found by Stritih (2004), who added 32 metal fins into PCM to enhance heat transfer. However, he found that the addition of metal fins did not have the desired effects on heat transfer enhancement during melting, with the reason being that natural convection was significantly suppressed by the metal fins, so that the Rayleigh number in his study was not sufficiently high to overcome the large flow resistance.

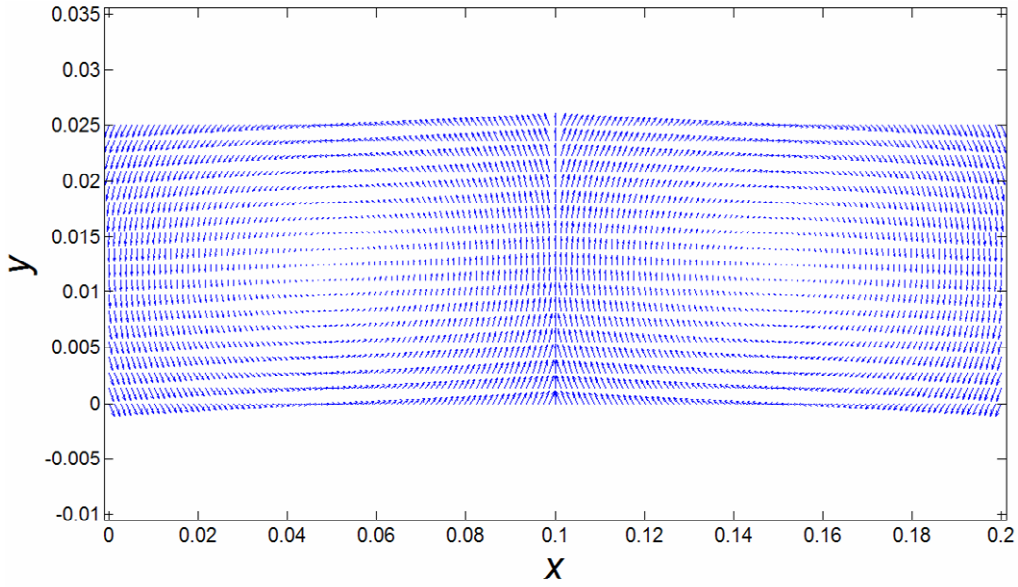

Figure 4.7. Velocity profile of natural convection (t = 5859 s).

To illustrate this further, an examination for smaller viscosity and larger thermal expansion coefficient was carried out. The viscosity and thermal expansion coefficient of "air" were adopted, which are 1.85×10^{-5} Pa·s and 3.43×10^{-3} K^{-1} respectively, but with other factors in the model remaining unchanged. It was found that the buoyancy-driven velocities became much larger than those in Figure 4.7, having an order of magnitude of 10^{-2} m/s (Tian and Zhao, 2010), and natural convection was strong enough to produce dominant influence on heat transfer. Figure 4.8 shows the effect of PCM viscosity on the relative thermal conductivity of the metal foam-PCM system when all other parameters remain the same. Relative themal conductivity reflects the degree of heat transfer enhancement by using metal foam, and is defined as U divided by the PCM thermal conductivity, which is 0.20 W/m K. U is defined by Eq. (4.28), representing the equivalent thermal conductivity of the metal foam-PCM system. The case numbers 1–8 represent the viscosity of μ_{PCM}, 0.1 μ_{PCM}, 0.01 μ_{PCM}, 0.001 μ_{PCM}, 0.0002 μ_{PCM}, 0.0001 μ_{PCM}, 0.00002 μ_{PCM} and 0.00001 μ_{PCM}, respectively. As seen in Figure 4.8, when

viscosity decreases, natural convection becomes stronger and it significantly enhances the heat transfer. Therefore from the heat transfer point of view, the PCM with low viscosity is preferred when choosing among several PCMs which have satisfied all other design requirements.

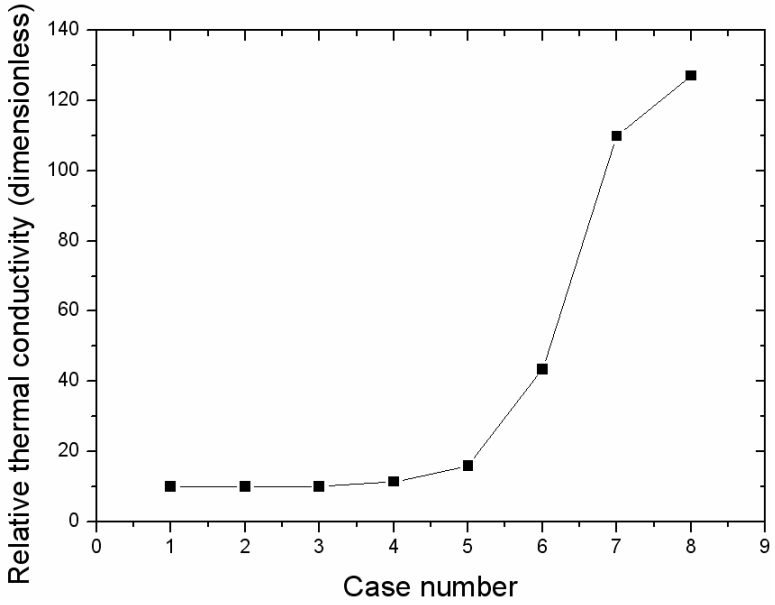

Figure 4.8. Effect of PCM viscosity on natural convection.

4.4.4 Effect of metal foam microstructures

For a thermal system with fixed heat flux, a smaller temperature difference means a higher heat transfer rate, which is reflected by Fourier's Law shown below:

$$U = q_w \frac{\Delta d}{\Delta T} \tag{4.28}$$

where U is the equivalent thermal conductivity of the metal foam-PCM thermal system; q_w is the heat flux; ΔT is the temperature difference; Δd is the distance for which the temperature difference is exerted.

Figure 4.9 shows a comparison of the temperature differences (between y = 8 mm and y = 0 mm) among three different metal-foam samples, each with either 95% or 85% porosity and with pore sizes of either 10 ppi or 30 ppi. The data in Figure 4.9 are from numerical simulations. It shows that after an initial rise, the temperature differences stay steady for a considerable time before melting starts. This is followed by a rapid drop at around t = 1100 s, due to the start of melting which enhances the heat transfer performance. As time increases and melting continues, temperature differences stay relatively constant for a considerable time. Once the PCM near the heating wall has finished absorbing the latent heat, the temperature differences rise rapidly. However, at this point, the PCM at y = 8 mm has not finished phase change and still keeps a constant temperature at 58 ºC. As time increases further, this part of PCM finishes the phase change process and consequently its temperatures rise dramatically around t = 3000 s, resulting in a decrease of temperature differences.

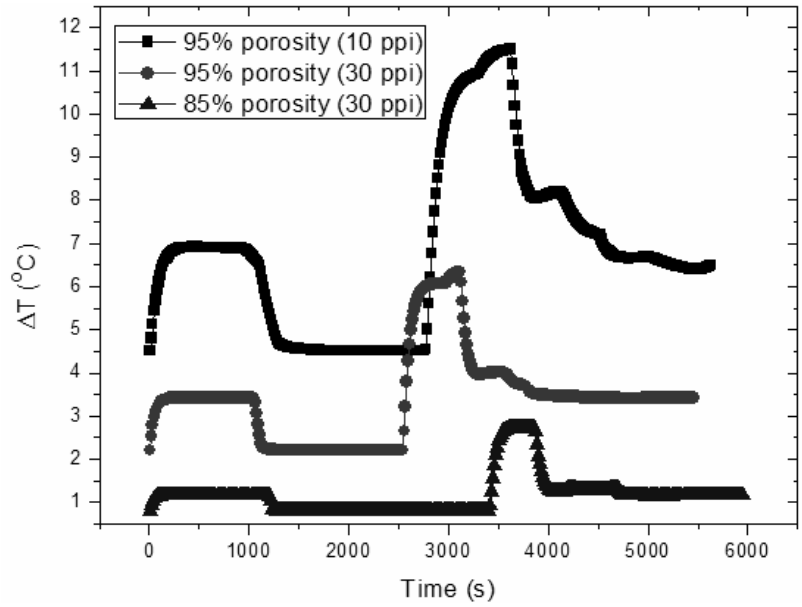

Figure 4.9. Comparison of temperature differences among three different metal-foam samples.

By using Eq. (4.28), the temperature differences in Figure 4.9 can be transformed into equivalent thermal conductivities *U*. Figure 4.10 shows *U* for three different metal-foam samples. It can be seen that two samples of 30 ppi have better heat transfer performance than the sample of 10 ppi. This is reasonable because smaller pore size (30 ppi) means larger contact area between the PCM and metal ligaments to transfer heat. Figure 4.10 also shows that the sample of 85% porosity achieves better heat transfer performance than that of 95% porosity. This is reasonable because the metal foam of lower porosity has more solid structures, which results in higher effective thermal conductivity; thus heat can be drawn more efficiently from the heating surface to the PCM through the metal foam structures.

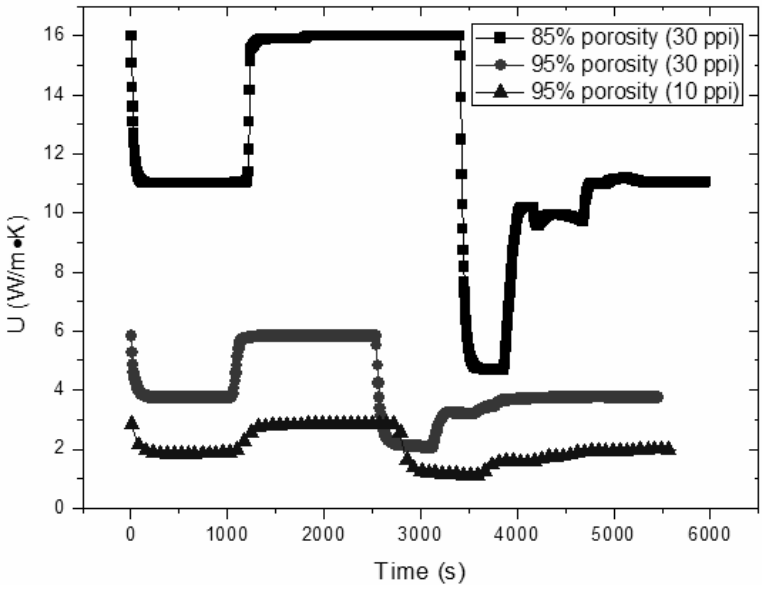

Figure 4.10. Comparison of equivalent thermal conductivities among three different metal-foam samples.

In summary, the metal-foam samples of smaller pore size and porosity can achieve better heat transfer performance than those of larger pore size and porosity.

4.4.5 PCM Temperature profiles during the phase change process

Figures 4.11(a)–(d) show the evolution of temperature profiles of the PCM for the metal-foam sample of 95% porosity and 10 ppi during melting process. Temperatures are represented by different colours in the figure, with numbers on the isotherms denoting the exact values (in ^{o}C).

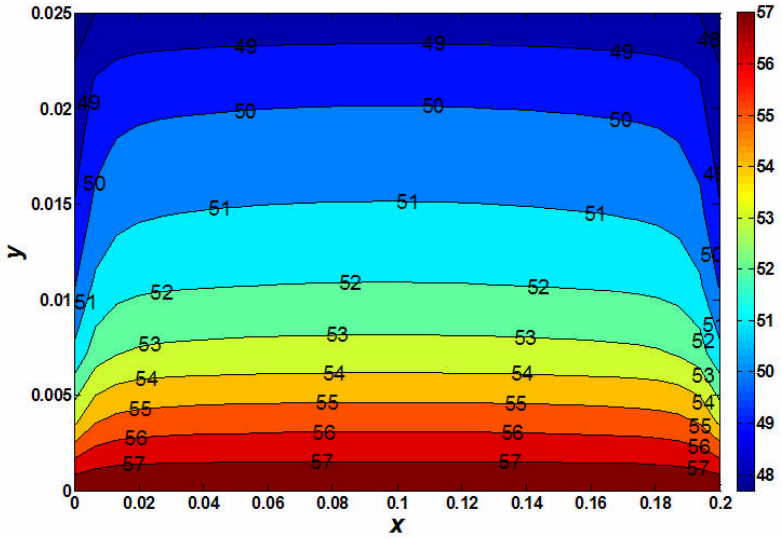

(a) t = 977 s

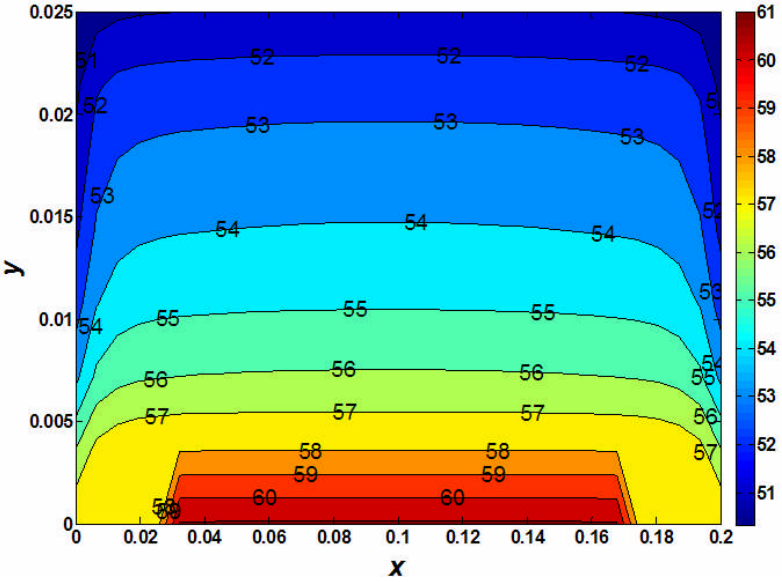

(b) t =1108 s

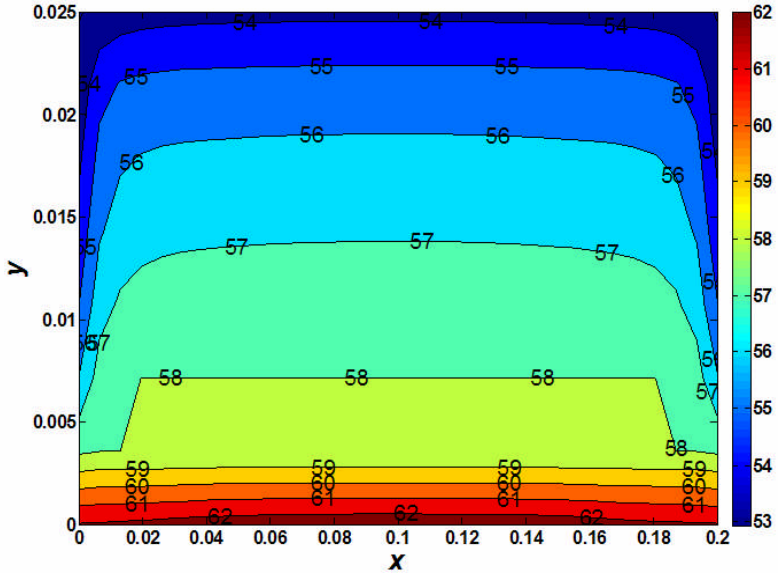

(c) t = 1318 s

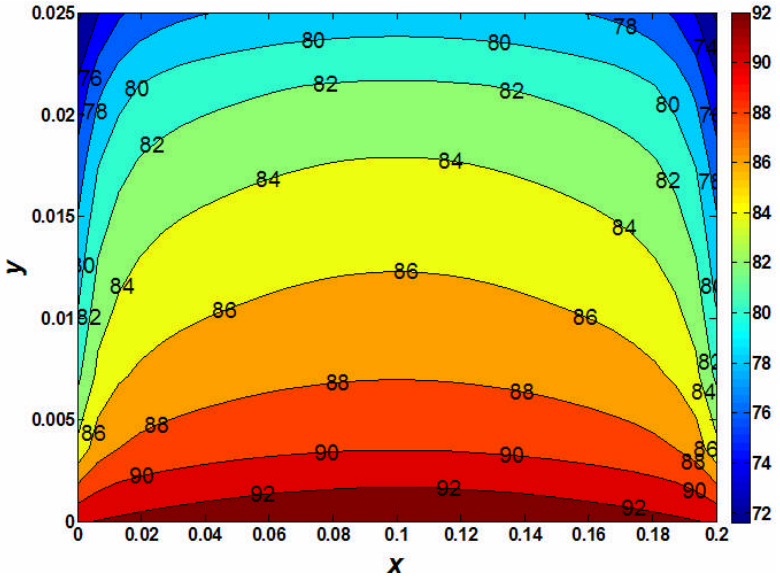

(d) t = 5859 s

Figure 4.11. Temperature profiles (two-dimensional heat conduction and natural convection).

Figure 4.11(a) shows its temperature profiles at t = 977 s. At this time, the maximum temperature of the PCM in the whole region is 57 ºC which is still below the melting point (58 ºC). When t = 1108 s, a small part of PCM near the bottom boundary has reached to 58 ºC and begun to melt gradually, illustrated by the isotherms shown in Figure 11(b). It can also be seen that the left and right parts of the PCM near the bottom side have not yet begun to melt, because the PCM at these places is losing heat to atmosphere through the left and right boundary and therefore has not acquired enough heat to reach the melting point.

As time increases, the melting front gradually moves upwards, meaning more PCM is being melted, as shown in Figure 11(c). The PCM temperature profiles when t = 5859 s are shown in Figure 11(d). At this time, all the PCM has been fully heated into liquid state, with the minimum and maximum temperatures being 72 ºC and 92 ºC.

4.5. Conclusion

The numerical results have shown good agreement with experimental data, even though the PCM (RT58) used in the experiments does not have a fixed melting point, as assumed in the model. When comparing the samples which have metal foams embedded into PCM with a pure PCM sample, it was found that the addition of metal foams can considerably enhance PCM heat transfer performance (overall, 3–10 times) through effectively transferring heat from the metal skeleton to the PCM.

It was found from the simulations that the velocity driven by the buoyancy force is not strong enough to produce dominant influence on heat transfer in the PCM. This is due to the high viscosity (about 1000 times higher than air) and low thermal expansion coefficient (30 times lower than air) of RT58, as well as the high flow resistance in metal foams. The simulation results also indicated that metal foams with smaller pore size and

porosity can achieve better heat transfer performance than those with larger pore size and porosity. In addition, a series of detailed evolutions of velocity and temperature distributions have been obtained; these illustrate clearly the phase change processes of the PCM.

Chapter 5. Cascaded Thermal Energy Storage

Apart from using metal foams, Cascaded Thermal Energy Storage (CTES) is another option to enhance heat transfer in Thermal Energy Storage (TES) systems. In this Chapter, a thermal and exergetic analysis of CTES is conducted, and comparison is also made between CTES and the traditional Single-stage Thermal Energy Storage (STES).

5.1. Introduction

In a Thermal Energy Storage (TES) system, the temperature differences undergo an unavoidable decrease during heat exchange process, which worsens heat transfer. To tackle this problem, a new concept of cascaded thermal storage has been proposed (Medrano et al., 2010; Mehling and Cabeza, 2008; Dincer and Rosen, 2010). A cascaded thermal storage system consists of multiple Phase Change Materials (PCMs) with staged melting temperatures, so that a relatively constant temperature difference can be maintained to achieve higher heat transfer rate during the charging/discharging process. The concept of cascaded thermal storage was tested by Michelsa and Pitz-Paal (2007) for high-temperature molten salt storage system, and their results indicated that a cascaded arrangement of PCMs increased the charging/discharging rate. Watanabe et al. (1993) also identified a significant heat transfer enhancement in their 'three-type' storage system.

However, most previous studies on cascaded storage have focused on heat transfer rate, and therefore failed to reflect an important energy conversion factor – exergy. Exergy is the useful part of thermal energy in PCMs which can be converted into electricity. Krane (1987) employed the ε–NTU (Effectiveness–Number of Transfer Units) analysis to conduct an exergy study of a TES system, but only sensible heat was considered. It is necessary to make an overall thermal performance analysis of a TES system, considering not only sensible heat but also latent heat. In this Chapter, the overall thermal

performance of a cascaded thermal storage system is investigated, considering both heat transfer performance and exergy efficiency.

5.2. Problem description

For comparison, two systems will be presented: the Cascaded Thermal Energy Storage (CTES) and the Single-stage Thermal Energy Storage (STES). Figure 5.1(a) illustrates the CTES system, and Figure 5.1(b) illustrates the STES system. The CTES system was formed by staging three PCMs (different physical properties) along the flow direction of HTF (heat transfer fluid), whilst the STES system was formed by using only one PCM.

In Figure 5.1, H_L (kJ/kg) and T_m (ºC) denote the latent heat and the melting temperature respectively; h and L show the dimensions of the two systems. Heat transfer fluid (HTF) enters each system from the left (inlet temperature $T_{0.HTF}$ = 100 ºC), and exits each system from the right (temperature $T_{HTF}(t)$, varying with time). The thermal properties of the PCMs used in this study are shown in Table 5.1. The melting point of PCM 4 in STES was chosen to be approximately the average melting point of the three PCMs used in the CTES, and thus a comparison made between two systems is justifiable. The ambient temperature T_0 was 20 ºC, and the initial temperatures of the two systems were also 20 ºC. It should be noted that the actual arrangement of PCMs in the current study was different from what would be expected, in which the melting temperatures of PCMs usually decrease along the HTF flow direction. Therefore, further studies are required to examine other influencing factors, such as PCM permutations, PCM thermal properties (melting temperatures/latent heat) and HTF flow rates. In this study, exergy analysis was conducted for only PCM, having neglected the exergy of HTF, which should also be considered in future studies.

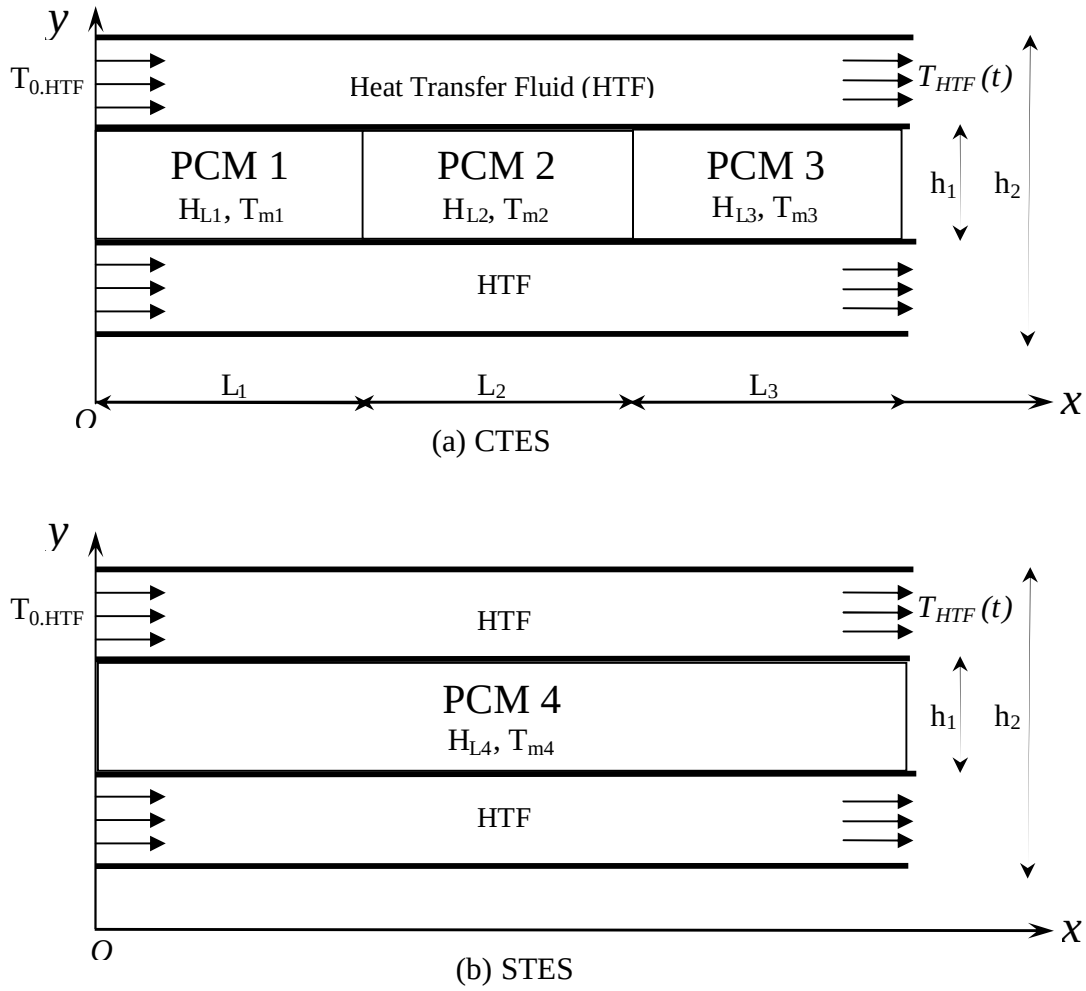

Figure 5.1. An illustration of CTES and STES processes.

Table 5.1. Thermal properties of PCMs.
(Rubitherm® Technologies GmbH, Germany, <http://www.rubitherm.de>)

PCMs	PCM 1	PCM 2	PCM 3	PCM4
Product code	RT31	RT50	RT82	RT55
Melting temperature (°C)	31	50	82	55
Density (kg/m^3)	880.0	880.0	880.0	880.0
Latent heat(kJ/kg)	169.0	168.0	176.0	172
Specific heat (kJ/kg °C)	2.1	2.1	2.1	2.1
Thermal conductivity (W/m K)	0.2	0.2	0.2	0.2
Linear thermal expansion coefficient (K^{-1})	1.1×10^{-4}	1.1×10^{-4}	1.1×10^{-4}	1.1×10^{-4}
Kinetic viscosity (mm^2/s)	28.57	31.20	45.45	34.08
Dynamic viscosity (Pa·s)	0.0251	0.0275	0.0400	0.0300

5.3. Mathematical description

5.3.1. Exergy analysis

The entropy change (Dincer and Rosen, 2010) of a thermal system from state '1' to state '2' can be written as:

$$s_2 - s_1 = c_p \ln(T_2 / T_1) - R_g \ln(p_2 / p_1) + H_L / T_m \tag{5.1}$$

The unusable part of the thermal energy (i.e. Anergy *X*), depends on the irreversible entropy increase, which is shown in Eq. (5.2).

$$X = T_0 (s_2 - s_1) = T_0 \left[c_p \ln(T_2 / T_1) - R_g \ln(p_2 / p_1) + H_L / T_m \right] \tag{5.2}$$

Thus the percentage of the usable energy can be calculated by using Eq. (5.3):

$$\eta_{ex} = \frac{c_p (T_2 - T_1) - X}{c_p (T_2 - T_1)} \times 100\% \tag{5.3}$$

Substituting Eq.(5.2) into Eq. (5.3), exergy efficiency is given in Eq. (5.4):

$$\eta_{ex} = \frac{c_p\left(T_2 - T_1\right) - T_0\left[c_p \ln(T_2/T_1) - R_g \ln(P_2/P_1) + H_L/T_m\right]}{c_p\left(T_2 - T_1\right)} \times 100\% \tag{5.4}$$

Eq. (5.4) can be reduced to Eq. (5.5), since most PCMs are incompressible.

$$\eta_{ex} = \frac{c_p\left(T_2 - T_1\right) - c_p T_0 \ln(T_2/T_1) - T_0 H_L/T_m}{c_p\left(T_2 - T_1\right)} \times 100\% \tag{5.5}$$

In this study, Eq. (5.5) has been used to obtain the exergy efficiency for both CTES and STES.

5.3.2. Heat transfer analysis on the HTF side

Considering the charging process of both CTES and STES, heat transfer comes from the high-temperature HTF to the low-temperature PCMs. Thermal resistance of heat transfer comprises the HTF-side resistance and the PCM-side resistance. The effective heat transfer coefficient on the HTF side can be obtained by simply employing the Dittus–Boelter Equation (Holman, 1997).

$$Nu = 0.023\,\mathrm{Re}^{0.8}\,\mathrm{Pr}^{0.4} \tag{5.6}$$

In this study, water was used as HTF: $v = 0.553\times10^{-6}$ m^2/s (kinetic viscosity at 50 ºC), Pr = 3.56 (Prandtl number at 50 ºC) (Vargaftik, 1975), characteristic length d = (h_2-h_1)/2 = 0.01 m. The HTF flow velocity is u = 0.5 m/s. By employing the Dittus–Boelter Equation shown in Eq. (5.6), the effective heat transfer coefficient h_{HTF} was calculated as 1117.7W/m^2 ($h_{HTF} = 0.023\lambda\mathrm{Re}^{0.8}\mathrm{Pr}^{0.4}$/d).

Biot number was then obtained by:

$$Bi = \frac{h_{HTF}\,\mathrm{d}}{k_{PCM}} = 55.9 >> 1 \tag{5.7}$$

Biot number (Holman, 1997) roughly represents how many times bigger the thermal resistance on the PCM side is than that on the HTF side. Since it is much greater than 1,

the thermal resistance on the HTF can be reasonably neglected, which simplifies the following analyses.

5.3.3. Heat transfer analysis

Perfect thermal insulation was assumed in the study, so the heat transfer equations can be established by employing the Energy Conservation Law: PCMs absorb the same amount of thermal energy as HTF releases. This is reflected in Eq. (5.8).

$$-dq_{HTF} = dq_{PCM} = h_{exch}(T_{HTF} - T_{PCM})dA \tag{5.8}$$

dq_{HTF} and dq_{PCM} in Eq. (5.8) can be written as follows:

$$dq_{HTF} = c_{HTF}\dot{m}_{HTF}\frac{\partial T_{HTF}}{\partial x}\frac{\partial x}{\partial t} \tag{5.9}$$

$$dq_{PCM} = \rho_{PCM}\mathrm{h}_1 dA\frac{\partial H_{PCM}}{\partial t} \tag{5.10}$$

The factor $\frac{\partial x}{\partial t}$ on the right hand side of Eq. (5.9) is equal to the flow velocity of HTF, given by:

$$\frac{\partial x}{\partial t} = u_{HTF} \tag{5.11}$$

Thus Eq. (5.8) can be rewritten as Eq. (5.12).

$$-c_{HTF}\dot{m}_{HTF}\frac{\partial T_{HTF}}{\partial x}u_{HTF} = \rho_{PCM}\mathrm{h}_1 dA\frac{\partial H_{PCM}}{\partial t} = h_{exch}(T_{HTF} - T_{PCM})dA \tag{5.12}$$

To tackle the phase change problem, the Enthalpy Method (Tian and Zhao, 2010) has been employed. The PCM enthalpy H_{PCM} shown in Eq. (5.10) has the following relationship with the PCM temperature T_{PCM} (Tian et al., 2012).

$$T_{PCM}=\begin{cases}\dfrac{H_{PCM}}{c_{PCM}}, & H_{PCM}\in(-\infty,c_{PCM}T_m)\\ T_m, & H_{PCM}\in\left(c_{PCM}T_m,c_{PCM}T_m+H_L\right)\\ \dfrac{H_{PCM}-H_L}{c_{PCM}}, & H_{PCM}\in(c_{PCM}T_m+H_L,+\infty)\end{cases}\qquad(5.13)$$

5.4. Numerical procedure

Eq. (5.12) and (5.13) are the equations governing such particular heat transfer phenomena. These equations were solved simultaneously by the Finite Difference Method (FDM) in Matlab®. 3,000 uniform meshes were used in the *x*-direction to ensure the simulation accuracy. Mesh independency was also examined, and it was found that 6,000 meshes could only improve the accuracy by 0.10% compared to the case of 3,000 meshes. The Implicit Iteration was adopted as the Difference Scheme, because the simulation indicated that Explicit Iteration made the results divergent whilst Implicit Iteration made the results convergent and accurate. Numerical simulations were set to stop when the error between two consecutive iterations was less than 10^{-6} (i.e. 0.0001%).

5.5. Results and discussion

Figure 5.2(a) shows the comparison of heat transfer rates between the CTES and STES system. It indicates that the cascaded arrangement of PCMs (CTES) enhanced heat transfer rate by up to 30% (overall). However, it should be noted that CTES showed lower heat transfer rate than STES after PCM 2 finished the melting process (when the dimensionless time in Figure 5.2(a) is around 2). The dimensionless time was defined as the real time divided by a reference time that equals the melting time of PCM 2. The low heat transfer rate of CTES can be attributed to two reasons: firstly, the temperatures in the CTES system increased rapidly (sensible heat only) when PCM 2 (50 ºC) finished phase change; secondly, at the same time when the temperatures in the CTES system rose

rapidly, the temperatures in the STES system kept relatively constant because PCM 4 (55 ºC) is still in the melting process (latent heat). The rapidly rising temperatures caused the decrease of temperature differences between PCMs and HTF, resulting in a lower heat transfer rate.

The phase change regions of PCM 1, PCM 2, PCM 3 and PCM 4 can also be seen in Figure 5.2(a). In the CTES system, PCM 3 used the most time to finish phase change whilst PCM 1 used the least time to finish phase change. The reason is that the temperature differences between these PCMs and HTF decreased along the HTF flow direction shown in Figure 5.1, which resulted in the decrease of heat transfer rate and the prolongation of the melting time.

To make a clear comparison between the two systems, Figure. 5.2(b) has been drawn to show the relative heat exchange rate of CTES, which was defined as $(q_{CTES} - q_{STES})/ q_{STES.}$ The figure shows that CTES nearly always had higher heat exchange rate than STES (up to 45%; overall, around 30%). The two reasons why CTES had slightly lower heat exchange rate than STES around dimensionless time = 2 was given in the first paragraph of this Section.

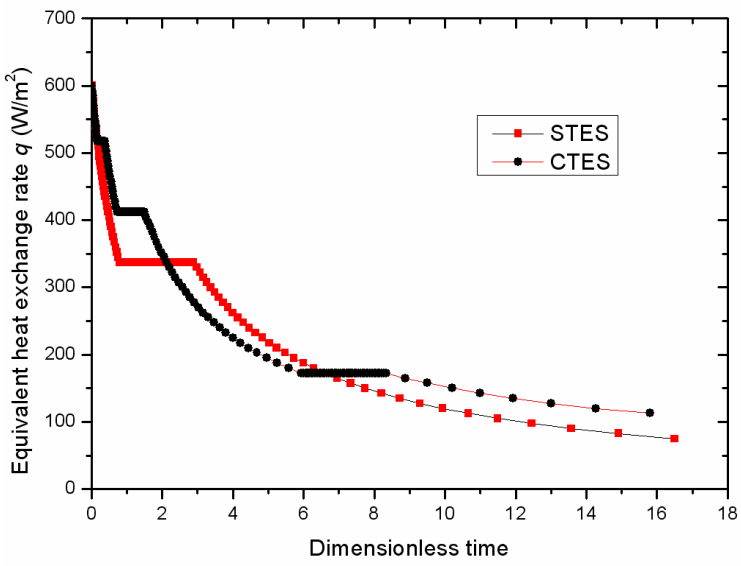

(a)

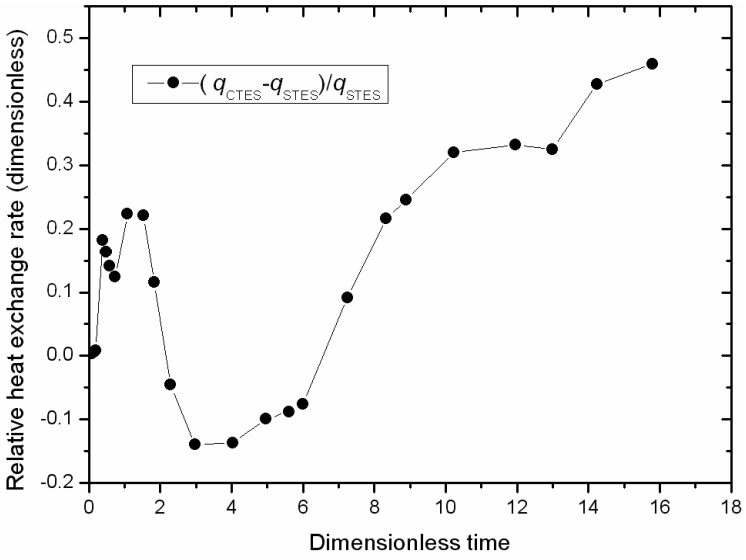

(b)

Figure 5.2. Comparison of equivalent heat exchange rate between CTES and STES.
(a) Equivalent heat exchange rate q (W/m^2);
(b) Relative heat exchange rate (dimensionless).

Exergy efficiency of the two systems is given in Figure 5.3(a), with the comparison between them shown in Figure 5.3(b). The relative exergy efficiency in Figure 5.3(b) has been defined as $(\eta_{ex\_CTES} - \eta_{ex\_STES})/\eta_{ex\_STES}$, with η_{ex_CTES} denoting the exergy efficiency of CTES and η_{ex_STES} denoting the exergy efficiency of STES. The CTES system does not always have higher exergy efficiency than the STES system (-20% to +30%). The exergy efficiency of CTES was lower than that of STES in early stages before PCM 4 started to melt, because PCM 1 and PCM 2 in CTES delayed the increase of temperature rise due to their latent heat. Since lower temperatures mean lower quality of energy, the CTES system had lower exergy efficiency at this time. However, the situation was changed when PCM 2 finished phase change and PCM 4 started phase change. From this time on, the temperatures in CTES began to increase rapidly (sensible heat) whilst the temperatures in STES kept relatively constant (latent heat), which led to CTES having a higher exergy efficiency than STES.

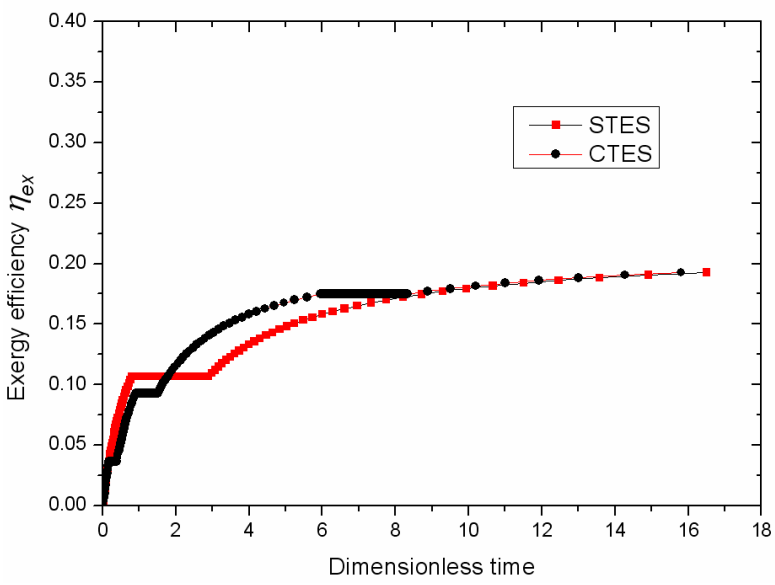

(a) Exergy efficiency η_{ex} (%);

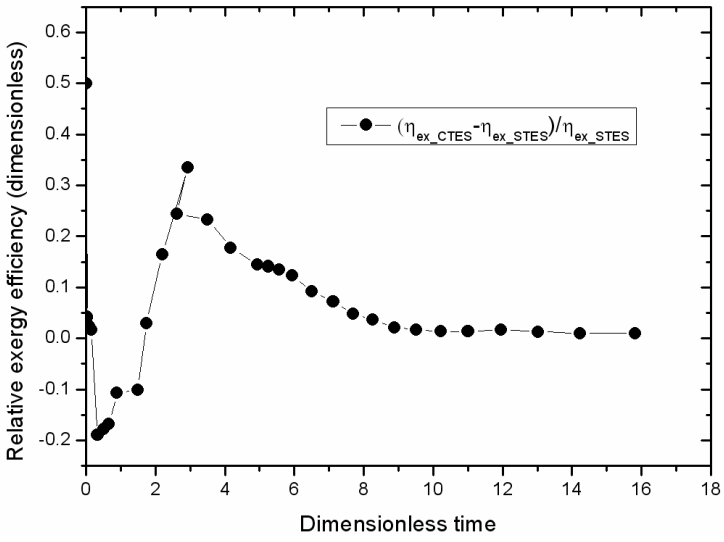

(b) Relative exercy efficiency (dimensionless).

Figure 5.3. Comparison of exergy efficency between CTES and STES.

As stated in the Second Law of Thermodynamics (Carnot et al., 1899), no thermal system can have 100% thermal efficiency in the process of converting heat to work. As a consequence, heat transfer rate q in Figure 5.2 cannot reflect the real thermal efficiency of an energy storage system. Thus, a concept of exergy transfer rate h_{ex} was proposed in this study to evaluate the overall thermal performance of the CTES and STES systems (Tian et al., 2012).

$$h_{ex} = q \times \eta_{ex} \ (\mathrm{W/m^2}) \tag{5.14}$$

where h_{ex} denotes the effective exergy transfer rate, representing the amount of useful thermal energy transferred from HTF to PCMs during charging processes. Figure 5.4(a) gives the values of the effective exergy transfer rates (h_{ex}) of both CTES and STES, with the comparison between them shown in Figure 5.4(b). The relative exergy transfer rate in Figure 5.4(b) was defined as $(h_{ex\_CTES} - h_{ex\_STES})/ h_{ex\_STES}$. It can be concluded that CTES nearly always produced higher exergy transfer rate (up to 22%) than STES. It should be noted that CTES showed slightly lower exergy transfer rate than STES, only when PCM 1 started phase change and when PCM 4 finished phase change. There are two probable reasons for this: Firstly, when PCM 1 started its phase change, CTES had lower exergy efficiency than STES although the former had slightly higher heat transfer rate than the latter. Secondly, after PCM 4 finished its phase change, the heat transfer rate of STES was higher than CTES due to the long-time delay of temperature rise (latent heat of PCM 4), but the exergy efficiency of STES was much lower than CTES (shown in Figure 5.3) due to its low temperatures after phase change.

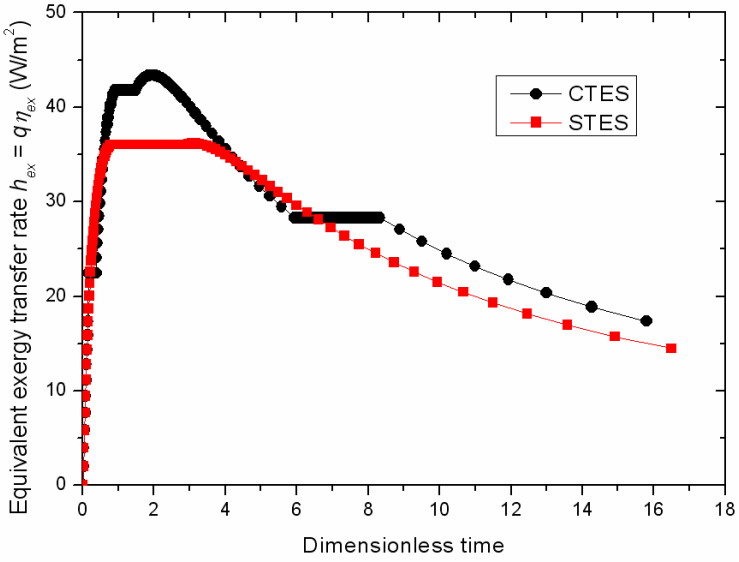

(a) Equivalent exergy transfer rate h_{ex} (W/m^2)

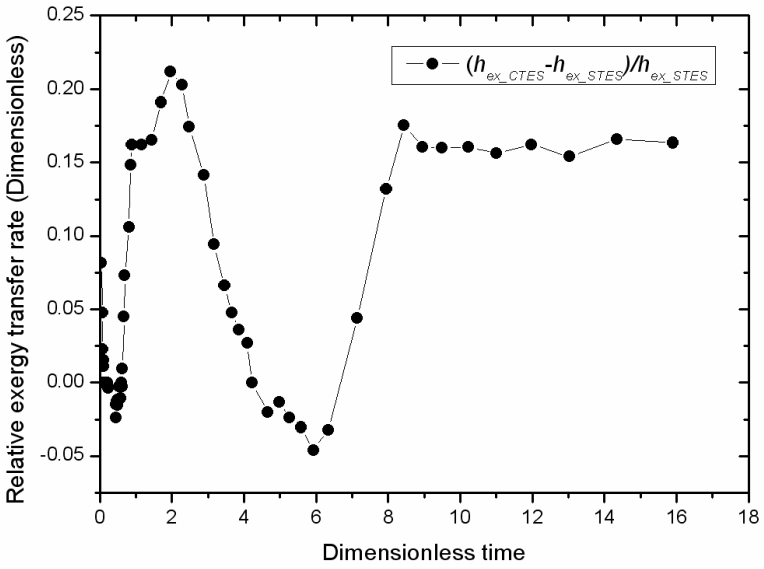

(b) Relative exergy transfer rate (dimensionless)

Figure 5.4. Comparison of equivalent exergy transfer rate between CTES and STES.

5.6. Conclusion

A comparative study for CTES and STES has been carried out. In order to take energy conversion efficiency into account, effective exergy transfer rate was introduced to evaluate a thermal energy storage system. The main finding is that although CTES can show lower exergy efficiency (-20% to 30%) than STES, CTES has a much higher heat transfer performance (overall 30%) than STES, making the overall thermal performance of CTES still superior (up to 22%) to that of STES.

5.7. Limitations

This work has neglected heat conduction of the PCMs in vertical direction (the *y*-direction), and natural convection was not considered. It is necessary to conduct a further work that incorporates a multi-dimensional numerical simulation on the coupled natural convection and heat conduction in both vertical and horizontal directions, which is given in Chapter 6.

Chapter 6. Metal Foam-enhanced Cascaded Thermal Energy Storage

Metal foams and Cascaded Thermal Energy Storage (CTES) have been investigated for their heat transfer enhancement in Thermal Energy Storage (TES) systems, with metal foams examined in Chapters 3 and 4, and CTES in Chapter 5. In Chapter 6, the idea of combining metal foams and CTES is examined by conducting a thermal and exergetic analysis of Metal Foam-enhanced Cascaded Thermal Energy Storage (MF-CTES).

6.1. Introduction

Low heat transfer performance has been the main limitation restricting the application of Phase Change Materials (PCMs) in situations requiring rapid energy release/storage. Apart from using high-thermal conductivity materials with porous structures, Cascaded Thermal Energy Storage (CTES) is another method to enhanced heat transfer for PCM applications (Watanabe et al., 1993; Tian et al., 2012). CTES, consisting of multiple PCMs with cascaded melting temperatures, has been proposed as a solution to heat transfer deterioration, which often arises when charging/discharging a single-stage PCM storage system. For a single-stage PCM storage system, the temperature of the heat transfer fluid falls rapidly when transferring heat to the PCM; as a result, the temperature difference between heat transfer fluid and the PCM is significantly reduced, which leads to poor heat transfer at the end of the storage (Mehling and Cabeza, 2008). The problem is that the PCM is melted rapidly at the entrance part, but much more slowly at the end of the storage. A similar problem occurs for the discharging process: the PCM at the end of the storage might not be used as the temperature of heat transfer fluid rises. Such problems can be solved by adopting CTES, in which the PCMs with cascaded melting temperatures can help to maintain a relatively high temperature difference.

Gong and Mujumdar (1997) investigated a five-stage PCMs system, and found a significantly improved heat transfer (34.7%) compared to the single PCM. Michels and Pitz-Paal (2007) investigated a three-stage PCM system, and found that a higher proportion of PCMs melted and a more uniform heat transfer fluid outlet temperature than in the traditional single-stage storage. The study by Michels and Pitz-Paal (2007) was based on energy efficiency, not having considered exergy efficiency that represents the utilisable part of energy. Exergy analyses for multiple PCM systems were conducted by Watanabe and Kanzawa (1995), and Shabgard et al. (2012). Watanabe and Kanzawa (1995) found increased exergy efficiency by using multiple PCMs, whilst Shabgard et al. (2012) found that the multiple PCMs recovered more amount of exergy despite having lower exergy efficiency at times. A thermal analysis taking exergy into account does not only consider the quantity of energy, but also the quality of energy, and therefore is very important. However, there are only a few publications addressing exergy issues for CTES; none of these studies has combined CTES with other heat transfer enhancement techniques, especially the use of metal foams.

In this Chapter, the idea of the Metal Foam-enhanced CTES system is investigated, with its technical feasibility being examined and energy/exergy performance being evaluated.

6.2. Physical problem

Metal Foam-enhanced Cascaded Thermal Energy Storage (MF-CTES) is illustrated in Figure 6.1(a). For comparison, CTES is also given in Figure 6.1(b). Both MF-CTES and CTES are formed by staging three PCMs along the HTF (heat transfer fluid) flow direction: PCM 1, 2 and 3 shown in Figure 6.1. MF-CTES and CTES are made of the same PCMs, with the only difference being that MF-CTES uses metal foam to enhance heat transfer. The thermo-physical properties of these PCMs used are listed in Table 5.1.

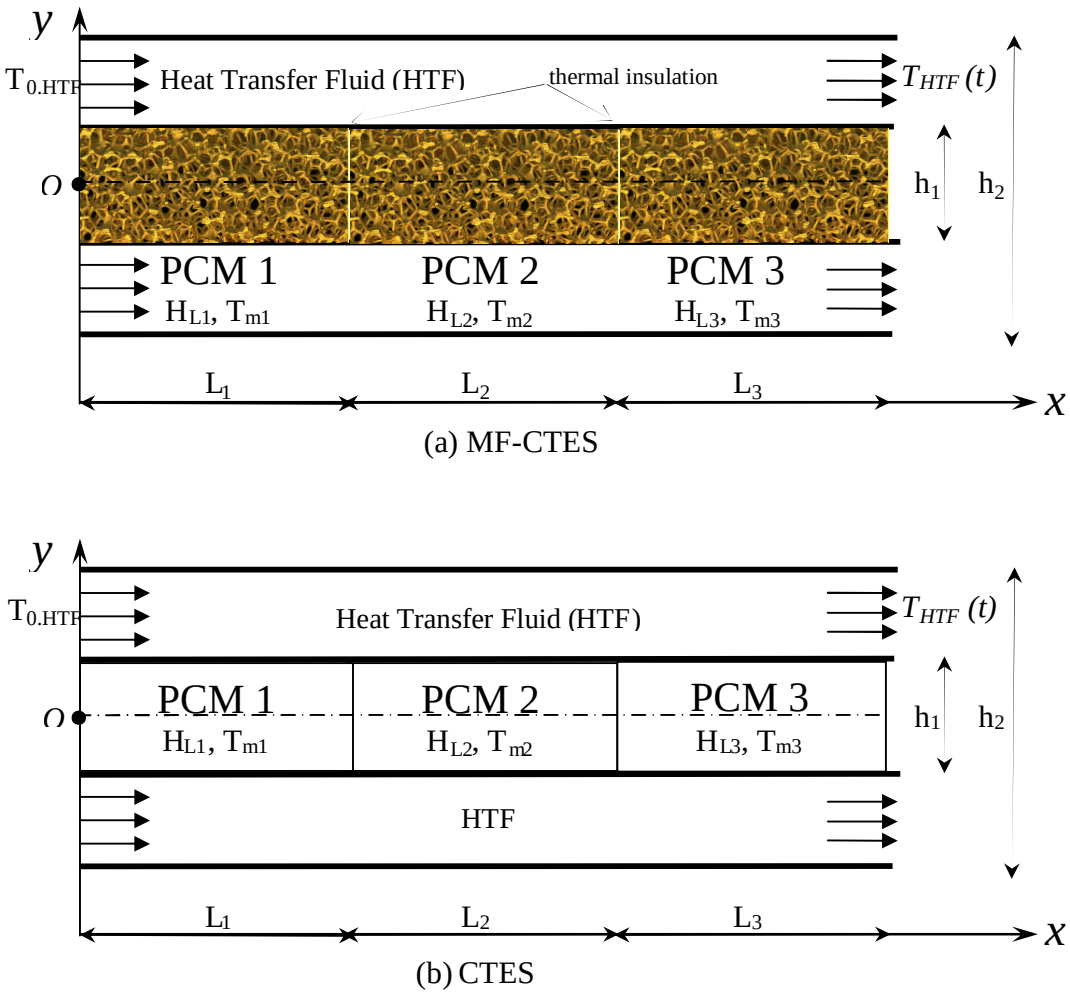

Figure 6.1. An illustration of the MF-CTES and CTES processes.

In Figure 6.1, H_L (kJ/kg) and T_m (ºC) denote the latent heat and melting temperature, respectively; h and L denote system dimensions. The HTF enters each system from the left (inlet temperature $T_{0.HTF}$ = 100 ºC), and exits from the right with the outlet temperature $T_{HTF}(t)$ which varies with time. The initial temperatures of both systems are equal to the ambient temperature, which is 20 ºC. Other parameters for the systems are given in Table 6.1.

Table 6.1. System parameters in the current study.

HTF properties		System dimension	
Density: ρ	1000 kg/m^3	L_1	3.5 m
Velocity: u	0.5 m/s	L_2	3.5 m
Dynamic viscosity at 50 ºC: υ	0.553×10^{-6} m^2/s *	L_3	3.5 m
Prandtl number at 50 ºC: Pr	3.56 *	h_1	0.02 m
Specific heat: c_p	4.2 kJ/(kg ºC) *	h_2	0.04 m
Thermal conductivity: λ_{HTF}	0.6 W/(m K) *	Characteristic diameter	
		$d = (h_2–h_1)/2$	0.01 m
Inlet temperature: $T_{0.HTF}$	100 ºC		
Ambient temperature: T_a	20 ºC		

*: Dincer and Rosen (2010).

6.3. Mathematical description

6.3.1. Exergy efficiency

Chapter 6 uses the same routine as given in Chapter 5 to obtain the exergy efficiency η_{ex} for the MF-CTES system, shown in Eq. (6.1). Details of its derivation were given by Eqs. (5.1) to (5.5) in Chapter 5.

$$\eta_{ex} = \frac{c_p\left(T_2 - T_1\right) - c_p T_a \ln(T_2/T_1) - T_a H_L/T_m}{c_p\left(T_2 - T_1\right)} \times 100\% \tag{6.1}$$

6.3.2. Heat transfer on the HTF side

Considering an energy charging process, heat flows from the high-temperature heat transfer fluid (HTF) to low-temperature PCMs. The thermal resistance of heat transfer is made up of the HTF-side resistance and PCM-side resistance. As discussed in Chapter 5, the *Bi* number (Biot number) qualitatively represents how many times larger the thermal

resistance is on the PCMs side than on the HTF side. Using the same method employed in Section 5.3.2, the *Bi* number (Biot number) in this case was estimated to 55.9, which is much greater than 1. With *Bi* much greater than 1, the thermal resistance on the HTF side can be reasonably neglected, and this highly simplifies the following analyses. It should be noted that the obtained *Bi* number is an approximate value, because this study used rectangular ducts, rather than round ducts which were assumed in the Dittus-Boelter Equation. Even allowing for this, the *Bi* number will still be much greater than 1, so that the thermal resistance on the HTF side is so low that it can be neglected.

6.3.3. Heat transfer between HTF and PCM-metal foam.

Perfect thermal insulation was assumed in this study, so the heat transfer equations can be established based on the energy conservation law: PCMs absorb the same amount of thermal energy as the HTF releases, which is reflected in Eq. (6.2) (Tian and Zhao, 2012b).

$$\begin{aligned}\rho_{HTF} c_{p.HTF} (\mathrm{h}_2\text{-}\mathrm{h}_1) dA \frac{\partial T_{HTF}}{\partial x} \frac{\partial x}{\partial t} &= \rho_{PCM-MF} \mathrm{h}_1 dA \frac{\partial H_{PCM-MF}}{\partial t} \\ &= \mathrm{h}_1 dA \left[\varepsilon \rho_{PCM} \frac{\partial H_{PCM}}{\partial t} + \rho_{MF} c_{p.MF} (1-\varepsilon) \frac{\partial T_{MF}}{\partial t} \right]\end{aligned} \tag{6.2}$$

Due to $\frac{\partial x}{\partial t} = u_{HTF}$, Eq. (6.2) can be rewritten as:

$$\rho_{HTF} c_{p.HTF} (\mathrm{h}_2\text{-}\mathrm{h}_1) u_{HTF} \frac{\partial T_{HTF}}{\partial x} = \mathrm{h}_1 \left[\varepsilon \rho_{PCM} \frac{\partial H_{PCM}}{\partial t} + \rho_{MF} c_{p.MF} (1-\varepsilon) \frac{\partial T_{MF}}{\partial t} \right] \tag{6.3}$$

In order to cope with the phase change heat transfer problem, the enthalpy method has been employed in this study. The correlation between the PCM enthalpy function $H_{PCM}(x, y, t)$ and its temperature function $T_{PCM}(x, y, t)$ is given by:

$$T_{PCM}=\begin{cases}\dfrac{H_{PCM}}{c_{PCM}}, & H_{PCM}\in(-\infty,c_{PCM}T_m)\\ T_m, & H_{PCM}\in\left(c_{PCM}T_m,c_{PCM}T_m+H_L\right)\\ \dfrac{H_{PCM}-H_L}{c_{PCM}}, & H_{PCM}\in(c_{PCM}T_m+H_L,+\infty)\end{cases} \tag{6.4}$$

6.3.4. Heat transfer on the PCM-metal foam side

In this Section, the governing equations for heat transfer on the PCM-metal foam side, including fluid dynamics equations, phase change heat transfer equations and their initial and boundary conditions will be formulated.

The process of solving complicated equations by numerical methods can be significantly simplified if the physical problem is symmetrical. A symmetrical physical problem requires that the computational domain, the initial and boundary conditions, and the governing equations should all be symmetrical. The computational domain for the present study is: $0<x<\mathrm{L}_1+\mathrm{L}_2+\mathrm{L}_3$ and $-\mathrm{h}_1/2<y<+\mathrm{h}_1/2$ (shown in Figure 6.1). Such a rectangular domain is symmetrical with respect to the *x*-axis. The initial and boundary conditions are discussed later in Section 6.3.4.3, which indicates that the upper part (above the *x*-axis) has identical initial and boundary conditions to the lower part (below the *x*-axis), meaning that the initial and boundary conditions are also symmetrical upon the *x*-axis. However, the present study takes natural convection into account, in which the gravity and temperature difference-driven buoyancy are not symmetrical, so the fluid dynamics equation in the *y*-direction is not symmetrical with respect to the *x*-axis. Hence the current physical problem will have to be solved on the whole computational domain.

6.3.4.1. Equations of fluid dynamics

When natural convection takes place, the metal foam remains stationary, whilst the PCM keeps moving under a buoyancy force driven by temperature difference. To tackle such complicated PCM flow in the porous metal foam, a volume-averaging technique has been employed (Calmidi, 1998; Calmidi and Mahajan, 2000; Tian and Zhao, 2011a), for which the classical Continuity Equation is:

$$\nabla \bullet \langle \mathbf{V} \rangle = \mathbf{0} \tag{6.5}$$

where $\langle\ \rangle$ denotes the volume-averaged value of a certain function over an REV (Representative Elementary Volume inside metal foams). The definition of REV was given in Section 4.2.

The Continuity Equation takes on the following form within Cartesian coordinate system:

$$\frac{\partial u_{PCM}}{\partial x} + \frac{\partial v_{PCM}}{\partial y} = 0 \tag{6.6}$$

where u_{PCM} and v_{PCM} denote the components of the velocity **V** in the *x*-direction and the *y*-direction respectively.

Based on the Brinkman-Forchheimer extended Darcy model (Calmidi, 1998), the Momentum Equations are given by:

$$\begin{aligned} &\rho_{PCM}\frac{\partial u_{PCM}}{\partial t} + \frac{\rho_{PCM}}{\varepsilon}\left(u_{PCM}\frac{\partial u_{PCM}}{\partial x} + v_{PCM}\frac{\partial u_{PCM}}{\partial y}\right) = -\frac{\partial p}{\partial x} + \\ &\frac{\mu_{PCM}}{\varepsilon}\left(\frac{\partial^2 u_{PCM}}{\partial x^2} + \frac{\partial^2 u_{PCM}}{\partial y^2}\right) - \frac{\mu_{PCM}}{K}u_{PCM} - \frac{\rho_{PCM}C_f}{\sqrt{K}}|u_{PCM}|u_{PCM} \end{aligned} \tag{6.7}$$

$$\rho_{PCM}\frac{\partial v_{PCM}}{\partial t}+\frac{\rho_{PCM}}{\varepsilon}\left(u_{PCM}\frac{\partial v_{PCM}}{\partial x}+v_{PCM}\frac{\partial v_{PCM}}{\partial y}\right)=-\frac{\partial p}{\partial y}+$$
$$\frac{\mu_{PCM}}{\varepsilon}\left(\frac{\partial^2 v_{PCM}}{\partial x^2}+\frac{\partial^2 v_{PCM}}{\partial y^2}\right)-\frac{\mu_{PCM}}{K}v_{PCM}-\frac{\rho_{PCM}C_f}{\sqrt{K}}|v_{PCM}|v_{PCM}+\rho_{PCM}g\varepsilon\beta(T_{PCM}-T_{ref}) \quad (6.8)$$

where g denotes the gravity constant, ε denotes the porosity of the metal foam, μ_{PCM} denotes the dynamic viscosity of the PCM, ρ_{PCM} denotes the density of the PCM, K is the permeability coefficient (Calmidi and Mahajan, 2000), C_f denotes the inertial factor for fluid flow in metal foams, and β denotes the thermal expansion coefficient of the PCM.

The PCM flow resistances consist of three parts: firstly, the first-order resistance (Darcy term) which is denoted by the third terms on the right hand side of Eq. (6.7) and Eq. (6.8); secondly, the second-order resistance (Forchheimer correction term) which is denoted by the fourth terms on the right hand side of Eq. (6.7) and Eq. (6.8); thirdly, the Brinkman viscous resistance which is denoted by the second terms on the right hand side of Eq. (6.7) and Eq. (6.8). The last term on the right hand side of Eq. (6.8) represents the buoyancy force caused by temperature differences inside the PCM, and it is the driving force of natural convection. The intensity of natural convection mainly depends on two factors: driving force and resisting force. The driving force increases with increasing temperature differences, whilst the resisting force can be reduced by decreasing the viscosity (μ_{PCM}) of the PCM used. With fixed temperature differences, larger viscosity results in a weaker natural convection. With fixed viscosity, larger temperature differences result in a stronger natural convection. Eqs. (6.6) to (6.8) are used to describe the buoyancy-driven fluid flow, but they also hold true when natural convection does not take place, which is just a special case when μ_{PCM} is infinite. The present study treats the non-convection heat

transfer region as a special case of natural convection ($\mu_{PCM} = +\infty$), so that all cases can use the same equations thus simplifying the subsequent simulation work. When implementing numerical simulation, the program can automatically make the following judgement: if the PCM is still in solid state, its viscosity will be assigned an infinite value to ensure the absence of natural convection; once the PCM finishes melting and becomes liquid, the real value of its viscosity will be assigned, so that the buoyancy forces can be precisely decided.

6.3.4.2 Equations of phase change heat transfer

In order to cope with the phase change heat transfer problem, the Enthalpy Method (Tian and Zhao, 2011a) has been employed in this study. The correlation between the PCM enthalpy function $H_{PCM}(x, y, t)$ and its temperature function $T_{PCM}(x, y, t)$ is given by Eq. (6.4). Under the Cartesian coordinate system, the energy equations for the PCM and metal foam can be written as:

$$\rho_{MF} c_{p.MF} (1-\varepsilon) \frac{\partial T_{MF}}{\partial t} = \bar{k}_{MF} \left(\frac{\partial^2 T_{MF}}{\partial x^2} + \frac{\partial^2 T_{MF}}{\partial y^2} \right) - h_{sf} a_{sf} \left(T_{MF} - T_{PCM} \right) \tag{6.9}$$

$$\begin{aligned} &\rho_{PCM} \varepsilon \frac{\partial H_{PCM}}{\partial t} + \rho_{PCM} c_{p.PCM} \varepsilon \left(u_{PCM} \frac{\partial T_{PCM}}{\partial x} + v_{PCM} \frac{\partial T_{PCM}}{\partial y} \right) \\ &= \bar{k}_{PCM} \left(\frac{\partial^2 T_{PCM}}{\partial x^2} + \frac{\partial^2 T_{PCM}}{\partial y^2} \right) + h_{sf} a_{sf} \left(T_{MF} - T_{PCM} \right) \end{aligned} \tag{6.10}$$

where $\bar{k}_{MF}$ is the effective thermal conductivity of the metal foam when PCM is not saturated), $\bar{k}_{PCM}$ is the effective thermal conductivity of the porous PCM when metal foam is taken off, their method of calculation is given in Section 3.2.2 of Chapter 3; h_{sf} is the inter-phase heat transfer coefficient between metal ligaments and PCM, and a_{sf} is specific surface area of the metal foam. Their values are obtained by employing the

model by Calmidi and Mahajan (2000), the detail of which is given in Section 4.2.4 in Chapter 4.

In Eq. (6.9) and Eq. (6.10), the first and second terms on the right hand side represent heat conduction and inter-phase heat transfer, respectively. The second term on the left hand side of Eq. (6.10) represents the convection term for PCM, which equals zero before natural convection occurs ($u_{PCM} = v_{PCM} = 0$).

6.3.4.3. Initial and boundary conditions

The governing equations in this study are Eqs. (6.3), (6.4) and (6.6)–(6.10). Their initial conditions are given by:

$$u_{PCM}\big|_{t=0} = v_{PCM}\big|_{t=0} = 0 \tag{6.11}$$

$$T_{PCM}\big|_{t=0} = T_{MF}\big|_{t=0} = 20^{\circ}\mathrm{C} \tag{6.12}$$

$$T_{HTF}\big|_{t=0} = 100^{\circ}\mathrm{C} \tag{6.13}$$

Boundary conditions are:

$$u_{PCM}, v_{PCM}\big|_{x=0} = u_{PCM}, v_{PCM}\big|_{x=\mathrm{L}_1} = u_{PCM}, v_{PCM}\big|_{x=\mathrm{L}_1+\mathrm{L}_2} = u_{PCM}, v_{PCM}\big|_{x=\mathrm{L}_1+\mathrm{L}_2+\mathrm{L}_3} = 0 \tag{6.14}$$

$$u_{PCM}\big|_{y=\pm \mathrm{h}_1/2} = v_{PCM}\big|_{y=\pm \mathrm{h}_1/2}\, 0 \tag{6.15}$$

$$T_{HTF}\big|_{x=0} = 100 \tag{6.16}$$

Eq. (6.14) and Eq. (6.15) give the non-slip boundary conditions of PCM velocities. Eq. (6.16) gives the HTF temperature T_{HTF} at its left boundary. T_{HTF} is a function of only horizontal coordinate x and time t, because the thermal resistance of HTF in the y-direction can be neglected when Bi is much greater than 1, as discussed in Section 6.3.2.

The heat released from HTF is transferred to PCM and metal foam, but the percentage between PCM and metal foam needs to be carefully decided for an accurate calculation

result. Calmidi and Mahajan (2000) used an explicit presumption to decide the percentage of the heat absorbed by PCM and metal foam at their common boundary, with PCM being $\bar{k}_{PCM}/(\bar{k}_{MF}+\bar{k}_{PCM})\times 100\%$ and metal foam being $\bar{k}_{MF}/(\bar{k}_{MF}+\bar{k}_{PCM})\times 100\%$. Such presumption can make the simulation simpler and quicker, but meanwhile it results in inaccuracy. Exact percentages between PCM and metal foam should be decided by an implicit relationship, which were given by Tian and Zhao (2011a and 2012b), shown in Eqs. (6.17) and (6.18):

$$\rho_{HTF} c_{p.HTF} (\mathrm{h}_2\text{-}\mathrm{h}_1) u_{HTF} \frac{\partial T_{HTF}}{\partial x} = \bar{k}_{MF} \left.\frac{\partial T_{MF}}{\partial y}\right|_{y=+\mathrm{h}_1/2} + \bar{k}_{PCM} \left.\frac{\partial T_{PCM}}{\partial y}\right|_{y=+\mathrm{h}_1/2} \tag{6.17}$$

$$T_{MF}\big|_{y=+\mathrm{h}_1/2} = T_{PCM}\big|_{y=+\mathrm{h}_1/2} = T_w \tag{6.18}$$

At the upper boundary, Eq. (6.17) reflects energy conservation between HTF and PCM-metal foam. Here, another restrictive condition is from the temperature continuity – both metal foam and PCM should have the same temperature as the wall temperature at their common boundary, as shown in Eq. (6.18). Such combined implicit boundary condition shown in Eqs. (6.17) and (6.18) can achieve better accuracy due to its avoidance of extra presumption. Similarly, the boundary conditions for the lower boundary have been obtained as follows:

$$\rho_{HTF} c_{p.HTF} (\mathrm{h}_2\text{-}\mathrm{h}_1) u_{HTF} \frac{\partial T_{HTF}}{\partial x} = -\bar{k}_{MF} \left.\frac{\partial T_{MF}}{\partial y}\right|_{y=-\mathrm{h}_1/2} - \bar{k}_{PCM} \left.\frac{\partial T_{PCM}}{\partial y}\right|_{y=-\mathrm{h}_1/2} \tag{6.19}$$

$$T_{MF}\big|_{y=-\mathrm{h}_1/2} = T_{PCM}\big|_{y=-\mathrm{h}_1/2} = T_w \tag{6.20}$$

The energy conservation at the lower boundary is shown in Eq. (6.19), with the temperature continuity condition being given in Eq. (6.20).

Due to perfect thermal insulation, all four horizontal boundaries are adiabatic, giving:

$$\left.\frac{\partial T_{PCM}}{\partial x}\right|_{x=0} = \left.\frac{\partial T_{PCM}}{\partial x}\right|_{x=\mathrm{L}_1} = \left.\frac{\partial T_{PCM}}{\partial x}\right|_{x=\mathrm{L}_1+\mathrm{L}_2} = \left.\frac{\partial T_{PCM}}{\partial x}\right|_{x=\mathrm{L}_1+\mathrm{L}_2+\mathrm{L}_3} = 0 \tag{6.21}$$

$$\left.\frac{\partial T_{MF}}{\partial x}\right|_{x=0} = \left.\frac{\partial T_{MF}}{\partial x}\right|_{x=L_1} = \left.\frac{\partial T_{MF}}{\partial x}\right|_{x=L_1+L_2} = \left.\frac{\partial T_{MF}}{\partial x}\right|_{x=L_1+L_2+L_3} = 0 \qquad (6.22)$$

6.3.4.4. Modelling of metal foam microstructures

There are several important parameters for metal foam microstructures that need to be determined for solving the governing equations, which are Eqs. (6.3), (6.4) and (6.6)–(6.10). These include: permeability, inertial factor, pore size, metal fibre diameter, effective thermal conductivity, surface area density, and inter-phase heat transfer coefficient. The determination of these parameters is complicated and strongly depends on special microstructures inside metal foams. Several existing models proposed by previous researchers are employed. Details of their derivation formula are given in Section 3.1.3 of Chapter 3, and in Sections 4.2.2 and 4.2.4 of Chapter 4.

6.4. Numerical procedure

A Finite Volume Method (FVM)-based program was developed by the author to solve Eqs. (6.3), (6.4) and (6.6)–(6.10), which are the governing equations of the current physical problem. The program was compiled and executed in Visual Fortran®. Coupled heat conduction and natural convection equations were solved simultaneously by employing the SIMPLER algorithm (Semi-Implicit Method for Pressure Linked Equations Revised) (Patankar, 1980) in a non-uniform mesh (1200×200). The source code has been given in the Appendix of this Thesis. The PLS (Power Law Scheme) (Patankar, 1981) was employed to discretise convection-diffusion terms to save computing time whilst ensuring high accuracy. In the *x*-direction (total length: 10.5 m), 1200 uniform grids were used, with each grid 0.00875 m in length, while in the *y*-direction (total length: 0.02 m), 200 grids were used in *y*-direction, with each grid 1.0×10^{-4} m in length. Mesh independency was also examined, and it was found that a 2400×400 mesh could only improve the accuracy by 0.17% compared to the 1200×200 mesh,

meaning a finer mesh is not needed. It should be noted that this difference of 0.17% means the relative difference of the calculated temperature field averaged on each grid between the two mesh systems amounts to 0.17%. Due to different convergence rates in the three metal-foam samples, the optimised time step was found to be 5×10^{-3} s for the metal foam of 95% porosity and 10 ppi, 3×10^{-3} s for the metal foam of 95% porosity and 30 ppi, and 2×10^{-3} s for the metal foam of 85% porosity and 30 ppi. Time step independency was also examined, and it was found that for the metal foam of 95% porosity and 10 ppi, the difference between 2.5×10^{-3} s and 5×10^{-3} s was 0.23%; for the metal foam of 95% porosity and 30 ppi, the difference between 1.5×10^{-3} s and 3×10^{-3} s was 0.22%; for the metal foam of 85% porosity and 30 ppi, the difference between 1.0×10^{-3} s and 2×10^{-3} s was 0.23%. Numerical simulations were set to stop when the difference between two consecutive iterations was less than 10^{-6} (i.e. 0.0001%). The program was run on a high performance HP® Z1 Workstation powered by the quad-core Intel® Xeon® processor and 8GB RAM (Random Access Memory). Total computational time was 41.5 hours, 72.3 hours and 108.8 hours for 95% porosity and 10 ppi, 95% porosity and 30 ppi, and 85% porosity and 30 ppi, respectively (Tian and Zhao, 2012b).

The numerical programming needs to ensure that natural convection only takes place at the grids where the PCM is in its liquid state and does not take place at the grids where the PCM is still in its solid state. This is realised by only assigning the real viscosity value to the grids where the PCM is liquid whilst assigning a viscosity with the value of 10^{10} to the grids where the PCM is still solid.

6.5. Results and discussions

6.5.1. Validation

To ensure the simulation accuracy and correctness, the numerical program was tested for a simple case of the single-stage PCM-embedded metal foam. This does not affect the

accuracy and correctness of the numerical program to be applied to multiple-PCM embedded metal foams, because the flow and heat transfer equations remain the same. Details of the test rig are given in Section 4.4.1 of Chapter 4. Figure 6.2(a) is reproduced here from Figure 4.2 to show the experimental setup, Figure 6.2(b) shows the test section, which comprised a piece of rectangular copper foam (with the dimension of 200×120×25 mm) with paraffin wax RT58 embedded in it. According to the PCM provider Rubitherm®, the thermo-physical properties of RT58 are listed in Table 6.2. The metal foam was sintered onto a thin copper plate from the bottom side for better thermal contact. Attached to the copper plate was an electrical heater, made of flexible silicon with adjustable heat flux, providing continuous and uniform heat flux for the PCM and metal foam. The temperatures were automatically recorded by a data acquisition system. As shown in Chapter 4, the overall uncertainty of the test was estimated at 6.67%.

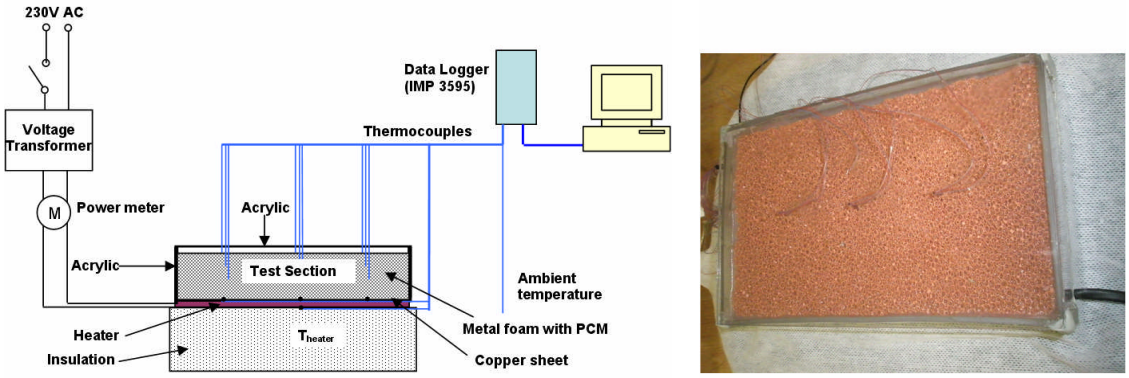

(a) Experimental setup (b) Test section

Figure 6.2. The experimental test rig.

Table 6.2. Thermal properties of RT58 (Rubitherm® Technologies GmbH, Germany).

PCM	Density (kg/m^3)	Nominal melting temperature (℃)	Latent heat per kg (kJ/kg)	Latent heat per m^3 (MJ/m^3)
RT 58	880	48-62	181	159
	Specific heat (kJ/kg ℃)	Thermal conductivity (W/ m K)	Thermal expansion coefficient (K^{-1})	Dynamic viscosity (Pa·s)
	2.1	0.20	1.1×10^{-4}	0.0269

Similar to Chapter 4, the numerical results and the corresponding experimental data were compared for the locations: y = 0 mm and 8 mm. Here, y denotes the distance between different locations and the heating plate. Numerical simulation indicated that roughly the same results were obtained in this case as those shown in Figure 4.5. This is reasonable because the same set of flow and heat transfer equations has been used in both Chapters. Very good agreement was achieved between numerical results and experimental data as shown in Chapter 4, so the validation in this case is also justified.

6.5.2. Natural convection

Natural convection was examined by numerical simulations. Figure 6.3 (Tian and Zhao, 2012b) shows the flow profiles of natural convection for CTES at dimensionless time = 10 when all three PCMs have finished their melting processes. Dimensionless time is defined as the real time divided by a reference time which equals to the melting time of PCM 2. Three dotted squares in Figure 6.3 denote the rectangular enclosures containing PCM 1 (left), PCM 2 (middle) and PCM 3 (right) respectively. Inside each PCM, two eddies are formed: the larger eddy (clockwise) is situated near the left bottom corner whilst the smaller eddy (anti-clockwise) is situated near the right top corner. It is reasonable to have two such eddies in each PCM, because the PCM and HTF

temperatures decrease along the *x*-axis (the HTF flow direction), resulting in the PCM on the left having lower density and therefore moving upward, and the PCM on the right having higher density and therefore moving downward. The larger eddy is caused by temperature differences, and is the dominating eddy. The smaller eddy seems to have been formed by the wake flow of the dominating eddy, and is the non-dominating eddy. None of these eddies is situated near the left top corner, because the PCM near the upper boundary has higher temperature (closer to HTF) and so lacks driving forces for natural convection to take place. It can also be noted in Figure 6.3 that the dominating eddies, the ones near the left bottom corner, tend to become smaller in size along the *x*-axis. The reason can be attributed to the fact that the temperature differences, which are the driving forces of natural convection, get smaller along the *x*-axis.

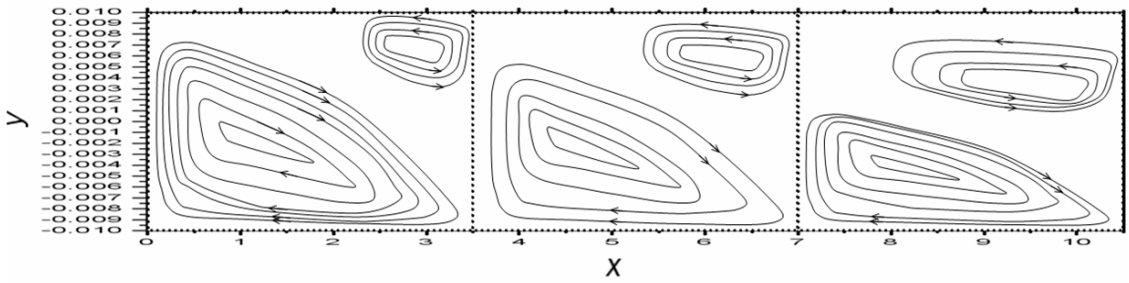

Figure 6.3. Flow profiles of natural convection for CTES.

The numerical simulation also examined natural convection for MF-CTES (Metal Foam-enhanced Cascaded Thermal Energy Storage). However, the flow velocities caused by buoyancy force are found to be rather low, with an order of magnitude of 10^{-4} m/s. At first sight, this may seem surprising, but it is still believed to be reasonable, for the following reason. The buoyancy force term $\rho_{PCM} g \beta \Delta T$, which drives natural convection, has an order of magnitude of 10^2, but in the main drag force term $-\mu_{PCM} u_{PCM} / K$ (i.e.

Darcy term), μ_{PCM}/K has an order of magnitude of 10^6. According to Equilibrium of Forces, drag force should have a similar order of magnitude to buoyancy force, and therefore u_{PCM} should have an order of magnitude of 10^{-4}. The PCMs used in this study has high dynamic viscosity of 0.0251 Pa·s – 0.0400 Pa·s (1000 times higher than air) and low thermal expansion coefficient of 1.1×10^{-4} K^{-1} (30 times lower than air), so these special physical characteristics result in the velocity driven by buoyancy force being insignificant in this case. Natural convection therefore fails to produce dominant influence on heat transfer for MF-CTES.

6.5.3. Effect of metal foam microstructure on equivalent heat exchange rate

Equivalent heat exchange rate was examined by numerical simulations for MF-CTES. Figure 6.4 compares the heat exchange rates of MF-CTES between three copper-foam samples, the properties of which are listed in Table 6.3. As shown in Figure 6.4, Sample C (85% porosity) has better heat transfer performance than Samples A and B (both 95% porosity). This is reasonable because the former has more solid structures, which results in higher effective thermal conductivity; thus it can transfer heat flux more efficiently to PCMs through the metal foam skeleton. Sample B (30ppi pore density) has better heat transfer performance than Sample A (10ppi pore density). This is also reasonable because higher pore density results in larger contact area between PCMs and metal ligaments so that more heat can be transferred.

In summary, the metal-foam samples with low porosity and high pore density have better heat transfer performance than the ones with high porosity and low pore density.

Table 6.3. Metal foam properties.

Properties	Porosity ε	Pore density	k_s in Eqs. (3.6b) to (3.6e)
Sample A	0.95 (95%)	10ppi	350 W/(m K)
Sample B	0.95 (95%)	30ppi	350 W/(m K)
Sample C	0.85 (85%)	30ppi	350 W/(m K)

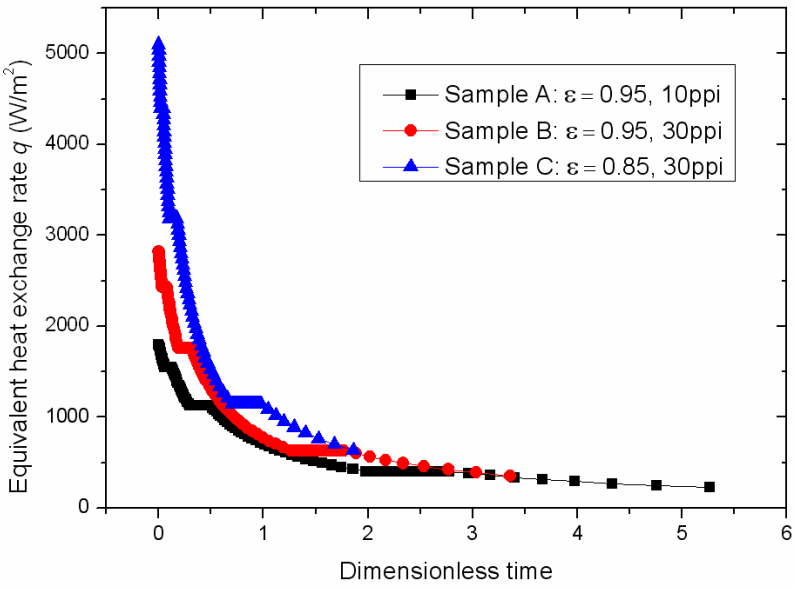

Figure 6.4. Comparison of equivalent heat exchange rates q (W/m^2) between three different metal-foam samples in MF-CTES.

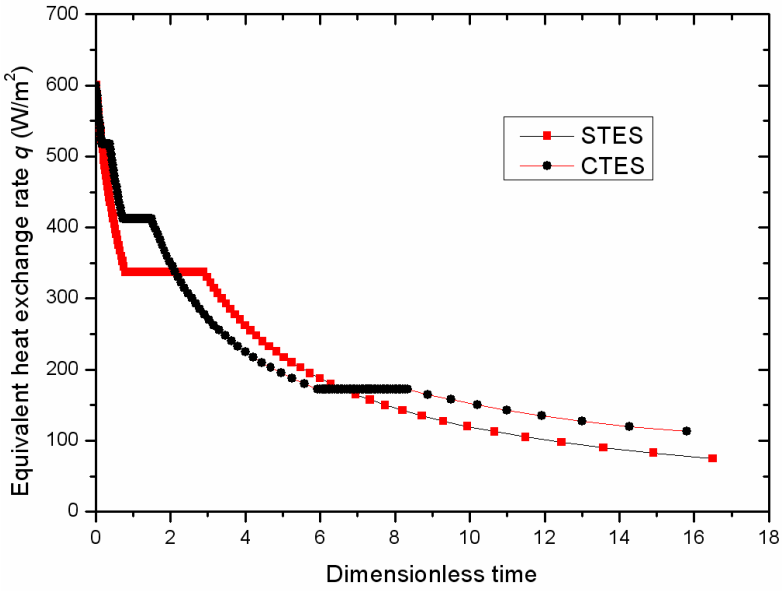

Figure 6.5. Comparison of equivalent heat exchange rates q (W/m^2) between CTES and STES.

To better show the advantage of MF-CTES over CTES and STES which were studied in Chapter 5, Figure 5.2(a) is reproduced here as Figure 6.5. It can be seen that MF-CTES enhances heat transfer by 2–7 times and reduces melting time by 67%–87% (depending on the properties of the metal-foam sample used) compared to CTES, and that CTES enhances heat transfer by an average factor of 30% compared to STES.

6.5.4. Effect of metal foam microstructure on exergy efficiency

Exergy efficiency was examined by numerical simulations for MF-CTES. Figure 6.6 shows exergy efficiency of MF-CTES of three different copper-foam samples, indicating that Sample A, B and C have all achieved similar exergy efficiency, with the only difference being the melting time: Sample C is the shortest, Sample B is longer, and Sample A is the longest. The reason is given in Section 6.5.3.

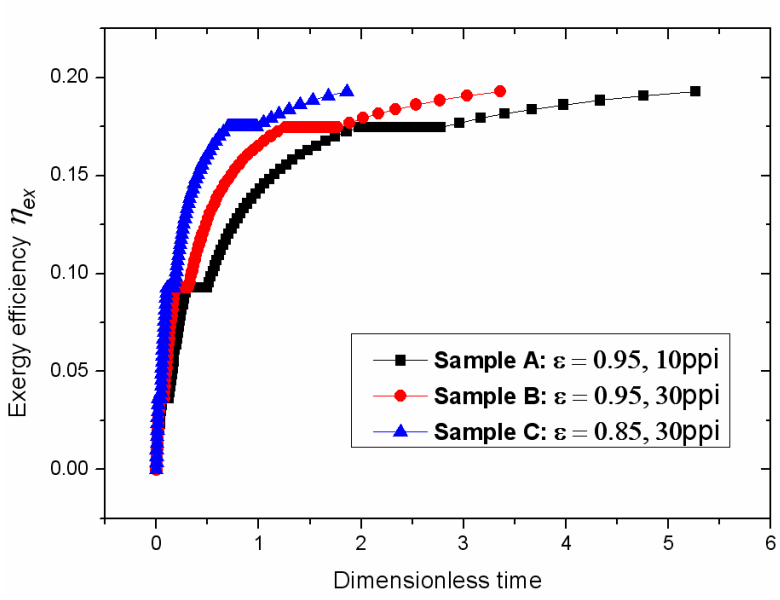

Figure 6.6. Comparison of exergy efficencies η_{ex} (%) between three different metal-foam samples in MF-CTES.

CTES and STES were studied in Chapter 5. Figure 5.3(a) which gives their exergy efficiency is reproduced here as Figure 6.7 to make a comparison of them with MF-CTES. It can be seen that CTES does not always have higher exergy efficiency than STES (-20% to +30%), and overall, there is not much difference between CTES and STES. MF-CTES has roughly the same exergy efficiency as CTES and STES, and the only difference is that MF-CTES has much shorter melting time than CTES and STES.

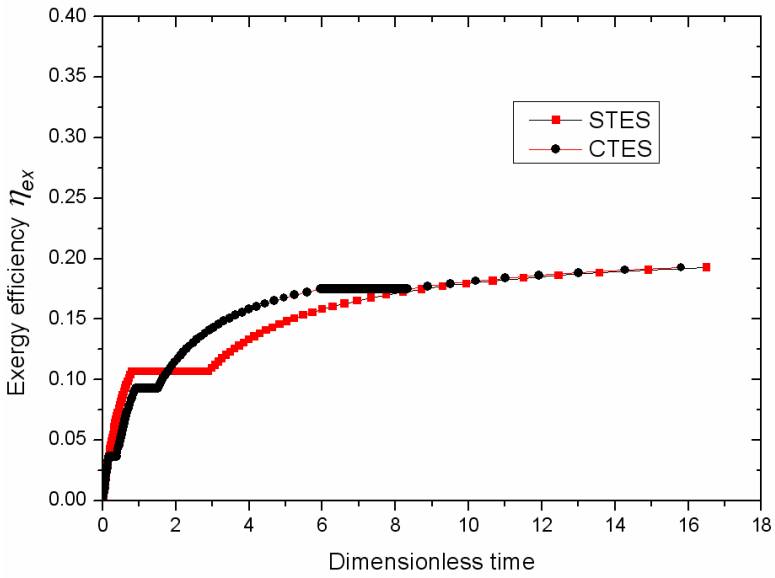

Figure 6.7. Comparison of exergy efficency η_{ex} (%) between STES and CTES.

In summary, metal foams cannot further improve exergy efficiency for CTES, but they can help CTES to finish melting more quickly by having a much higher heat exchange rate.

6.5.5. Effect of metal foam microstructure on exergy transfer rate

According to the Second Law of Thermodynamics (Carnot et al., 1899), heat exchange rate q in Section 6.5.3 cannot reflect the real energy efficiency of a thermal system. Thus, the concept of exergy transfer rate $h_{ex,}$ which has been proposed in Chapter 5, is used to evaluate the overall thermal performance of STES, CTES and MF-CTES.

$$h_{ex} = q \times \eta_{ex} \ (\mathrm{W/m^2}) \tag{6.23}$$

h_{ex} is the effective exergy transfer rate, representing how much useful thermal energy is transferred from HTF to PCMs during charging processes.

Effective exergy transfer rates h_{ex} were obtained by numerical simulations for MF-CTES. Figure 6.8 shows h_{ex} of three different copper-foam samples, indicating that Sample C has higher h_{ex} than Sample B and that Sample B has higher h_{ex} than Sample A. This is because the sample with higher heat exchange rate will have higher exergy transfer rate when all the samples have roughly the same exergy efficiency η_{ex}. Section 6.5.3 has shown that Sample C has the highest heat exchange rate q whilst Sample A has the lowest heat exchange rate.

Figure 5.4(a) which gives h_{ex} for CTES and STES is reproduced here as Figure 6.9 to make a comparison of them with MF-CTES. It can be seen that all metal-foam samples produce much higher h_{ex} (by 2–7 times) than CTES, and that CTES nearly always produces higher exergy transfer rate (up to 22%) than STES. CTES only delivers slightly lower exergy transfer rate than STES, when PCM 1 starts phase change and when PCM 4 finishes phase change. The reasons are given in Section 5.5 of Chapter 5.

In summary, CTES nearly always has higher exergy transfer rates (up to 22%) than STES; MF-CTES can further increase exergy transfer rates of CTES by 2–7 times.

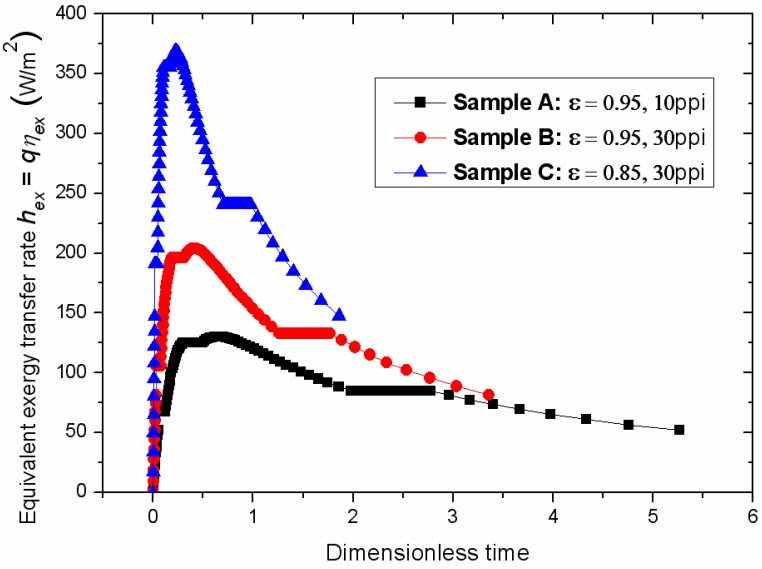

Figure 6.8. Comparison of equivalent exergy transfer rate h_{ex} (W/m^2) between three different metal-foam samples in MF-CTES.

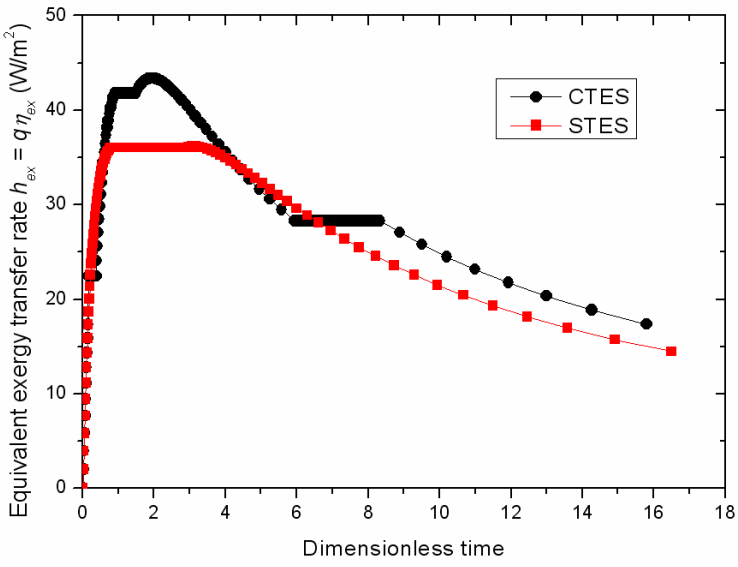

Figure 6.9. Comparison of equivalent exergy transfer rate h_{ex} (W/m^2) between STES and CTES.

6.6. Conclusion

CTES enhances heat transfer by up to 30% compared to STES. MF-CTES enhances heat transfer by 2–7 times compared to CTES, depending on the properties of metal-foam samples (porosity, pore density and metal thermal conductivity). Simulation results indicate that the metal foams with lower porosity and higher pore density have better heat transfer performance than the ones with higher porosity and lower pore density.

CTES does not always have higher exergy efficiency than STES (-20% to +30%). MF-CTES cannot further improve exergy efficiency for CTES, but can help CTES to finish melting more quickly by having higher heat exchange rates (melting time reduced by 67% to 87%).

CTES nearly always has higher exergy transfer rate (up to 22%) than STES. MF-CTES can further increase exergy transfer rate of CTES by 2–7 times.

Chapter 7. Conclusions and Suggestions for Further Work

7.1. Conclusions

Fluid flow, heat conduction and natural convection of PCM-embedded metal foams have been investigated in this Thesis, for both single-PCM storage and multiple-PCM storage. The main conclusions are given below.

- *Heat conduction in metal foams*

Metal foams can effectively enhance the heat conduction rate of Phase Change Materials (PCMs) by 5–20 times. This can be attributed to three excellent properties of metal foams: high thermal conductivity, high specific surface area and continuous inter-connected structure. High thermal conductivity helps to draw heat rapidly; high specific surface area increases the heat transfer area between metal foam and the PCM embedded in it; continuous inter-connected structure reduces the thermal resistance and helps to spread heat across the whole PCM more efficiently.

- *Natural convection in metal foams*

Despite having high porosity, metal foams have large flow resistance. More importantly, most paraffin-type PCMs have rather high viscosity and low thermal expansion coefficient, so the driving force of natural convection tends to be quite weak. Natural convection was found to be suppressed when metal foams were used. At the heat conduction-dominated zone, heat transfer rate can be increased by 5–20 times when metal foams are used. After considering the reduced heat transfer enhancement at the convection-dominated zone, metal foams can still achieve a better overall heat transfer rate (3–10 times) than the pure PCM sample. Whether in heat conduction or in natural convection, better heat transfer performance is always achieved by metal foams of higher pore density and lower porosity, because higher pore density means larger heat contact

area between the metal foam and the PCM, and lower porosity means higher effective thermal conductivity.

- *Cascaded Thermal Energy Storage (CTES)*

Cascaded Thermal Energy Storage (CTES) achieves higher heat transfer performance (overall 30%) than Single-stage Thermal Energy Storage (STES), by maintaining a relatively high temperature difference during heat exchange process. However, CTES does not always have a higher exergy efficiency (-20% to 30%) than STES, because in CTES the PCM with the lowest melting point delays the temperature rise during the charging process. Overall, CTES still has higher effective exergy transfer rate (22%) than STES.

- *Metal Foam-enhanced Cascaded Thermal Energy Storage (MF-CTES)*

Metal Foam-enhanced Cascaded Thermal Energy Storage (MF-CTES) can further increase heat transfer rate of CTES by 2–7 times, depending on the properties of the metal-foam samples used (higher pore density and lower porosity can achieve a better performance). MF-CTES cannot improve exergy efficiency of CTES, but can help CTES to finish melting more quickly by having higher heat transfer rates (melting time reduced by 67%–87%). In addition, exergy transfer rate of CTES is further increased by 2–7 times if MF-CTES is used.

In summary, the use of metal foams and CTES has been investigated for their heat transfer enhancement in PCM applications. They are both capable of improving heat transfer, but for different situations. Metal foams improve the heat transfer of PCMs themselves, whilst CTES helps to boost the heat transfer between PCMs and the rest of the heat exchange system when heat transfer inevitably deteriorates following the drop of

the temperature difference. Both situations could happen in real applications, which can be significantly improved by use of MF-CTES.

7.2. Suggestions for further work

- *Thermal radiation under high temperatures*

Heat conduction and natural convection have been studied in this Thesis. These are the two dominant heat transfer modes under low-medium working temperatures (below 300 ºC). However, thermal radiation is no longer negligible under high working temperatures (above 300 ºC). So a possible extension of the present work would be to examine thermal radiation in the PCM-embedded metal foams at high temperatures. A spectral analysis will be needed to examine the effects of metal material, porosity and pore density on thermal radiation.

- *Material compatibility*

Metal foams have shown excellent capability to enhance heat transfer in PCMs. Before applying them to real application, a study of their anti-corrosion for the long-term use is still needed, especially under high temperatures. Metal foams made of different materials will need to be tested for their compatibility with the PCMs commonly used in real applications.

- *Further investigation of Cascaded Thermal Energy Storage*

Relevant studies in this Thesis lack a more detailed and parametric simulation of Cascaded Thermal Energy Storage (CTES) and Metal Foam-enhanced Thermal Energy Storage (MF-CTES). Further investigations should be conducted to consider the effects of more influencing parameters, such as Heat Transfer Fluid (HTF) flow rates, different permutations of PCMs along the HTF flow direction, and optimisation of melting temperatures. In addition, the current exergy analysis has only considered the PCM side

but neglected the HTF side, and therefore needs to be improved. Future work needs to be conducted for both PCMs and HTF, giving a more accurate energy evaluation.

References

Berber, S., Kwon, Y.K., Tománek, D., 2000. Unusually high thermal conductivity of carbon nanotubes. *Phys. Rev. Lett.* **84**, 4613–4616.

Bhattacharya, A., Calmidi, V.V., Mahajan, R.L., 2002. Thermophysical properties of high porosity metal foams. *Int. J. Heat Mass Tran.* **45**, 1017–1031.

Boomsma, K., Poulikakos, D., 2001. On the effective thermal conductivity of a three-dimensionally structured fluid-saturated metal foam. *Int. J. Heat Mass Tran*. **44**, 827–836.

Brinkman, H.C., 1947. A calculation of the viscous force exerted by a flowing fluid on a dense swarm of particles. *Appl. Sci. Res.* **A1**, 27–34.

Buddhi, D., 1997. Thermal performance of a shell and tube PCM storage heat exchanger for industrial waste heat recovery. In: *Proceedings of the ISES 1997 Solar World Congress*, Taejon, Korea.

Calmidi, V.V., 1998. Transport phenomena in high porosity metal foams. *Ph.D. Thesis*, University of Colorado, U.S.A.

Calmidi, V.V., Mahajan, R.L., 1999. The effective thermal conductivity of high porosity fibrous metal foams. *J. Heat Trans. – T ASME* **121**, 466–471.

Calmidi, V.V., Mahajan, R.L., 2000. Forced convection in high porosity metal foams. *J. Heat Trans. – T ASME* **122**, 557–565.

Carnot, S., Clausius, R., Kelvin, W., 1899. *The second law of thermodynamics: memoirs by Carnot, Clausius and Thomson*, Haper & Brothers, New York, U.S.A.

Couper, J.R., Penney, W.R., Fair J.R., Walas, S.M., 2010. *Chemical process equipment: selection and design,* 2nd Edition, Butterworth-Heinemann (an imprint of Elsevier), Burlington, U.S.A.

Darcy, H., 1856. *Les Fontaines Publiques de la Ville de Dijon*, Victor Dalmont, Paris, France.

Dincer, I., Rosen, M.A., 2010. *Thermal Energy Storage: Systems and Applications*, 2nd Edition, John Wiley & Sons, West Sussex, U.K.

Domanski, R., El-Sebaii, A.A., Jaworski, M., 1995. Cooking during off-sunshine hours using PCMs as storage media. *Energy* **20**, 607–616.

Dukhan, N., 2010. An improved PCM heat storage technology utilizing metal foam. In: *Proceedings of the 12th IEEE Intersociety Conference on Thermal and Thermomechanical Phenomena in Electronic Systems (ITherm 2010),* Las Vegas, U.S.A.

Dul'nev, G.N., 1965. Heat transfer through solid disperse systems. *J. Eng. Phys. Thermophys*. **9**, 275–279.

El-Sebaii, A.A., Al-Ghamdi, A.A., Al-Hazmi, F.S., Faidah, A.S., 2009. Thermal performance of a single basin solar still with PCM as a storage medium. *Appl. Energ.* **86**, 1187–1195.

El-Sebaii, A.A., Al-Heniti, S., Al-Agel, F., Al-Ghamdi, A.A., Al-Marzouki, F., 2011. One thousand thermal cycles of magnesium chloride hexahydrate as a promising PCM for indoor solar cooking. *Energ. Convers. Manage.* **52**, 1771–1777.

Ellinger, E.A., Beckermann, C., 1991. On the effect of porous layers on melting heat transfer in an enclosure. *Exp. Therm. Fluid Sci.* **4**, 619–629.

Ervin, G., 1977. Solar heat storage using chemical reactions. *J. Solid State Chem.* **22**, 51–61

Fan, L., Khodadadi, J.M., 2011. Thermal conductivity enhancement of phase change materials for thermal energy storage: a review. *Renew. Sust. Energ. Rev.* **15**, 24–46.

Forchheimer, P., 1901. Wasserbewegung durch Boden (Water movement through soil). *Forsch. Ver. D. Ing.* **45**, 1782–1788.

Foster, M., 2002. Theoretical investigation of the system SnO_x/Sn for the thermochemical storage of solar energy. In: *Proceedings of the 11th Solar PACES International Symposium on Concentrated Solar Power and Chemical Energy Technologies*, Zürich, Switzerland. Later published in *Energy* **29**, 789–799.

Fourie, J.G., Du Plessis, J.P., 2002. Pressure drop modelling in cellular metallic foams. *Chem. Eng. Sci.* **57**, 2781–2789.

Gil, A., Medrano, M., Martorell, I., Lázaro, A., Dolado, P., Zalba, B., Cabeza, L.F., 2010. State of the art on high temperature thermal energy storage for power generation. Part 1 – concepts, materials and modellization. *Renew. Sust. Energ. Rev.* **14**, 31–55.

Gong, Z.X., Mujumdar, A.S., 1997. Thermodynamic optimization of the thermal process in energy storage using multiple phase change materials. *Appl. Therm. Eng.* **17**, 1067-1083.

Han, X.X., Tian, Y., Zhao, C.Y., 2013. An effectiveness study of enhanced heat transfer in Phase Change Materials (PCMs). *Int. J. Heat Mass Tran.* **60**, 459–468.

Hauer, A., 2007. Sorption theory for thermal energy storage. Chapter 24 in Book: *Thermal energy storage for sustainable energy consumption*. NATO Science Series, Springer, Netherlands, Volume **234**, Part VI, 393–408.

Holman, J.P., 1997. *Heat transfer*, 8th Edition, McGraw-Hill Companies, New York, 143–144.

Hwang, J.J., Hwang, G.J., Yeh, R.H., Chao, C.H., 2002. Measurement of interstitial convective heat transfer and frictional drag for flow across metal foams. *J. Heat Trans.–T ASME* **124**, 120 – 129.

Jegadheeswaran, S., Pohekar, S.D., 2009. Performance enhancement in latent heat thermal storage system: a review. *Renew. Sust. Energ. Rev.* **13**, 2225–2244.

Kato, Y., Takahashi, R., Sekiguchi, T., Ryu, J., 2009. Study on medium-temperature chemical heat storage using mixed hydroxides. *Int. J. Refrig.* **32**, 661–666

Kato, Y., Yamada, M., Kanie, T., Yoshizawa, Y., 2001. Calcium oxide/carbon dioxide reactivity in a packed bed reactor of a chemical heat pump for high-temperature gas reactors. *Nucl. Eng. Des.* **210**, 1–8.

Kim, S.Y., Kang, B.H., Kim, J.H., 2001. Forced convection from aluminium foam materials in an asymmetrically heated channel. *Int. J. Heat Mass Tran.* **44**, 1451–1454.

Kim, S.Y., Paek, J.W., Kang, B.H., 2000. Flow and heat transfer correlations for porous fin in a plate-fin heat exchanger. *J. Heat Trans.– T ASME* **122**, 572–578.

Krane, R.J., 1987. A second law analysis of the optimum design and operation of thermal energy storage systems. *Int. J. Heat Mass Tran.* **30**, 43–57.

Krishnan, S., Murthy, J.Y., Garimella, S.V., 2005. A two-temperature model for solid-liquid phase change in metal foams. *J. Heat Trans.– T ASME* **127**, 997–1004.

Kuznik, F., David, D., Johannes, K., Roux, J.J., 2011. A review on phase change materials integrated in building walls. *Renew. Sust. Energ. Rev.* **15**, 379–391.

Lafdi, K., Mesalhy, O., Elyafy, A., 2008. Graphite foams infiltrated with phase change materials as alternative materials for space and terrestrial thermal energy storage applications. *Carbon* **46**, 159–168.

Lee, Y.C., Zhang, W., Xie, H., Mahajan, R.L., 1993. Cooling of a FCHIP package with 100 W, 1 cm^2 chip. In: *Proceedings of the 1993 ASME International Electronics Packaging Conference*, ASME, New York, Volume **1**, 419–423.

Lovegrove, K., Luzzi, A., Soldiani, I., Kreetz, H., 2004. Developing ammonia based thermochemical energy storage for dish power plants. *Sol. Energ.* **76**, 331–337.

Lu, W., Zhao, C.Y., Tassou, S.A., 2006. Thermal analysis on metal-foam filled heat exchangers, I. metal-foam filled pipes. *Int. J. Heat Mass Tran.* **49**, 2751–2761.

Mazman, M., Cabeza, L.F., Mehling, H., Paksoy, H.O., Evliya, H., 2008. Heat transfer enhancement of fatty acids when used as PCMs in thermal energy storage. *Int. J. Energy Res.* **32**, 135–143.

Medrano, M., Gil, A., Martorell, I., Potou, X., Cabeza, L.F., 2010. State of the art on high-temperature thermal energy storage for power generation. Part 2 – case studies. *Renew. Sust. Energ. Rev.* **14**, 56–72.

Mehling, H., Cabeza, L.F., 2008. Integration of active storages into systems. Chapter 6 in Book: *Heat and cold storage with PCM*, Springer Publication Corporation, Berlin, 189–191.

Mehling, H., Hiebler, S., 2004. Review on PCM in buildings – Current R&D. *IEA Report*, from IEA Task 42 Annex 24: Compact Thermal Energy Storage: Material Development for System Integration.

Mettawee, E.B.S., Assassa, G.M.R., 2006. Experimental study of a compact PCM solar collector. *Energy* **31**, 2958–2968.

Mettawee, E.B.S., Assassa, G.M.R., 2007. Thermal conductivity enhancement in a latent heat storage system. *Sol. Energy* **81**, 839–845.

Michels, H., Pitz-Paal, R., 2007. Cascaded latent heat storage for parabolic trough solar power plants. *Sol. Energy* **81**, 829–837.

Mills, A., Farid, M., Selman, J.R., Al-Hallaj, S., 2006. Thermal conductivity enhancement of phase change materials using a graphite matrix. *Appl. Therm. Eng.* **26**, 1652–1661.

Morton, K.W., Mayers, D.F., 2005. *Numerical solution of partial differential equations*. 2nd edition, Cambridge University Press, UK, pp.16–22.

Nakaso, K., Teshima, H., Yoshimura, A., Nogami, S., Hamada, S., Fukai, J., 2008. Extension of heat transfer area using carbon fiber cloths in latent heat thermal energy storage tanks. *Chem. Eng. Process: Process Intensif.* **47**, 879–885.

Nayak, K.C., Saha, S.K., Srinivasan, K., Dutta, P., 2006. A numerical model for heat sinks with phase change marterials and thermal conductivity enhancers. *Int. J. Heat Mass Tran.* **49**, 1833–1844.

Neeper, D.A., 2000. Thermal dynamics of wallboard with latent heat storage. *Sol. Energy* **68**, 393–403.

Ozmat, B., Leyda, B., Benson, B., 2004. Thermal applications of open-cell metal foams. *Mater. Manuf. Process.* **19**, 839–862.

Paglione, J., Greene, R.L., 2010. High-temperature superconductivity in iron-based materials. *Nat. Phys.* **6**, 645–658.

Pasupathy, A., Velraj, R., Seeniraj, R.V., 2008. Phase change material-based building architecture for thermal management in residential and commercial establishments. *Renew. Sust. Energ. Rev.* **12**, 39–64.

Patankar, S.V., 1980. *Numerical heat transfer and fluid flow*. Hemisphere Publishing Corporation, New York.

Patankar, S.V., 1981. A calculation procedure for two-dimensional elliptic situations. *Numer. Heat Transfer* **4**, 409–425.

Phanikumar, M.S., Mahajan, R.L., 2002. Non-Darcy natural convection in high porosity metal foams. *Int. J. Heat Mass Tran.* **45**, 3781–3793.

Pilkington Solar International GmbH, 2000. Survey of thermal storage for parabolic trough power plants. *NREL Report* (Refererence number: NREL/SR-550-27925). Available at: http://www.nrel.gov/csp/troughnet/pdfs/27925.pdf [Accessed on 16.11.2012].

Prengle, H.W., Sun, C.H., 1976. Operational chemical storage cycles for utilization of solar energy to produce heat or electric power. *Sol. Energ.* **18**, 561–567.

Py, X., Olives, R., Mauran S., 2001. Paraffin/porous-graphite-matrix composite as a high and constant power thermal storage material. *Int. J. Heat Mass Tran.* **44**, 2727–2737.

Rubitherm® Technologies GmbH, Germany <http://www.rubitherm.de> [Accessed on 16.11.2012].

Sarı, A., Karaipekli, A., 2007. Thermal conductivity and latent heat thermal energy storage characteristics of paraffin/expanded graphite composite as phase change material. *Appl. Therm. Eng.* **27**, 1271–1277.

Shabgard, H., Robak, C.W., Bergman, T.L., Faghri, A., 2012. Heat transfer and exergy analysis of cascaded latent heat storage with gravity-assisted heat pipes for concentrating solar power applications. *Sol. Energy* **86**, 816–830.

Sharma, A., Tyagi, V.V., Chen, C.R., Buddhi, D., 2009. Review on thermal energy storage with phase change materials and applications. *Renew. Sust. Energ. Rev.* **13**, 318–345.

Sharma, S.D., Iwata, T., Kitano, H., Sagara, K., 2005. Thermal performance of a solar cooker based on an evacuated tube solar collector with a PCM storage unit. *Sol. Energy* **78**, 416-426.

Shatikian, V., Ziskind, G., Letan, R., 2008. Numerical investigation of a PCM-based heat sink with internal fins: constant heat flux. *Int. J. Heat Mass Tran.* **51**, 1488–1493.

Shukla, A., Buddhi, D., Sawhney, R.L., 2008. Thermal cycling test of few selected inorganic and organic phase change materials. *Renew. Energ.* **33**, 2606–2614.

Siahpush, A., O'Brien, J., Crepeau, J., 2008. Phase change heat transfer enhancement using copper porous foam. *J. Heat Trans. – T ASME* **130**, 082301–1–11.

Stritih, U., 2004. An experimental study of enhanced heat transfer in rectangular PCM thermal storage. *Int. J. Heat Mass Tran.* **47**, 2841–2847.

Thomson, W., 1887. On the division of space with minimum partitional area. *Phil. Mag.* **24**, 503–514.

Tian, Y., 2012. Phase change convective heat transfer in high porosity cellular metal foams. In Book: *Focus on Porous Media Research*. Nova Science Publishers Inc., New York (ISBN: 978-1-62618-668-2).

Tian, Y., Zhao, C.Y., 2009a. Heat transfer analysis for Phase Change Materials (PCMs). In: *Proceedings of 11th International Conference on Energy Storage (Effstock 2009)*, Stockholm, Sweden.

Tian, Y., Zhao, C.Y., 2009b. Numerical investigations of heat transfer in phase change materials using non-equilibrium model. In: *Proceedings of 11th UK National Heat*

Transfer Conference – UKHTC-11, Queen Mary College, University of London, U.K.

Tian, Y., Zhao, C.Y., 2010. Thermal analysis in phase change materials (PCMs) embedded with metal foams. In: *Proceedings of 14th International Heat Transfer Conference (ASME Conference) – IHTC-14*, Washington D.C., U.S.A., Volume **7**, 425–434.

Tian, Y., Zhao, C.Y., 2011a. A numerical investigation of heat transfer in phase change materials (PCMs) embedded in porous metals. *Energy* **36**, 5539–5546.

Tian, Y., Zhao, C.Y., 2011b. Natural convection investigations in porous phase change materials. *Nanosci. Nanotech. Lett.* **3**(6), 769–772.

Tian, Y., Zhao, C.Y., 2012a. A review of solar collectors and thermal energy storage in solar thermal applications. *Appl. Energ.* (In Press, Corrected Proof). doi:10.1016/j.apenergy.2012.11.051.

Tian, Y., Zhao, C.Y., 2012b. A thermal and exergetic analysis of Metal Foam-enhanced Cascaded thermal Energy storage (MF-CTES). *Int. J. Heat Mass Tran.* (In Press, Corrected Proof). doi:10.1016/j.ijheatmasstransfer.2012.11.034.

Tian, Y., Zhao, C.Y., Lapkin A., 2012. Exergy optimisation for cascaded thermal storage. In: *Proceedings of 12th International Conference on Energy Storage (Innostock 2012),* University of Lleida, Lleida, Spain.

Tian, Y., Zhao, C.Y., Li, Z.Y., Qu, Z.G., 2008. Flow and heat transfer in metal foam filled pipes under two extended Darcy models. *J. Eng. Thermophys* **29**(8), 1380–1382 (EI accession number: 20083311459656, full paper in Chinese, with English Abstract).

Turton, R., Bailie, R.C., Whiting, W.B., Shaeiwitz, J.A., 2008. *Analysis, synthesis and design of chemical processes.* 3rd Edition, Prentice Hall, New Jersey, U.S.A.

Tyagi, V.V., Buddhi, D., 2008. Thermal cycle testing of calcium chloride hexahydrate as a possible PCM for latent heat storage. *Sol. Energ. Mat. Sol. C.* **92**, 891–899.

Vargaftik, N.B., 1975. *Handbook of physical properties of liquids and gases - pure substances and mixtures*. 2nd Edition, Hemisphere Publishing Corporation, New York.

Velraj, R., Seeniraj, R.V., Hafner, B., Faber, C., Schwarzer, K., 1999. Heat transfer enhancement in a latent heat storage system. *Sol. Energ.* **65**, 171–180.

Watanabe, T., Kanzawa, A., 1995. Second law optimization of a latent heat storage system with PCMs having different melting points. *Heat Recov. Syst. CHP*. **15**, 641–653.

Watanabe, T., Kikuchi, H., Kanzawa, A., 1993. Enhancement of charging and discharging rates in a latent heat storage system by use of PCM with different melting temperatures. *Heat Recov. Syst. CHP*. **13**, 57–66.

Wentworth, W.E., Chen, E., 1976. Simple thermal decomposition reactions for storage of solar thermal energy. *Sol. Energ.* **18**, 205–214.

Whitaker, S., 1969, Advances in the theory of fluid motion in porous media. *Ind. Eng. Chem.* **12**, 14–28.

Zalba, B., Marin, J.M., Cabeza, L.F., Mehling, H., 2003. Review on thermal energy storage with phase change: materials, heat transfer analysis and applications. *Appl. Therm. Eng.* **23**, 251–283.

Zhang, Y., Faghri, A., 1996a. Heat transfer enhancement in latent heat thermal energy storage system by using the internally finned tube. *Int. J. Heat Mass Tran.* **39**, 3165–3173.

Zhang, Y., Faghri, A., 1996b. Heat transfer enhancement in latent heat thermal energy storage system by using an external radial finned tube. *J. Enhanc. Heat Transf.* **3**, 119–127.

Zhao, C.Y., Dai, L.N., Tang, G.H., Qu, Z.G., 2010. Numerical study of natural convection in porous media (metals) using lattice Boltzmann method (LBM). *Int. J. Heat Fluid Flow* **31**, 925–934

Zhao, C.Y., Kim, T., Lu, T.J., Hodson, H.P., 2004a. Thermal transport in high porosity cellular metal foams. *J. Thermophys. Heat Tr.* **18**, 309–317.

Zhao, C.Y., Lu, T.J., Hodson, H.P., Jackson, J.D., 2004b. The temperature dependence of effective thermal conductivity of open-celled steel alloy foams. *Mat. Sci. Eng. A–Struct.* **367**, 123–131.

Zhao, C.Y., Lu, T.J., Hodson, H.P., 2004c. Thermal radiation in metal foams with open cells. *Int. J. Heat Mass Tran.* **47**, 2927–2939.

Zhao, C.Y., Lu, T.J., Hodson, H.P., 2005. Natural convection in metal foams with open cells. *Int. J. Heat Mass Tran.* **48**, 2452–2463.

Zhao, C.Y., Lu, W., Tassou, S.A., 2006. Thermal analysis on metal-foam filled heat exchangers, II. tube heat exchangers. *Int. J. Heat Mass Tran.* **49**, 2762–2770.

Zhao, C.Y., Lu, W., Tian, Y., 2010. Heat transfer enhancement for thermal energy storage using metal foams embedded within phase change materials (PCMs). *Sol. Energy* **84**, 1402–1412.

Zhou, D., Zhao, C.Y., 2011. Experimental investigations on heat transfer in Phase Change Materials (PCMs) embedded with porous materials. *Appl. Therm. Eng.* **31**, 970–977.

Zhou, D., Zhao, C.Y., Tian, Y., 2012. Review on thermal energy storage with phase change materials (PCMs) in building applications. *Appl. Energ.* **92**, 593–605.

Zondag, A.H., Kalbasenka, A., Van Essen, M., 2008. First studies in reactor concepts for thermochemical storage. In: *Proceedings of 1st International Conference on Solar Heating, Cooling and Buildings (Eurosun 2008)*, Lisbon, Portugal.

Zukauskas, A.A., 1987. Convective heat transfer in cross-flow. Chapter 6 in Book: *Handbook of single-phase heat transfer*, editors: Kakac, S., Shah, R.K., Aung, W., Wiley, New York.

Appendix: SIMPLE Algorithm

SIMPLE is the abbreviation for “Semi-Implicit Method for Pressure-Linked Equations”, which was used in Chapters 4 and 6. Appendix A gives the scource code for the SIMPLE algorithm in *Fortran 77*.

```
*---------------------------MAIN PROGRAM---------------------------------*
*******************************************************************************
      LOGICAL LSTOP
      COMMON/CNTL/LSTOP
*******************************************************************************
      OPEN(08,FILE='teresul')
      CALL SETUP0
      CALL GRID
      CALL SETUP1
      CALL START
   10 CALL DENSE
      CALL BOUND
      CALL OUTPUT
      IF(.NOT.LSTOP) GO TO 15
      CLOSE(08)
      STOP
   15 CALL SETUP2
      GO TO 10
      END
*-------------------------------------------------------------------
      SUBROUTINE DIFLOW
*******************************************************************************
      COMMON/COEF/FLOW,DIFF,ACOF
*******************************************************************************
      ACOF=DIFF
      IF(FLOW .EQ.0.0)RETURN
      TEMP=DIFF-ABS(FLOW)*0.1
      ACOF=0.
      IF(TEMP .LE. 0. ) RETURN
      TEMP=TEMP/DIFF
      ACOF=DIFF*TEMP**5
      RETURN
      END
*-------------------------------------------------------------------
      SUBROUTINE SOLVE
*******************************************************************************
      DOUBLE PRECISION TITLE
      LOGICAL LSOLVE,LPRINT,LBLK,LSTOP
      COMMON F(22,22,10),P(22,22),RHO(22,22),GAM(22,22),CON(22,22),
```

```
     &  AIP(22,22),AIM(22,22),AJP(22,22),AJM(22,22),AP(22,22),
     &  X(22),XU(22),XDIF(22),XCV(22),XCVS(22),
     &  Y(22),YV(22),YDIF(22),YCV(22),YCVS(22),
     & YCVR(22),YCVRS(22),ARX(22),ARXJ(22),ARXJP(22),
     & R(22),RMN(22),SX(22),SXMN(22),XCVI(22),XCVIP(22)
      COMMON DU(22,22),DV(22,22),FV(22),FVP(22),
     &  FX(22),FXM(22),FY(22),FYM(22),PT(22),QT(22)
      COMMON /INDX/NF,NFMAX,NP,NRHO,NGAM,L1,L2,L3,M1,M2,M3,
     &  IST,JST,ITER,LAST,TITLE(13),RELAX(13),TIME,DT,XL,YL,
     &IPREF,JPREF,LSOLVE(10),LPRINT(13),LBLK(10),MODE,NTIMES(10),RHOCON
*************************************************************************
      ISTF=IST-1
      JSTF=JST-1
      IT1=L2+IST
      IT2=L3+IST
      JT1=M2+JST
      JT2=M3+JST
*************************************************************************
      DO 999 NT=1,NTIMES(NF)
      DO 999 N=NF,NF
*-------------------------------------------------------------------------
      IF(.NOT. LBLK(NF)) GO TO 10
      PT(ISTF)=0.
      QT(ISTF)=0.
      DO 11 I=IST,L2
      BL=0.
      BLP=0.
      BLM=0.
      BLC=0.
      DO 12 J=JST,M2
      BL=BL+AP(I,J)
      IF(J .NE. M2) BL=BL-AJP(I,J)
      IF(J .NE. JST) BL=BL-AJM(I,J)
      BLP=BLP+AIP(I,J)
      BLM=BLM+AIM(I,J)
      BLC=BLC+CON(I,J)+AIP(I,J)*F(I+1,J,N)+AIM(I,J)*F(I-1,J,N)
     &   +AJP(I,J)*F(I,J+1,N)+AJM(I,J)*F(I,J-1,N)-AP(I,J)*F(I,J,N)
   12 CONTINUE
      DENOM=BL-PT(I-1)*BLM
      DENO=1.E15
      IF(ABS(DENOM/BL) .LT. 1.E-10) DENOM=1.E20*DENO
      PT(I)=BLP/DENOM
      QT(I)=(BLC+BLM*QT(I-1))/DENOM
   11 CONTINUE
      BL=0.
      DO 13 II=IST,L2
      I=IT1-II
      BL=BL*PT(I)+QT(I)
      DO 13 J=JST,M2
```

```
  13 F(I,J,N)=F(I,J,N)+BL
*-------------------------------------------------------------------------
      PT(JSTF)=0.
      QT(JSTF)=0.
      DO 21 J=JST,M2
      BL=0.
      BLP=0.
      BLM=0.
      BLC=0.
      DO 22 I=IST,L2
      BL=BL+AP(I,J)
      IF(I .NE. L2) BL=BL-AIP(I,J)
      IF(I .NE. IST) BL=BL-AIM(I,J)
      BLP=BLP+AJP(I,J)
      BLM=BLM+AJM(I,J)
      BLC=BLC+CON(I,J)+AIP(I,J)*F(I+1,J,N)+AIM(I,J)*F(I-1,J,N)
     &   +AJP(I,J)*F(I,J+1,N)+AJM(I,J)*F(I,J-1,N)-AP(I,J)*F(I,J,N)
  22 CONTINUE
      DENOM=BL-PT(J-1)*BLM
      IF (ABS(DENOM/BL) .LT. 1E-10) DENOM=1.E20*DENO
      PT(J)=BLP/DENOM
      QT(J)=(BLC+BLM*QT(J-1))/DENOM
  21 CONTINUE
      BL=0.
      DO 23 JJ=JST,M2
      J=JT1-JJ
      BL=BL*PT(J)+QT(J)
      DO 23 I=IST,L2
  23 F(I,J,N)=F(I,J,N)+BL
  10 CONTINUE
*-------------------------------------------------------------------------
      DO 90 J=JST,M2
      PT(ISTF)=0.
      QT(ISTF)=F(ISTF,J,N)
      DO 70 I=IST,L2
      DENOM=AP(I,J)-PT(I-1)*AIM(I,J)
      PT(I)=AIP(I,J)/DENOM
      TEMP=CON(I,J)+AJP(I,J)*F(I,J+1,N)+AJM(I,J)*F(I,J-1,N)
      QT(I)=(TEMP+AIM(I,J)*QT(I-1))/DENOM
  70 CONTINUE
      DO 80 II=IST,L2
      I=IT1-II
  80 F(I,J,N)=F(I+1,J,N)*PT(I)+QT(I)
  90 CONTINUE
*-------------------------------------------------------------------------
      DO 190 JJ=JST,M3
      J=JT2-JJ
      PT(ISTF)=0.
      QT(ISTF)=F(ISTF,J,N)
```

```
      DO 170 I=IST,L2
      DENOM=AP(I,J)-PT(I-1)*AIM(I,J)
      PT(I)=AIP(I,J)/DENOM
      TEMP=CON(I,J)+AJP(I,J)*F(I,J+1,N)+AJM(I,J)*F(I,J-1,N)
      QT(I)=(TEMP+AIM(I,J)*QT(I-1))/DENOM
  170 CONTINUE
      DO 180 II=IST,L2
      I=IT1-II
  180 F(I,J,N)=F(I+1,J,N)*PT(I)+QT(I)
  190 CONTINUE
*---------------------------------------------------------------------
      DO 290 I=IST,L2
      PT(JSTF)=0.
      QT(JSTF)=F(I,JSTF,N)
      DO 270 J=JST,M2
      DENOM=AP(I,J)-PT(J-1)*AJM(I,J)
      PT(J)=AJP(I,J)/DENOM
      TEMP=CON(I,J)+AIP(I,J)*F(I+1,J,N)+AIM(I,J)*F(I-1,J,N)
      QT(J)=(TEMP+AJM(I,J)*QT(J-1))/DENOM
  270 CONTINUE
      DO 280 JJ=JST,M2
      J=JT1-JJ
  280 F(I,J,N)=F(I,J+1,N)*PT(J)+QT(J)
  290 CONTINUE
*---------------------------------------------------------------------
      DO 390 II=IST,L3
      I=IT2-II
      PT(JSTF)=0.
      QT(JSTF)=F(I,JSTF,N)
      DO 370 J=JST,M2
      DENOM=AP(I,J)-PT(J-1)*AJM(I,J)
      PT(J)=AJP(I,J)/DENOM
      TEMP=CON(I,J)+AIP(I,J)*F(I+1,J,N)+AIM(I,J)*F(I-1,J,N)
      QT(J)=(TEMP+AJM(I,J)*QT(J-1))/DENOM
  370 CONTINUE
      DO 380 JJ=JST,M2
      J=JT1-JJ
  380 F(I,J,N)=F(I,J+1,N)*PT(J)+QT(J)
  390 CONTINUE
*********************************************************************
  999 CONTINUE
      DO 400 J=2,M2
      DO 400 I=2,L2
      CON(I,J)=0.
      AP(I,J)=0.
  400 CONTINUE
      RETURN
      END
*********************************************************************
```

```
      SUBROUTINE SETUP
**********************************************************************
      DOUBLE PRECISION TITLE
      LOGICAL LSOLVE,LPRINT,LBLK,LSTOP
      COMMON F(22,22,10),P(22,22),RHO(22,22),GAM(22,22),CON(22,22),
     & AIP(22,22),AIM(22,22),AJP(22,22),AJM(22,22),AP(22,22),
     & X(22),XU(22),XDIF(22),XCV(22),XCVS(22),
     & Y(22),YV(22),YDIF(22),YCV(22),YCVS(22),
     &YCVR(22),YCVRS(22),ARX(22),ARXJ(22),ARXJP(22),
     &R(22),RMN(22),SX(22),SXMN(22),XCVI(22),XCVIP(22)
      COMMON DU(22,22),DV(22,22),FV(22),FVP(22),
     & FX(22),FXM(22),FY(22),FYM(22),PT(22),QT(22)
      COMMON /INDX/NF,NFMAX,NP,NRHO,NGAM,L1,L2,L3,M1,M2,M3,
     & IST,JST,ITER,LAST,TITLE(13),RELAX(13),TIME,DT,XL,YL,
     & IPREF,JPREF,LSOLVE(10),LPRINT(13),LBLK(10),MODE,NTIMES(10),RHOCON
      COMMON/CNTL/LSTOP
      COMMON/SORC/SMAX,SSUM
      COMMON/COEF/FLOW,DIFF,ACOF
      DIMENSION U(22,22),V(22,22),PC(22,22)
      EQUIVALENCE (F(1,1,1),U(1,1)),(F(1,1,2),V(1,1)),(F(1,1,3),PC(1,1))
**********************************************************************
    1 FORMAT(//15X,'COMPUTATION IN CARTISIAN COORDINATES')
    2 FORMAT(//15X,'COMPUTATION FOR AXISYMMETRICAL SITUATION')
    3 FORMAT(//15X,' COMPUTATION IN POLAR COORDINATES  ')
    4 FORMAT(1X,14X,40(1H*),//)
*---------------------------------------------------------------------
      ENTRY SETUP0
      NFMAX=10
      NP=11
      NRHO=12
      NGAM=13
      LSTOP=.FALSE.
      DO 779 I=1,10
      LSOLVE(I)=.FALSE.
      LBLK(I)=.TRUE.
  779 NTIMES(I)=1
      DO 889 I=1,13
      LPRINT(I)=.FALSE.
  889 RELAX(I)=1.
      MODE=1
      LAST=5
      TIME=0.
      ITER=0
      DT=1.0E+10
      IPREF=1
      JPREF=1
      RHOCON=1
      RETURN
*---------------------------------------------------------------------
```

```
      ENTRY SETUP1
      L2=L1-1
      L3=L2-1
      M2=M1-1
      M3=M2-1
      X(1)=XU(2)
      DO 5 I=2,L2
    5 X(I)=0.5*(XU(I+1)+XU(I))
      X(L1)=XU(L1)
      Y(1)=YV(2)
      DO 10 J=2,M2
   10 Y(J)=0.5*(YV(J+1)+YV(J))
      Y(M1)=YV(M1)
      DO 15 I=2,L1
   15 XDIF(I)=X(I)-X(I-1)
      DO 18 I=2,L2
   18 XCV(I)=XU(I+1)-XU(I)
      DO 20 I=3,L2
   20 XCVS(I)=XDIF(I)
      XCVS(3)=XCVS(3)+XDIF(2)
      XCVS(L2)=XCVS(L2)+XDIF(L1)
      DO 22 I=3,L3
      XCVI(I)=0.5*XCV(I)
   22 XCVIP(I)=XCVI(I)
      XCVIP(2)=XCV(2)
      XCVI(L2)=XCV(L2)
      DO 35 J=2,M1
   35 YDIF(J)=Y(J)-Y(J-1)
      DO 40 J=2,M2
   40 YCV(J)=YV(J+1)-YV(J)
      DO 45 J=3,M2
   45 YCVS(J)=YDIF(J)
      YCVS(3)=YCVS(3)+YDIF(2)
      YCVS(M2)=YCVS(M2)+YDIF(M1)
      IF (MODE .NE. 1) GO TO 55
      DO 52 J=1,M1
      RMN(J)=1.
   52 R(J)=1.
      GO TO 56
   55 DO 50 J=2,M1
   50 R(J)=R(J-1)+YDIF(J)
      RMN(2)=R(1)
      DO 60 J=3,M2
   60 RMN(J)=RMN(J-1)+YCV(J-1)
      RMN(M1)=R(M1)
   56 CONTINUE
      DO 57 J=1,M1
      SX(J)=1.
      SXMN(J)=1.
```

```
      IF(MODE .NE. 3) GO TO 57
      SX(J)=R(J)
      IF(J .NE. 1) SXMN(J)=RMN(J)
   57 CONTINUE
      DO 62 J=2,M2
      YCVR(J)=R(J)*YCV(J)
      ARX(J)=YCVR(J)
      IF (MODE .NE. 3) GO TO 62
      ARX(J)=YCV(J)
   62 CONTINUE
      DO 64 J=4,M3
   64 YCVRS(J)=0.5*(R(J)+R(J-1))*YDIF(J)
      YCVRS(3)=0.5*(R(3)+R(1))*YCVS(3)
      YCVRS(M2)=0.5*(R(M1)+R(M3))*YCVS(M2)
      IF(MODE .NE. 2) GO TO 67
      DO 65 J=3,M3
      ARXJ(J)=0.25*(1.+RMN(J)/R(J))*ARX(J)
   65 ARXJP(J)=ARX(J)-ARXJ(J)
      GO TO 68
   67 DO 66 J=3,M3
      ARXJ(J)=0.5*ARX(J)
   66 ARXJP(J)=ARXJ(J)
   68 ARXJP(2)=ARX(2)
      ARXJ(M2)=ARX(M2)
      DO 70 J=3,M3
      FV(J)=ARXJP(J)/ARX(J)
   70 FVP(J)=1.-FV(J)
      DO 85 I=3,L2
      FX(I)=0.5*XCV(I-1)/XDIF(I)
   85 FXM(I)=1.-FX(I)
      FX(2)=0.
      FXM(2)=1.
      FX(L1)=1.
      FXM(L1)=0.
      DO 90 J=3,M2
      FY(J)=0.5*YCV(J-1)/YDIF(J)
   90 FYM(J)=1.-FY(J)
      FY(2)=0.
      FYM(2)=1.
      FY(M1)=1.
      FYM(M1)=0.
*---CON,AP,U,V,RHO,PC AND P ARRAYS ARE INITIALIZED HERE----
      DO 95 J=1,M1
      DO 95 I=1,L1
      PC(I,J)=0.
      U(I,J)=0.
      V(I,J)=0.
      CON(I,J)=0.
      AP(I,J)=0.
```

```
      RHO(I,J)=RHOCON
      P(I,J)=0.
   95 CONTINUE
      IF(MODE .EQ. 1) WRITE(8,1)
      IF(MODE .EQ. 2) WRITE(8,2)
      IF(MODE .EQ. 3) WRITE(8,3)
      WRITE(8,4)
      RETURN
*-------------------------------------------------------------------
      ENTRY SETUP2
*---COEFFICIENTS FOR THE U EQUATION----
      NF=1
      IF(.NOT. LSOLVE(NF)) GO TO 100
      IST=3
      JST=2
      CALL GAMSOR
      REL=1.-RELAX(NF)
      DO 102 I=3,L2
      FL=XCVI(I)*V(I,2)*RHO(I,1)
      FLM=XCVIP(I-1)*V(I-1,2)*RHO(I-1,1)
      FLOW=R(1)*(FL+FLM)
      DIFF=R(1)*(XCVI(I)*GAM(I,1)+XCVIP(I-1)*GAM(I-1,1))/YDIF(2)
      CALL DIFLOW
  102 AJM(I,2)=ACOF+AMAX1(0.,FLOW)
      DO 103 J=2,M2
      FLOW=ARX(J)*U(2,J)*RHO(1,J)
      DIFF=ARX(J)*GAM(1,J)/(XCV(2)*SX(J))
      CALL DIFLOW
      AIM(3,J)=ACOF+AMAX1(0.,FLOW)
      DO 103 I=3,L2
      IF(I .EQ. L2) GO TO 104
      FL=U(I,J)*(FX(I)*RHO(I,J)+FXM(I)*RHO(I-1,J))
      FLP=U(I+1,J)*(FX(I+1)*RHO(I+1,J)+FXM(I+1)*RHO(I,J))
      FLOW=ARX(J)*0.5*(FL+FLP)
      DIFF=ARX(J)*GAM(I,J)/(XCV(I)*SX(J))
      GO TO 105
  104 FLOW=ARX(J)*U(L1,J)*RHO(L1,J)
      DIFF=ARX(J)*GAM(L1,J)/(XCV(L2)*SX(J))
  105 CALL DIFLOW
      AIM(I+1,J)=ACOF+AMAX1(0.,FLOW)
      AIP(I,J)=AIM(I+1,J)-FLOW
      IF (J .EQ. M2) GOTO 106
      FL=XCVI(I)*V(I,J+1)*(FY(J+1)*RHO(I,J+1)+FYM(J+1)*RHO(I,J))
      FLM=XCVIP(I-1)*V(I-1,J+1)*(FY(J+1)*RHO(I-1,J+1)+FYM(J+1)*
     &   RHO(I-1,J))
      GM=GAM(I,J)*GAM(I,J+1)/(YCV(J)*GAM(I,J+1)+YCV(J+1)*GAM(I,J)+
     &   1.0E-30)*XCVI(I)
      GMM=GAM(I-1,J)*GAM(I-1,J+1)/(YCV(J)*GAM(I-1,J+1)+YCV(J+1)*
     &   GAM(I-1,J)+1.E-30)*XCVIP(I-1)
```

```
      DIFF=RMN(J+1)*2.*(GM+GMM)
      GO TO 107
  106 FL=XCVI(I)*V(I,M1)*RHO(I,M1)
      FLM=XCVIP(I-1)*V(I-1,M1)*RHO(I-1,M1)
      DIFF=R(M1)*(XCVI(I)*GAM(I,M1)+XCVIP(I-1)*GAM(I-1,M1))/YDIF(M1)
  107 FLOW=RMN(J+1)*(FL+FLM)
      CALL DIFLOW
      AJM(I,J+1)=ACOF+AMAX1(0.,FLOW)
      AJP(I,J)=AJM(I,J+1)-FLOW
      VOL=YCVR(J)*XCVS(I)
      APT=(RHO(I,J)*XCVI(I)+RHO(I-1,J)*XCVIP(I-1))
     &   /(XCVS(I)*DT)
      AP(I,J)=AP(I,J)-APT
      CON(I,J)=CON(I,J)+APT*U(I,J)
      AP(I,J)=(-AP(I,J)*VOL+AIP(I,J)+AIM(I,J)+AJP(I,J)+AJM(I,J))
     &   /RELAX(NF)
      CON(I,J)=CON(I,J)*VOL+REL*AP(I,J)*U(I,J)
      DU(I,J)=VOL/(XDIF(I)*SX(J))
      CON(I,J)=CON(I,J)+DU(I,J)*(P(I-1,J)-P(I,J))
      DU(I,J)=DU(I,J)/AP(I,J)
  103 CONTINUE
      CALL SOLVE
  100 CONTINUE
*---COEFFICIENTS FOR THE V EQUATION----
      NF=2
      IF(.NOT. LSOLVE(NF)) GO TO 200
      IST=2
      JST=3
      CALL GAMSOR
      REL=1.-RELAX(NF)
      DO 202 I=2,L2
      AREA=R(1)*XCV(I)
      FLOW=AREA*V(I,2)*RHO(I,1)
      DIFF=AREA*GAM(I,1)/YCV(2)
      CALL DIFLOW
  202 AJM(I,3)=ACOF+AMAX1(0.,FLOW)
      DO 203 J=3,M2
      FL=ARXJ(J)*U(2,J)*RHO(1,J)
      FLM=ARXJP(J-1)*U(2,J-1)*RHO(1,J-1)
      FLOW=FL+FLM
      DIFF=(ARXJ(J)*GAM(1,J)+ARXJP(J-1)*GAM(1,J-1))/(XDIF(2)*SXMN(J))
      CALL DIFLOW
      AIM(2,J)=ACOF+AMAX1(0.,FLOW)
      DO 203 I=2,L2
      IF(I .EQ. L2)GO TO 204
      FL=ARXJ(J)*U(I+1,J)*(FX(I+1)*RHO(I+1,J)+FXM(I+1)*RHO(I,J))
      FLM=ARXJP(J-1)*U(I+1,J-1)*(FX(I+1)*RHO(I+1,J-1)+FXM(I+1)*
     &   RHO(I,J-1))
      GM=GAM(I,J)*GAM(I+1,J)/(XCV(I)*GAM(I+1,J)+XCV(I+1)*GAM(I,J)+
```

```
     &   1.E-30)*ARXJ(J)
         GMM=GAM(I,J-1)*GAM(I+1,J-1)/(XCV(I)*GAM(I+1,J-1)+XCV(I+1)*
     &   GAM(I,J-1)+1.0E-30)*ARXJP(J-1)
         DIFF=2.*(GM+GMM)/SXMN(J)
         GO TO 205
  204 FL=ARXJ(J)*U(L1,J)*RHO(L1,J)
         FLM=ARXJP(J-1)*U(L1,J-1)*RHO(L1,J-1)
         DIFF=(ARXJ(J)*GAM(L1,J)+ARXJP(J-1)*GAM(L1,J-1))/(XDIF(L1)*SXMN(J))
  205 FLOW=FL+FLM
         CALL DIFLOW
         AIM(I+1,J)=ACOF+AMAX1(0.,FLOW)
         AIP(I,J)=AIM(I+1,J)-FLOW
         IF(J .EQ. M2) GO TO 206
         AREA=R(J)*XCV(I)
         FL=V(I,J)*(FY(J)*RHO(I,J)+FYM(J)*RHO(I,J-1))*RMN(J)
         FLP=V(I,J+1)*(FY(J+1)*RHO(I,J+1)+FYM(J+1)*RHO(I,J))*RMN(J+1)
         FLOW=(FV(J)*FL+FVP(J)*FLP)*XCV(I)
         DIFF=AREA*GAM(I,J)/YCV(J)
         GO TO 207
  206 AREA=R(M1)*XCV(I)
         FLOW=AREA*V(I,M1)*RHO(I,M1)
         DIFF=AREA*GAM(I,M1)/YCV(M2)
  207 CALL DIFLOW
         AJM(I,J+1)=ACOF+AMAX1(0.,FLOW)
         AJP(I,J)=AJM(I,J+1)-FLOW
         VOL=YCVRS(J)*XCV(I)
         SXT=SX(J)
         IF(J .EQ. M2) SXT=SX(M1)
         SXB=SX(J-1)
         IF(J .EQ. 3) SXB=SX(1)
         APT=(ARXJ(J)*RHO(I,J)*0.5*(SXT+SXMN(J))+ARXJP(J-1)*RHO(I,J-1)*
     &   0.5*(SXB+SXMN(J)))/(YCVRS(J)*DT)
         AP(I,J)=AP(I,J)-APT
         CON(I,J)=CON(I,J)+APT*V(I,J)
         AP(I,J)=(-AP(I,J)*VOL+AIP(I,J)+AIM(I,J)+AJP(I,J)+AJM(I,J))
     &   /RELAX(NF)
         CON(I,J)=CON(I,J)*VOL+REL*AP(I,J)*V(I,J)
         DV(I,J)=VOL/YDIF(J)
         CON(I,J)=CON(I,J)+DV(I,J)*(P(I,J-1)-P(I,J))
         DV(I,J)=DV(I,J)/AP(I,J)
  203 CONTINUE
         CALL SOLVE
  200 CONTINUE
*---COEFIICIENTS FOR THE PRESSURE CORRECTION EQUATION----
         NF=3
         IF(.NOT. LSOLVE(NF)) GO TO 500
         IST=2
         JST=2
         CALL GAMSOR
```

```
      SMAX=0.
      SSUM=0.
      DO 410 J=2,M2
      DO 410 I=2,L2
      VOL=YCVR(J)*XCV(I)
  410 CON(I,J)=CON(I,J)*VOL
      DO 402 I=2,L2
      ARHO=R(1)*XCV(I)*RHO(I,1)
      CON(I,2)=CON(I,2)+ARHO*V(I,2)
  402 AJM(I,2)=0.
      DO 403 J=2,M2
      ARHO=ARX(J)*RHO(1,J)
      CON(2,J)=CON(2,J)+ARHO*U(2,J)
      AIM(2,J)=0.
      DO 403 I=2,L2
      IF(I .EQ. L2) GO TO 404
      ARHO=ARX(J)*(FX(I+1)*RHO(I+1,J)+FXM(I+1)*RHO(I,J))
      FLOW=ARHO*U(I+1,J)
      CON(I,J)=CON(I,J)-FLOW
      CON(I+1,J)=CON(I+1,J)+FLOW
      AIP(I,J)=ARHO*DU(I+1,J)
      AIM(I+1,J)=AIP(I,J)
      GO TO 405
  404 ARHO=ARX(J)*RHO(L1,J)
      CON(I,J)=CON(I,J)-ARHO*U(L1,J)
      AIP(I,J)=0.
  405 IF(J .EQ. M2) GO TO 406
      ARHO=RMN(J+1)*XCV(I)*(FY(J+1)*RHO(I,J+1)+FYM(J+1)*RHO(I,J))
      FLOW=ARHO*V(I,J+1)
      CON(I,J)=CON(I,J)-FLOW
      CON(I,J+1)=CON(I,J+1)+FLOW
      AJP(I,J)=ARHO*DV(I,J+1)
      AJM(I,J+1)=AJP(I,J)
      GO TO 407
  406 ARHO=RMN(M1)*XCV(I)*RHO(I,M1)
      CON(I,J)=CON(I,J)-ARHO*V(I,M1)
      AJP(I,J)=0.
  407 AP(I,J)=AIP(I,J)+AIM(I,J)+AJP(I,J)+AJM(I,J)
      PC(I,J)=0.
      SMAX=AMAX1(SMAX,ABS(CON(I,J)))
      SSUM=SSUM+CON(I,J)
  403 CONTINUE
      CALL SOLVE
*---COMEE HERE TO CORRECT THE PRESSURE AND VELOCITIES
      DO 501 J=2,M2
      DO 501 I=2,L2
      P(I,J)=P(I,J)+PC(I,J)*RELAX(NP)
      IF(I .NE. 2) U(I,J)=U(I,J)+DU(I,J)*(PC(I-1,J)-PC(I,J))
      IF(J .NE. 2) V(I,J)=V(I,J)+DV(I,J)*(PC(I,J-1)-PC(I,J))
```

```
 501 CONTINUE
 500 CONTINUE
*---COEFFICIENTS FOR OTHER EQUATIONS----
      IST=2
      JST=2
      DO 600 N=4,NFMAX
      NF=N
      IF(.NOT. LSOLVE(NF)) GO TO 600
      CALL GAMSOR
      REL=1.-RELAX(NF)
      DO 602 I=2,L2
      AREA=R(1)*XCV(I)
      FLOW=AREA*V(I,2)*RHO(I,1)
      DIFF=AREA*GAM(I,1)/YDIF(2)
      CALL DIFLOW
  602 AJM(I,2)=ACOF+AMAX1(0.,FLOW)
      DO 603 J=2,M2
      FLOW=ARX(J)*U(2,J)*RHO(1,J)
      DIFF=ARX(J)*GAM(1,J)/(XDIF(2)*SX(J))
      CALL DIFLOW
      AIM(2,J)=ACOF+AMAX1(0.,FLOW)
      DO 603 I=2,L2
      IF(I .EQ. L2) GO TO 604
      FLOW=ARX(J)*U(I+1,J)*(FX(I+1)*RHO(I+1,J)+FXM(I+1)*RHO(I,J))
      DIFF=ARX(J)*2.*GAM(I,J)*GAM(I+1,J)/((XCV(I)*GAM(I+1,J)+
     &   XCV(I+1)*GAM(I,J)+1.0E-30)*SX(J))
      GO TO 605
  604 FLOW=ARX(J)*U(L1,J)*RHO(L1,J)
      DIFF=ARX(J)*GAM(L1,J)/(XDIF(L1)*SX(J))
  605 CALL DIFLOW
      AIM(I+1,J)=ACOF+AMAX1(0.,FLOW)
      AIP(I,J)=AIM(I+1,J)-FLOW
      AREA=RMN(J+1)*XCV(I)
      IF(J .EQ. M2) GO TO 606
      FLOW=AREA*V(I,J+1)*(FY(J+1)*RHO(I,J+1)+FYM(J+1)*RHO(I,J))
      DIFF=AREA*2.*GAM(I,J)*GAM(I,J+1)/(YCV(J)*GAM(I,J+1)+
     &   YCV(J+1)*GAM(I,J)+1.0E-30)
      GO TO 607
  606 FLOW=AREA*V(I,M1)*RHO(I,M1)
      DIFF=AREA*GAM(I,M1)/YDIF(M1)
  607 CALL DIFLOW
      AJM(I,J+1)=ACOF+AMAX1(0.,FLOW)
      AJP(I,J)=AJM(I,J+1)-FLOW
      VOL=YCVR(J)*XCV(I)
      APT=RHO(I,J)/DT
      AP(I,J)=AP(I,J)-APT
      CON(I,J)=CON(I,J)+APT*F(I,J,NF)
      AP(I,J)=(-AP(I,J)*VOL+AIP(I,J)+AIM(I,J)+AJP(I,J)+AJM(I,J))
     &   /RELAX(NF)
```

```
      CON(I,J)=CON(I,J)*VOL+REL*AP(I,J)*F(I,J,NF)
  603 CONTINUE
      CALL SOLVE
  600 CONTINUE
      TIME=TIME+DT
      ITER=ITER+1
      IF(ITER .GE. LAST) LSTOP=.TRUE.
      RETURN
      END
*---------------------------------------------------------------------
      SUBROUTINE SUPPLY
*********************************************************************
      DOUBLE PRECISION TITLE
      LOGICAL LSOLVE,LPRINT,LBLK,LSTOP
      COMMON F(22,22,10),P(22,22),RHO(22,22),GAM(22,22),CON(22,22),
     & AIP(22,22),AIM(22,22),AJP(22,22),AJM(22,22),AP(22,22),
     & X(22),XU(22),XDIF(22),XCV(22),XCVS(22),
     & Y(22),YV(22),YDIF(22),YCV(22),YCVS(22),
     &YCVR(22),YCVRS(22),ARX(22),ARXJ(22),ARXJP(22),
     &R(22),RMN(22),SX(22),SXMN(22),XCVI(22),XCVIP(22)
      COMMON DU(22,22),DV(22,22),FV(22),FVP(22),
     &FX(22),FXM(22),FY(22),FYM(22),PT(22),QT(22)
      COMMON/INDX/NF,NFMAX,NP,NRHO,NGAM,L1,L2,L3,M1,M2,M3,
     & IST,JST,ITER,LAST,TITLE(13),RELAX(13),TIME,DT,XL,YL,
     & IPREF,JPREF,LSOLVE(10),LPRINT(13),LBLK(10),MODE,NTIMES(10),RHOCON
      DIMENSION U(22,22),V(22,22),PC(22,22)
      EQUIVALENCE (F(1,1,1),U(1,1)),(F(1,1,2),V(1,1)),(F(1,1,3),PC(1,1))
*********************************************************************
   10 FORMAT(1X,26(1H*),3X,A10,3X,26(1H*))
   20 FORMAT(1X,4H I =,I6,6I9)
   30 FORMAT(1X,1HJ)
   40 FORMAT(1X,I2,3X,1P7E9.2)
   50 FORMAT(1X,1H )
   51 FORMAT(1X,' I =',2X,7(I4,5X))
   52 FORMAT(1X,' X =',1P7E9.2)
   53 FORMAT(1X,'TH =',1P7E9.2)
   54 FORMAT(1X,'J =',2X,7(I4,5X))
   55 FORMAT(1X,'Y =',1P7E9.2)
*********************************************************************
      ENTRY UGRID
      XU(2)=0.
      DX=XL/FLOAT(L1-2)
      DO 1 I=3,L1
    1 XU(I)=XU(I-1)+DX
      YV(2)=0.
      DY=YL/FLOAT(M1-2)
      DO 2 J=3,M1
    2 YV(J)=YV(J-1)+DY
      RETURN
```

```
*************************************************************************
      ENTRY PRINT
      IF(.NOT. LPRINT(3)) GO TO 80
*---CALCULATE THE STREAM FUNTION----------------------------------------
      F(2,2,3)=0.
      DO 82 I=2,L1
      IF(I .NE. 2) F(I,2,3)=F(I-1,2,3)-RHO(I-1,1)*V(I-1,2)
     &   *R(1)*XCV(I-1)
      DO 82 J=3,M1
      RHOM=FX(I)*RHO(I,J-1)+FXM(I)*RHO(I-1,J-1)
   82 F(I,J,3)=F(I,J-1,3)+RHOM*U(I,J-1)*ARX(J-1)
   80 CONTINUE
*
      IF( .NOT. LPRINT(NP)) GO TO 90
*
*---CONSTRUCT BOUNDARY PRESSURES BY EXTRAPOLATION
      DO 91 J=2,M2
      P(1,J)=(P(2,J)*XCVS(3)-P(3,J)*XDIF(2))/XDIF(3)
   91 P(L1,J)=(P(L2,J)*XCVS(L2)-P(L3,J)*XDIF(L1))/XDIF(L2)
      DO 92 I=2,L2
      P(I,1)=(P(I,2)*YCVS(3)-P(I,3)*YDIF(2))/YDIF(3)
   92 P(I,M1)=(P(I,M2)*YCVS(M2)-P(I,M3)*YDIF(M1))/YDIF(M2)
      P(1,1)=P(2,1)+P(1,2)-P(2,2)
      P(L1,1)=P(L2,1)+P(L1,2)-P(L2,2)
      P(1,M1)=P(2,M1)+P(1,M2)-P(2,M2)
      P(L1,M1)=P(L2,M1)+P(L1,M2)-P(L2,M2)
      PREF=P(IPREF,JPREF)
      DO 93 J=1,M1
      DO 93 I=1,L1
   93 P(I,J)=P(I,J)-PREF
   90 CONTINUE
*
      IF(TIME.GT.0.5*DT) GOTO 320
      WRITE (8,50)
      IEND=0
  301 IF(IEND .EQ. L1) GO TO 310
      IBEG=IEND+1
      IEND=IEND+7
      IEND=MIN0(IEND,L1)
      WRITE (8,50)
      WRITE(8,51) (I,I=IBEG,IEND)
      IF(MODE .EQ. 3) GO TO 302
      WRITE(8,52) (X(I),I=IBEG,IEND)
      GO TO 303
  302 WRITE (8,53) (X(I),I=IBEG,IEND)
  303 GO TO 301
  310 JEND=0
      WRITE(8,50)
  311 IF(JEND .EQ. M1) GO TO 320
```

```
      JBEG=JEND+1
      JEND=JEND+7
      JEND=MIN0(JEND,M1)
      WRITE(8,50)
      WRITE(8,54) (J,J=JBEG,JEND)
      WRITE(8,55) (Y(J),J=JBEG,JEND)
      GO TO 311
  320 CONTINUE
*
      DO 999 N=1,NGAM
      NF=N
      IF(.NOT. LPRINT(NF)) GO TO 999
      WRITE(8,50)
      WRITE(8,10) TITLE(NF)
      IFST=1
      JFST=1
      IF(NF .EQ. 1 .OR. NF .EQ. 3) IFST=2
      IF(NF .EQ. 2 .OR. NF .EQ. 3) JFST=2
      IBEG=IFST-7
  110 CONTINUE
      IBEG=IBEG+7
      IEND=IBEG+6
      IEND=MIN0(IEND,L1)
      WRITE(8,50)
      WRITE(8,20) (I,I=IBEG,IEND)
      WRITE(8,30)
      JFL=JFST+M1
      DO 115 JJ=JFST,M1
      J=JFL-JJ
      WRITE(8,40) J,(F(I,J,NF),I=IBEG,IEND)
  115 CONTINUE
      IF(IEND .LT. L1) GO TO 110
  999 CONTINUE
      RETURN
      END
```

The main variables used above are listed below:

Symbols	Denotation
ACOF	quantity calculated by subroutine DIFLOW to give the combined convection and diffusion effect.
AIM (I, J)	the coefficient a_W.
AIP (I, J)	the coefficient a_E .
AJM (I, J)	the coefficient a_S .
AJP (I, J)	the coefficient a_N.
AP (I, J) t	the coefficient a_P ; also S_P in GAMSOR subroutine.
APT	the unsteady term $\rho/\Delta T$.
AREA	local variable,usually the area of a C.V. face.
ARHO	local variable, (area) (ρ).
ARX(J)	the area of the main C.V. face normal to the x direction.
ARXJ(J)	the part of ARX(J) that overlaps on the C.V. for V(I,J).
ARXJP(J)	the part of ARX(J) that overlaps on the C.V. for V(I,J+1).
BL	coefficients used in the block correction.
BLC	coefficients used in the block correction.
BLM	coefficients used in the block correction.
BLP	coefficients used in the block correction.
CON(I,J)	the constant term b in the discretization equation;also stands for S_C in GAMSOR.
DENOM	temporary storage.
DIFF	diffusion conductance D.
DT	the time step ΔT.
DU(I,J)	d_e influencing U(I,J).

Symbols	Denotation
DV(I,J)	d_n influencing V(I,J).
F(I,J,NF)	various Φ.
FL	temporary storage leading to FLOW.
FLM	temporary storage leading to FLOW.
FLOW	temporary storage leading to FLOW
FLP	temporary storage leading to FLOW.
FV(J)	interpolation factors which give the mass flow
FVP(J)	ρvr at a main grid point, I,J as FV(J)×ρvr (I,J)+FVP(I,J)×ρvr(I,J+1)
FX(I)	interpolation factors which give the interface.
FXM(I)	density RHOM (at the location of U(I,J)) as FX(I) ×RHO(I,J)+FXM(I) ×RHO(I-1,J).
FY(J)	interpolation factors which give the interface.
FYM(J)	density RHOM (at the location of V(I,J)) as FY(J) ×RHO(I,J)+FYM(J) ×RHO(I,J-1).
GAM(I,J)	the diffusion coefficient Γ .
I	index denoting the position in x.
IBEG IEND	temporary values used in PRINT.
IFST	the first value of I for which the print-out is arranged ;used in PRINT.
II	temporary index.
ILST	the last value of I for which the print-out is arranged ;used in PRINT.
IPREF	the value of I for the grid point which is used as a reference for pressure.
IST	the first internal-point value of I.
ISTF	IST-1; used in SOLVE.
ITER	a counter for iterations.

Symbols	Denotation
IT1 IT2	temporary values used in SOLVE.
J	index denoting the position in y.
JFL	temporary index used in PRINT.
JFST	similar to IFST.
JJ	temporary index
JLST	similar to ILST
JPREF	similar to IPREF.
JST	the first internal-point value of J.
JSTF	JST-1;used in SOLVE.
JT1 JT2	temporary values used in SOLVE.
LAST	the maximum number of iterations allowed by the user.
LBLK(NF)	when .TRUE. the block correction for F(I,J,NF) is used.
LPRINT(NF)	when .TRUE. F(I,J,NF) is printed.
LSOLVE(NF)	when .TRUE. solve for F(I,J,NF).
LSTOP	when .TRUE. computation stops.
L1	the value of I for the last grid location in the x direction.
L2	(L1-1).
L3	(L1-2).
MODE	index for the coordinate system; =1 for xy , =2 for rx , =3 for $r\theta$.
M1	the value of I for the last grid location in the y direction.
M2	(M1-1).
M3	(M1-2).
N	temporary storage for NF.

Symbols	Denotation
NF	index denoting a particular Φ.
NFMAX	the largest value of NF for which storage is assigned.
NGAM	NFMAX+3; GAM(I,J) can be considered as F(I,J,NGAM).
NP	NFMAX+1; P(I,J) can be considered as F(I,J,NP).
NRHO	NFMAX+2; RHO(I,J) can be considered as F(I,J,NRHO).
NTIMES(NF)	the number of repetitions of the sweeps in SOLVE for F(I,J,NF).
P(I,J)	the pressure p.
PC(I,J)	the pressure correction p'.
PREF	the pressure at the reference point.
PT(I) or PT(J) QT(I)or QT(J)	transformed coefficients in the TDMA.
R(J)	the radius r for a main grid point I,J.
REL	1.0-RELAX(NF).
RELAX(NF)	relaxation factor for F(I,J,NF).
RHO(I,J)	the density ρ.
RHOCON	the value of ρ for a constant-density problem.
RMN(J)	the value of radius r for the location to which V(I,J) refers.
SMAX	the largest absolute value of the "mass source" used in the p' equation .
SSUM	the algebraic sum of all the "mass sources" in the p' equation .
SX(J)	scale factor for the x direction at the main grid locations Y(J).
SXMN(J)	scale factor for the x direction at interface locations YV(J).
TEMP	temporary storage.
TIME	time t for unsteady problems.
TITLE(NF)	title for F(I,J,NF).
U(I,J)	the x-direction velocity u.

Symbols	Denotation
V(I,J)	the y-direction velocity v.
VOL	volume of the C.V..
X(I)	the values of x at grid points.
XCV(I)	the x-direction widths of main C.V..
XCVI(I)	the part of XCV(I) that overlaps on the C.V. for U(I,J).
XCVIP(I)	the part of XCV(I) that overlaps on the C.V. for U(I+1,J).
XCVS(I)	the x-direction width of the staggered C.V. for U(I,J).
XDIF(I)	the difference X(I)-X(I-1).
XL	the x-direction length of the calculation domain.
XU(I)	the locations of the C.V. faces; i.e. the location of U(I,J).
Y(J)	the values of y at grid points.
YCV(J)	the y-direction widths of main C.V..
YCVR(J)	the area $r\Delta y$ for a main C.V..
YCVRS(J)	the area $r\Delta y$ for the C.V. for v(I,J).
YCVS(J)	the y-direction width of the staggered C.V. for V(I,J).
YDIF(J)	the difference Y(J)-Y(J-1).
YL	the y-direction length of the calculation domain.
YV(J)	the locations of the C.V. faces; i.e. the location of V(I,J).